A Chemical Characterization of the Endeavour Non-buoyant Plume, Juan de Fuca Ridge

By

Meghan Zee
B.Sc. (Hons), Queen's University

A thesis submitted in Partial Fulfilment of the Requirements for the Degree of

Master of Science

In the School of Earth and Ocean Sciences

We acknowledge and respect the lək̓ʷ əŋən peoples on whose traditional territory the university stands and the Songhees, Esquimalt and W̱ SÁNEĆ peoples whose historical relationships with the land continue to this day.

Supervisory Committee

A Chemical Characterization of the Endeavour Non-buoyant Plume, Juan de Fuca Ridge

By

Meghan Zee
B.Sc. (Hons), Queen's University

Supervisory Committee

Dr. Jay T. Cullen, School of Earth and Ocean Sciences
Supervisor

Dr. Laurence A. Coogan, School of Earth and Ocean Sciences
Departmental member

Dr. Roberta C. Hamme, School of Earth and Ocean Sciences
Department member

Dr. Damian Grundle, Arizona State University
Committee member, University of Arizona

Abstract

This study aims to provide a quantitative chemical characterization of the Endeavour non-buoyant plume and examine the processes that impact trace metal transport from vent sites to the ocean interior. The chemistry of the Endeavour non-buoyant plume was analyzed using filtered and unfiltered seawater samples collected at 5 stations, starting on-axis at the Main Endeavour Vent field and extending ~45 km southwest of the axial valley. The spatial distribution of these trace metals is likely controlled by a number of processes, including metal sulfide precipitation, oxidation, sedimentation, and plume mixing.

Iron (Fe) and manganese (Mn) are limiting or co-limiting nutrients for primary productivity, nitrogen fixation and other biogeochemically important processes in the ocean. The transport of metals associated with hydrothermal plumes and the processes that impact their fate are poorly understood. High concentrations of dFe (24-68 nmol kg^{-1}) and dMn (46-98 nmol kg^{-1}), relative to ambient seawater concentrations at similar depths in the region, were observed proximal to the vent field, followed by a sharp decrease to 1.2-2.9 nmol kg^{-1} dFe and 0.76-1.4 nmol kg^{-1} dMn 45 km southwest of the axial valley. Roughly 66% of the Fe present in the non-buoyant plume proximal to the vent field is in the particulate phase (defined as the difference between total dissolvable and dissolved). The particulate phase decreases to ~45% at the most distal station. Particulate Mn increases with distance from the vent field with 25% proximal to the vent field and 56% 45 km off-axis. This study hypothesizes that the spatial distribution and size partitioning of Fe and Mn can be explained by a combination of sulfide precipitation near-field, oxidation and oxide formation, and plume mixing with surrounding seawater.

Chalcophile elements including cobalt (Co), nickel (Ni), copper (Cu), zinc (Zn), lead (Pb) and cadmium (Cd), are trace metals often associated with hydrothermal systems. Due to precipitation processes, these trace metals are not typically found in non-buoyant plumes far from vent fields. Correlations between these chalcophile elements with particulate Fe at END1 indicate similar removal pathways and highlight the importance near-field processes (precipitation, oxidation, mixing) play in controlling their net-input to the ocean. When compared to the geochemistry of sediments at the Main Endeavour Vent field, non-buoyant plume chemistry shows similar spatial trends. Furthermore, high mass accumulations of Fe, Zn and Cu on-axis along with the presence of chalcopyrite, pyrite, and sphalerite help explain the higher proportion of the particulate phase of these elements proximal to the vent field.

Table of Contents

List of Tables

List of Figures

Acknowledgements

I would like to thank Dr. Jay Cullen for this opportunity. Your continual support and understanding are what allowed me to learn and grow as an individual and researcher. The empathy and open mindedness you show towards all students is something to be admired. I am grateful for your guidance and could not have asked for a better supervisor.

Thank you to Dr. Jody Spence for your help in running the ICP. This thesis would not exist without your hard work. Thank you to the researchers at the Institute of Ocean Sciences and the crew of the CCGS John P. Tully for welcoming me onto the cruise and assisting in the very hectic 2 days of sampling. Thank you to my committee members Dr. Roberta Hamme, Dr. Laurence Coogan, and Dr. Damian Grundle for your continual guidance during this process.

A big thank you to the entire Cullen lab including Robyn, Melissa, and Tia. To Robyn, your kindness and help towards the beginning of my degree, specifically in preparation for my first cruise, is something I will always remember. To Melissa – a coincidence in living situations led to what I hope will be a lifelong friendship. Thank you for the constant chats, walks, and reminders for self-care. And finally, to Tia. You are without a doubt the best lab-mate a person could ask for. Thank you for teaching me everything I know about the lab and seaFAST, for constantly fielding my questions and for the long chats. Thank you for being an all-around incredible person and friend.

Thank you to my close friends Leanne, Anelle, Suba, Cass, and Catherine. While we live on opposite coasts, I never felt like I was alone through this process. Thank you for the constant phone and video chats and for the support through the best and worst times grad school brought. Special thanks to Cass for letting me hop over whenever I needed. Finally, thank you to my family. Thank you to my siblings Kayla and Mathew for the visits and to my parents for supporting me my entire life, making sure I grew up knowing I could not only do anything I put my head to but do it with their unwavering love and support.

Chapter 1: Introduction

1.1 Trace metals in Sea Water

Trace metals are metallic elements found in the environment at low concentrations (Bruland et al. 2013). In the open ocean, they are present at nanomolar (nM) and picomolar (pM) concentrations. Many trace metals, such as iron (Fe), act at key limiting or co-limiting nutrients for primary productivity, while others (nickel (Ni), copper (Cu), zinc (Zn), cobalt (Co), cadmium (Cd)) display water column profiles similar to important macronutrients (nitrate, phosphate, silicate), indicative of their role in key biochemical processes (Moore et al. 2013; Morel and Price 2003). The concentration of trace metals in the ocean are affected by their supply and removal from sources and sinks. Trace metal inputs can be classified as being either external or internal. External sources include riverine, atmospheric, benthic, and hydrothermal inputs, while internal inputs include processes that recycle trace metals in the water column. Processes which work to remove trace metals include biological uptake and particle scavenging (Bruland et al. 2013).

In seawater, trace metals can be defined by their water column distribution. Those with conservative type distributions, such as molybdenum (Mo), antimony (Sb), tungsten (W), and caesium (Cs), will have concentrations uniform throughout all ocean basins and maintain constant ratios with salinity. Nutrient-type distributions, such as Zn, will have low concentrations in surface waters due to trace metal assimilation by phytoplankton and/or adsorption by biogenic particles. Concentrations will increase with depth as organic matter sinks and is oxidized, releasing these metals (Bruland et al. 2013; Morel and Price 2003). Those with scavenged-type distributions have highest trace metal concentrations proximal to sources (atmospheric deposition, riverine, hydrothermal vents) and decrease with distance from these sources. These metals (aluminum (Al), manganese (Mn)), will have short residence times in the ocean and have a high affinity for particles. Some trace metals will be strongly influenced by both scavenging and recycling processes and will have hybrid-type distributions. Fe, for example, is depleted in surface waters such as high-nutrient, low-chlorophyll zones, but can also show surface maxima's proximal to external sources including riverine and hydrothermal vents (Bruland et al. 2013; Moore et al. 2013).

Given their influence on ocean processes, trace metals have been the subject of extensive study. Efforts to map the global distribution of trace metals has consisted of ongoing efforts of improving data

coverage through global programs such as the GEOTRACES programme (Anderson 2020). Programs such as this have not only provided useful insight into the distribution of trace metals in the ocean with respect to location specific processes such as surface biological consumption and redistribution by ocean circulation (Anderson 2020) but have highlighted the need for additional investment into quantifying inputs from various sources.

1.2 Hydrothermal Circulation

Hydrothermal circulation occurs in regions where there is sufficient rock permeability and a substantial heat source and are therefore found predominantly along mid-ocean ridges or spreading centers (Figure 1).

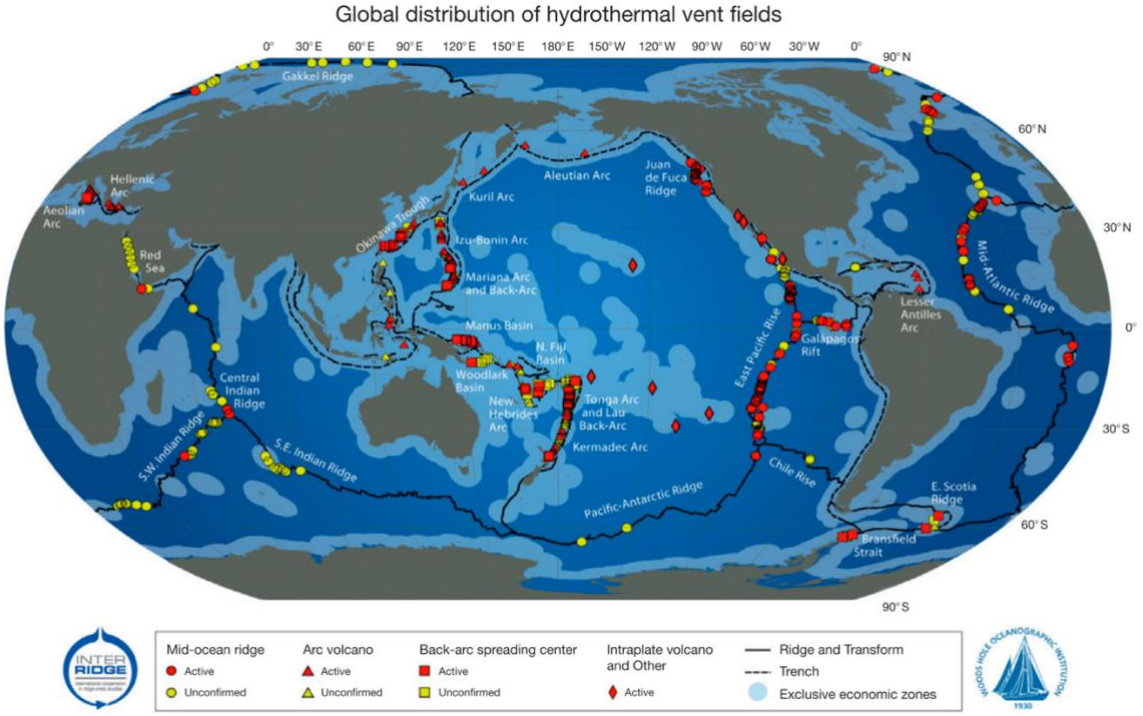

Figure 1. Map of global distribution of hydrothermal vents discovered. Red symbols indicate vents that have been visually confirmed. Yellow symbols indicate vents sites that have been inferred though the detection of water column chemical signals. Figure taken from (http://www.interridge.org/irvents/).

Hydrothermal vents were first discovered in 1977 by scientists diving along the Galapagos Spreading center (Edmond et al. 1979). This was followed by the discovery of high temperature vent fluids (380°C) by MacDonald in 1980 at 21°N on the East Pacific Rise (EPR). Since then, researchers have used their unique chemical characteristics and anomalies to find and track hydrothermal activity in numerous locations (Bennett et al. 2008; Fitzsimmons et al. 2017; Klunder et al. 2012; Wu et al.

2011). Hydrothermal circulation occurs when seawater percolates down through cracks in oceanic crust. The seawater becomes heated by underlying magma bodies, reaching temperatures of up to 450°C (German and Seyfried 2013). The heated seawater reacts with the surrounding rock, leaching metals from the crust and becoming chemically modified.

The region in which metals are leached from crust, becoming concentrated in seawater include both the reaction and up-flow zones. Within these zones, temperatures reach >400°C causing phase separation (Bischoff and Pitzer 1985; German and Seyfried 2013). Phase separation partitions circulating waters into a brine phase, characterized by higher Cl- concentrations, and a vapor phase, which is enriched in volatile gasses (Von Damm 1995; German and Seyfried 2013). Heating in the reaction zone results in the removal of magnesium and sulphate from the seawater, decreasing the pH of the fluid to about 4 (at 25°C) and forming anhydrite and smectite minerals which make up the base of the chimney structure (German and Seyfried 2013). The increased acidity and temperature, as well as the precipitation of Mg-sulfate minerals provide both an environment and framework for metal-sulfide minerals to precipitate onto (Figure 2). Metal leaching from the host rock and subsequent precipitation allow the fluid to become enriched in transition metals and rare earth elements (REE) (Campbell et al. 1988; Von Damm 1995). In addition, gases (H_2, CH_4, H_2S, CO_2, ^3He) are produced from water-rock reactions and incorporated through magmatic degassing (Butterfield et al. 1994).

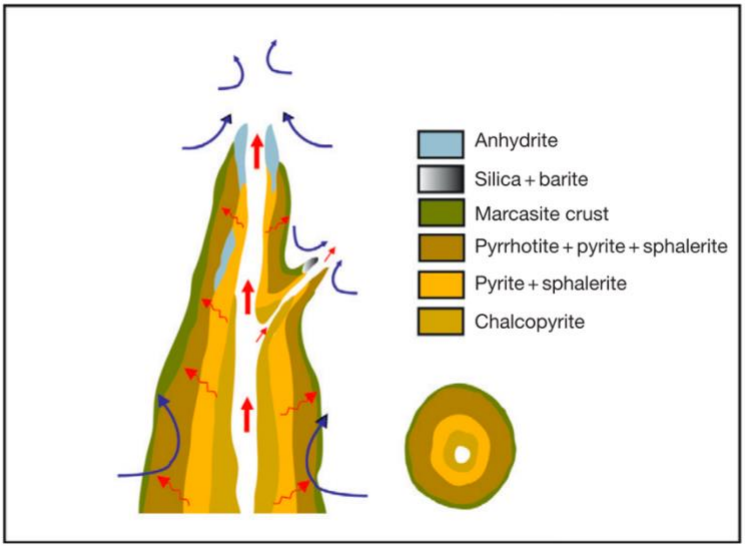

Figure 2. Mineral zonation of typical black smoker chimney (German and Seyfried 2013).

Hydrothermal fluids will have varying chemical compositions, depending on the host rock (basalt, ultramafic) and geologic environment (spreading centre, back arc system). Broadly speaking, vent fluids can be described as being modified through the loss of magnesium, sulfate, and alkalinity, and the gain of many metals (transition metals and rare earth elements) relative to chloride (Cl) (Figure 3) (German and Seyfried 2013).

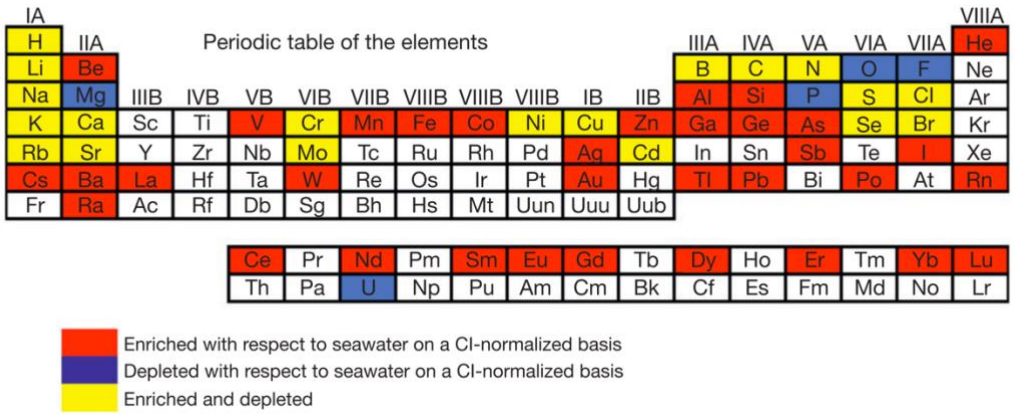

Figure 3. Periodic table showing enriched and depleted elements in hydrothermal vent fluids relative to seawater. Figure from German and Seyfried (2013).

1.3 Hydrothermal Plumes

Hydrothermal plumes form in the water column above active venting sites where hydrothermal fluids are expelled from the seafloor. As the high temperature fluids are vented into the overlying cool and oxidizing seawater, a series of oxidation-reduction (redox) reactions occur, resulting in the precipitation of a variety of metal sulfide phases such as pyrite, chalcopyrite and sphalerite (Baker et al. 1995; Feely et al. 1992). The extreme temperature difference between the vent fluid and surrounding seawater creates a density difference causing the fluid to rise through the water column. This is termed the buoyant plume (BP). Progressive dilution and cooling of the original vent fluid as the plume rises occurs until the buoyant plume reaches a maximum height above the seafloor where the density of the plume matches that of the surrounding seawater (Butterfield, et al. 1994; German and Seyfried 2013). This stage is referred to as the non-buoyant plume (NBP). Upon reaching neutral buoyancy it will start to disperse laterally, carrying these chemical enrichments and depletions. (Figure 4).

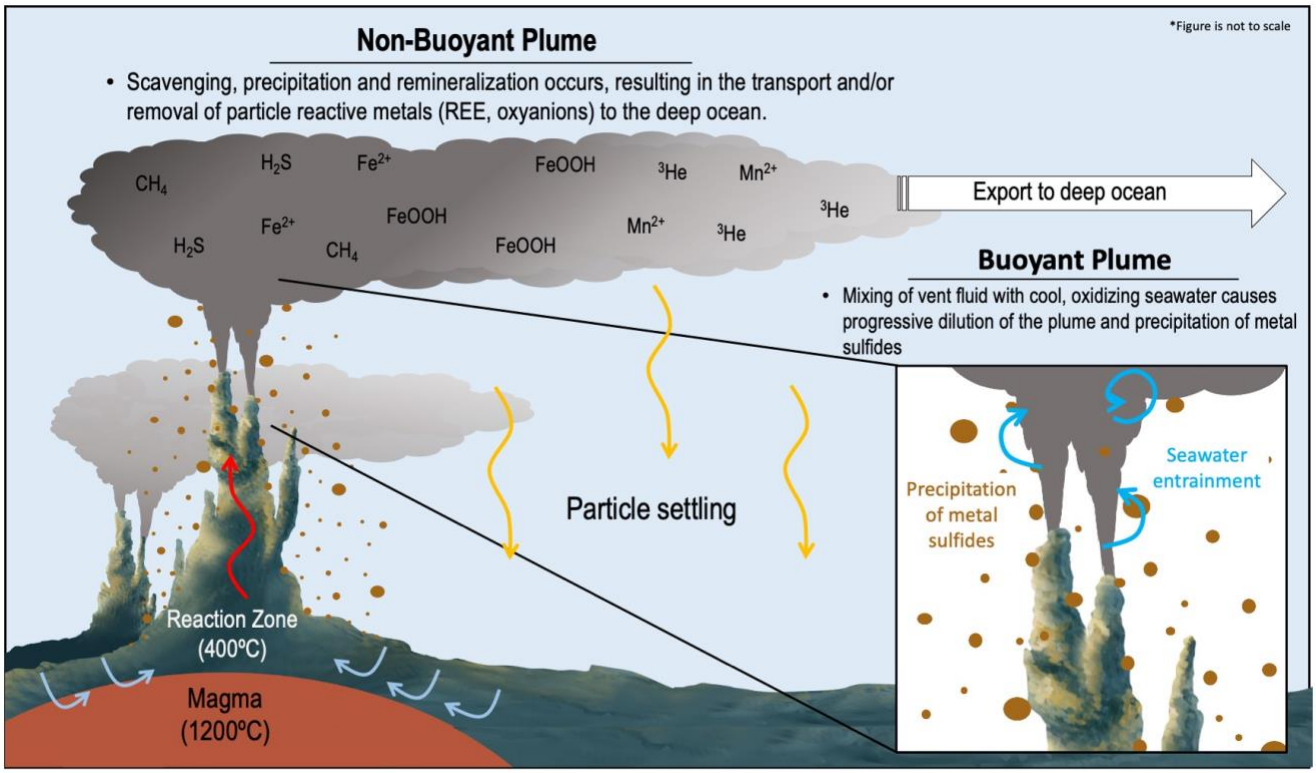

Figure 4. Schematic diagram of a hydrothermal vent system (Figure is not to scale). Seawater percolates into ocean crust where it is heated by underlying magma chambers in the reaction zone. Modified seawater rises and vents at the surface where it will entrain seawater, forming a buoyant plume. The buoyant plume rises until it reaches neutral buoyancy, after which it spreads laterally, carrying with it several chemical enrichments and depletions. Figure has been modified from those published in Fitzsimmons 2017, Toner 2009, Gartman 2020, and Tagliabue 2017.

Non-buoyant plumes carry geochemical fluxes from vent fields to the deep ocean, where they have the potential to impact ocean biogeochemistry. There are various physical and chemical processes that can greatly modify these geochemical fluxes. How the fluxes are altered will depend on the chemical inertness and affinity for adsorption of the trace element. Dissolved noble gasses, for example, will undergo conservative dilution and dispersion within non-buoyant plumes due to their inert behaviour (Fitzsimmons et al. 2015; Jenkins 2020; Lupton and Craig 1981). Primordial dissolved ^{3}He is a fantastic tracer of hydrothermal activity due to both its conservative behaviour in the water column and because its only source to the deep ocean is through processes related to volcanic activity such as hydrothermal venting (German and Seyfried 2013). The large enrichments of dissolved ^{3}He found in hydrothermal plumes, relative to low seawater concentrations, have been used to trace hydrothermal activity, as was the case with Lupton and Craig (1981) who identified a pronounced ^{3}He plume dispersing over 2000 km across the Southern Pacific Ocean. Contrastingly, dissolved reduced gases such as hydrogen sulfide (H_2S) – the most abundant reduced gas in vent fluids – will be largely removed from the hydrothermal fluid upon venting (Mottl and McConachy 1990). The H_2S sourced

from vents will rapidly react with various metals (i.e, Fe) to precipitate polymetallic sulfide minerals (German and Seyfried 2013) which fall out of the buoyant plume.

Iron (Fe) and Manganese (Mn) are two of the most enriched metals in vent fluids and, unlike ^{3}He, are greatly influenced by vent fluid conditions. The fate of Fe is of particular interest due to the impact it has on hydrothermal fluxes. When hydrothermal fluids first vent, they are instantly cooled from temperatures >350°C to <30°C (German and Seyfried 2013), causing the rapid precipitation of Fe-rich metal sulfides.. The amount of Fe that precipitates will depend on the amount of sulphide present relative to Fe, or other chalcophile elements (element with an affinity to form a sulfide phase) such as Cu and Zn, with higher sulphide concentrations (German and Seyfried 2013). Observations from hydrothermal sediments indicate that up to 50% of the total dissolved Fe emitted from hydrothermal vents may precipitate rapidly, near (100's of meters) the source of venting (Mottl and McConachy 1990; Rudnicki and Elderfield 1993).

As the buoyant plume rises, entraining oxidizing seawater, Fe(II) is oxidized to Fe(III), which then precipitates as Fe oxyhydroxides (Mottl and McConachy 1990).The formation of Fe oxyhydroxides constitutes an important dispersal and/or removal mechanism for other particle reactive tracers including rare earth elements (REE) and oxyanions (vanadium, phosphorous, arsenic, uranium, chromium) (German et al. 1991), causing their co-precipitation or scavenging. The uptake of these tracers by Fe oxyhydroxides through adsorption and aggregation removes concentrations of them that far exceed the dissolved flux that enters the ocean (German and Seyfried 2013; Klinkhammer et al. 1983). Hydrothermal vents therefore act as a sink for these elements, rather than a source.

1.3.1 Iron in Hydrothermal Systems

High-temperature hydrothermal vents emit fluids with Fe concentrations several orders of magnitude greater than deep ocean dFe concentrations (~0.6 nM) (Bruland et al. 1994; Martin 1989; Fitzsimmons 2014). While initial studies of gross dFe flux from mid-ocean ridge high temperature and diffuse low temperature hydrothermal sites were neglected due to precipitation processes near the vent, several studies have have identified hot spots of Fe far from any hydrothermal vent sites (Fitzsimmons et al. 2017; Klunder et al. 2012; Wu et al. 2011). With the high concentrations (μM-mM) emitted from hydrothermal vents (Von Damm et al. 1985; Fitzsimmons 2014), any percentage of dissolved Fe (dFe) that is transported can have a major impact on ocean biogeochemistry.

Fe species in the water column can exist in two oxidation states: ferric (Fe(III)) and ferrous (Fe(II)) iron (Gonzalez-Santana et al. 2021; Meskhidze et al. 2019). In oxidizing conditions, Fe(II) will oxidize to form the more stable Fe(III) form. This oxidation causes Fe solubility to decrease reducing its bioavailability for plant uptake. For this reason, dissolved Fe(II) concentrations in the open ocean are generally very low (Gonzalez-Santana et al. 2021). Hydrothermal fluids however, are highly enriched in Fe(II). The transport of this dFe can be attributed to a number of mechanisms including uptake by microorganisms, complexation by Fe-binding organic ligands and Fe colloids, adsorption to and aggregation with particulate organic carbon (POC) (Hoffman et al. 2018; Wang et al. 2021), and the formation of Fe-bearing nanoparticles (Yücel et al. 2011). Each of these will work to stabilize hydrothermal dFe by either preventing precipitation or inhibiting Fe oxidation.

1.4 The Juan de Fuca Ridge

The Juan de Fuca ridge (JDFR) is an intermediate spreading centre located ~300 km off the coast of British Columbia. With a spreading rate of 6 cm/year, the JDFR separates the Pacific plate to the west from the Juan de Fuca plate to the east (Jamieson et al. 2014; Riddihough 1978). The Endeavour segment (47°N, 129°W) forms a 90 km long section at the northern end of the JDFR (Figure 5). The central portion of Endeavour forms a ~25 km long, 4 km wide volcanic ridge with a central high of 2050 m and 0.5-1 km wide steep-sided axial rift that deepens to the north and south (Karsten et al. 1986). Within this axial rift exists over 800 extinct and active chimney structures (Clague 2008), including five major vent fields (from north to south): Sasquatch, Salty Dawg, High Rise, Main Endeavour, and Mothra (Figure 5). Sasquatch and Salty Dawg are characterized by lower fluid temperatures (278°C and 305°C) and a smaller abundance of sulfide structures. High Rise and Main Endeavour are both vigorously venting fields with very high fluid temperatures (300-380 °C) ((Baker and Massoth 1987; Feely et al. 1992). Mothra, the southernmost vent field, has 6 large clusters of chimneys reaching up to 24 m in height (Kelley et al. 2012). Each of these vent fields are underlain by a large magma body, providing the heat source needed to leach metals from the crust into the seawater (Kelley et al., 2012). In addition, there are several smaller fields and distally diffusing vents scattered between.

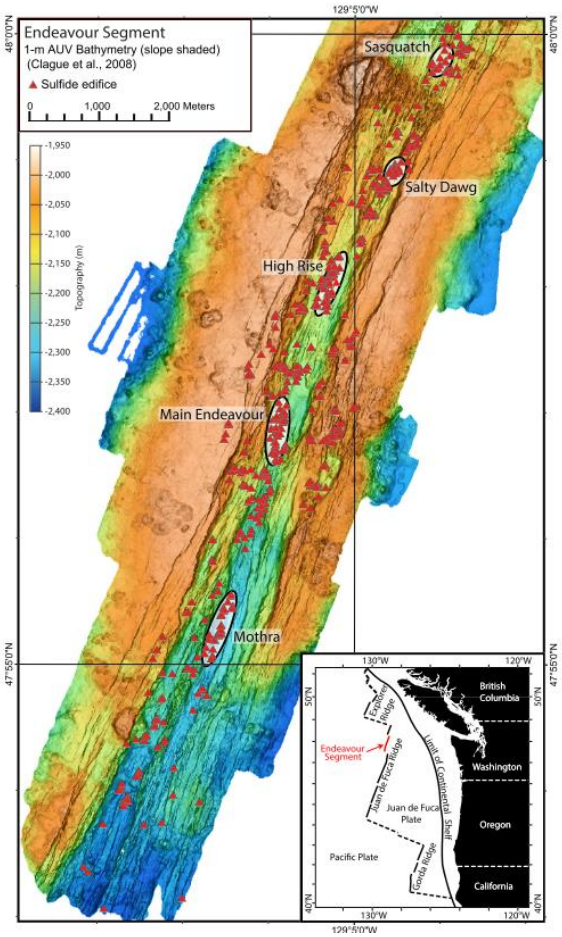

Figure 5. Map of the Endeavour segment of the Juan de Fuca Ridge. Figure from Jamieson 2014.

Significant efforts have been invested in studying the hydrothermal activity, hydrothermal plumes, and sediments at the Endeavour segment (Baker and Massoth 1987; Thomson et al. 1992). In 1985, Baker and Massoth (1987) mapped the regional distribution of non-buoyant plumes originating from two vent fields on the southern end of Endeavour. Temperature and light attenuation anomalies of 0.02-0.05°C and 0.01-0.08 m^{-1} respectively, pointed to the coalescence of several fluid emissions into one, large 200 m think non-buoyant plume traveling in the direction of current flow, 100-200 m above the seafloor (Baker and Massoth 1987). Feely et al. (1992) furthered this research by using hydrothermal plume suspended matter to track its dispersal. The Endeavour non-buoyant plume was found to be centred around 2000 m and spread to the southwest. Hydrothermal plume particulates were enriched in Si, P, V, Mn, Fe, Cu, Zn, and As. Average elemental concentrations of suspended particulate material for the Endeavour segment and JDFR (South Cleft, North Cleft, and Endeavour combined) can be found in Table 1. In addition, detailed studies on the composition of vent particles along the Endeavour segment indicate a mineralogy of anhydrite, chalcopyrite, sphalerite, barite, sulfur, pyrite, marcasite, pyrrhotite, isocubanite and magnetite (Feely et al. 1992).

Table 1. Elemental concentrations for the Endeavour segment of the Juan de Fuca Ridge from suspended particulate matter taken between 1800-2800 m from the non-buoyant plume. Values obtained from Feely et al. (1992).

Element	Endeavour segment (nmol/L)	Average JDFR (nmol/L)	Northeast Pacific Deep Ocean (nmol/L)
Al	13.9 ± 1.1	11.4 ± 2.2	6.3 ± 0.7
Si	99.2 ± 6.3	80.0 ± 18	25.3 ± 3.7
P	21.9 ± 1.2	23.8 ± 5.1	0.44 ± 0.2
Ca	32 ± 2.4	34 ± 5	33.8 ± 3.1
V	0.24 ± 0.03	0.26 ± 0.04	0.013 ± 0.007
Mn	1.11 ± 0.05	1.27 ± 0.14	0.11 ± 0.02
Fe	102 ± 5.3	102 ± 23	2.7 ± 0.4
Cu	2.97 ± 0.03	1.3 ± 1.4	0.22 ± 0.1
Zn	0.92 ± 0.05	0.7 ± 0.2	0.29 ± 0.08
As	0.18 ± 0.02	0.2 ± 0.05	< 0.003

In addition to being chemically complex, the Endeavour segment is home to abundant seismic activity likely due to the constant reorganization of plate boundaries in the region (Kelley et al. 2012).There have been three major seismic events during the last two decades, each of which have had an impact on the venting temperature, intensity and chemistry. In June of 1999 and January 2000, strong melt pulses and seismic swarms resulted in a significant increase in chimney growth, vent fluid temperatures, volatile concentrations and flocculent output (Kelley et al. 2012; Seyfried and Shanks 2004). The injection of a 40 km long, 3 km deep dyke in 1999 caused dramatic increases in venting temperature, causing elevated release of CO_2, boiling, and the emission of low salinity vapors (Johnson et al. 2000; Kelley et al. 2012; Lilley et al. 2003). In addition, this event altered gas concentration variability between vent complexes, as exemplified in the differences between the vents Sully and Hulk. While these vents are close in proximity, following dyke injection these vents exhibited vastly different gas compositions. These two vent complexes are likely fed by different fluid sources along different upwelling limbs, segmented along the ridge by the 1999 event (Kelley et al. 2012). The third event, two complex swarm sequences involving progressive north-to-south seismicity, occurred in February of 2005 (Kelley et al. 2012). Recorded evidence indicates that these sequences involved magmatic intrusions on the northern end of the Endeavour segment, and deformation within the spreading centre.

1.5 Introduction to Thesis

The objective of this thesis is to quantify trace metal chemistry of the Main Endeavour Field non-buoyant plume and assess the processes impacting trace metal flux. Chapter 2 focuses on Fe and Mn distribution and transport. Concentrations are compared to that of vents in varying locations and size fractionation is used to assess the impact processes including precipitation, oxidation, and sedimentation have on the fate of these trace metals. Dilution factors and trace metal inventories are empirically estimated and compared to determine the impact mixing with seawater has on Fe and Mn inventories. Chapter 3 focuses on the distribution of chalcophile elements (Cu, Zn, Cd, Co, Pb), with an emphasis on stations proximal to the main vent field. This is paired with previous studies on hydrothermal sediments and sedimentation rates of the Main Endeavour Field to correlate removal processes occurring in the plume with the geochemistry of sediments below.

Chapter 2: Iron and Manganese distribution in the Endeavour Non-buoyant Plume

2.1 Introduction

The high temperature fluids emitted from hydrothermal vents are produced from the circulation of seawater through ocean crust. During its interaction with crust, the seawater is heated and becomes chemically altered (Baker et al. 1995; James and Elderfield 1996). This fluid can become supercritical and ultimately vent back into the ocean, producing hydrothermal plumes that carry chemical anomalies relative to the surrounding bottom waters. Hydrothermal activity is an important source of trace metals to the deep ocean and can impact global biogeochemistry 10-10^3 kms away from the site of venting (Fitzsimmons et al. 2017; Hoffman et al. 2018). Among the metal enrichments identified and transported in hydrothermal plumes are dissolved and particulate iron (Fe) and manganese (Mn). The fate of Fe and Mn are of particular interest given their importance as essential, and often limiting, nutrients in the ocean that can modulate primary productivity and impact the biogeochemistry of the major elements C, N, S and P (Ardyna et al. 2019; Fitzsimmons et al. 2017; Wang et al. 2019, 2021).

Several studies have identified and tracked hydrothermally derived Fe and Mn penetrating up to 10^3 kms into the Pacific (Klinkhammer 1980, Klinkhammer 1986, Fitzsimmons 2014), Atlantic (Conway and John 2014), Southern (Ardyna et al. 2019; Klunder et al. 2012), and Indian (Nishioka 2013; Sands et al. 2012) Ocean interiors. The impact hydrothermal Fe and Mn will have on ocean biogeochemistry will depend on the amount supplied by the vent field, metal speciation, and processes that operate within the non-buoyant plume (NBP) (Jong et al. 2007). The persistence of Fe and Mn within the NBP and subsequent transport within the ocean is likely related to several processes operating in concert. The stabilization of Fe and Mn in the dissolved phase can occur through the formation of nanoparticles, which would prevent loss due to settling. Additionally, complexation by organic ligands, colloids, and adsorption to/aggregation with dissolved organic carbon can also work to either prevent precipitation, inhibit oxidation, or prevent removal by settling (Fitzsimmons et al. 2017; Hawkes et al. 2013; Statham 2005).

While there have been several studies conducted on the long-range transport of hydrothermally derived trace metals to the ocean interior (Fitzsimmons et al. 2014; Gartman and Findlay 2020; Hawkes et al. 2013; Resing et al. 2015; Tagliabue et al. 2022), there are still questions surrounding the processes that act to remove or retain Fe and Mn within the NBP. Understanding the mechanisms that control their exchange between the dissolved (<0.2 μm) and particulate (>0.2 μm) size fractions, as well as the complex processes that operate within the NBP (adsorption, oxidation, scavenging, co-precipitation, complexation) will be important for assessing the impact hydrothermal systems have on the Fe and Mn ocean inventory.

Here, observations of Fe and Mn concentrations in the Endeavour non-buoyant plume obtained during a September 2021 expedition (Figure 6) to the Endeavour Segment of the Juan de Fuca ridge are reported. An analysis into the size fractionation of Fe and Mn, as well as the reversible exchange processes which impact their persistence and removal from the non-buoyant plume is presented. Data is used to derive oxidation half-lives and estimate total Fe and Mn inventories at each station.

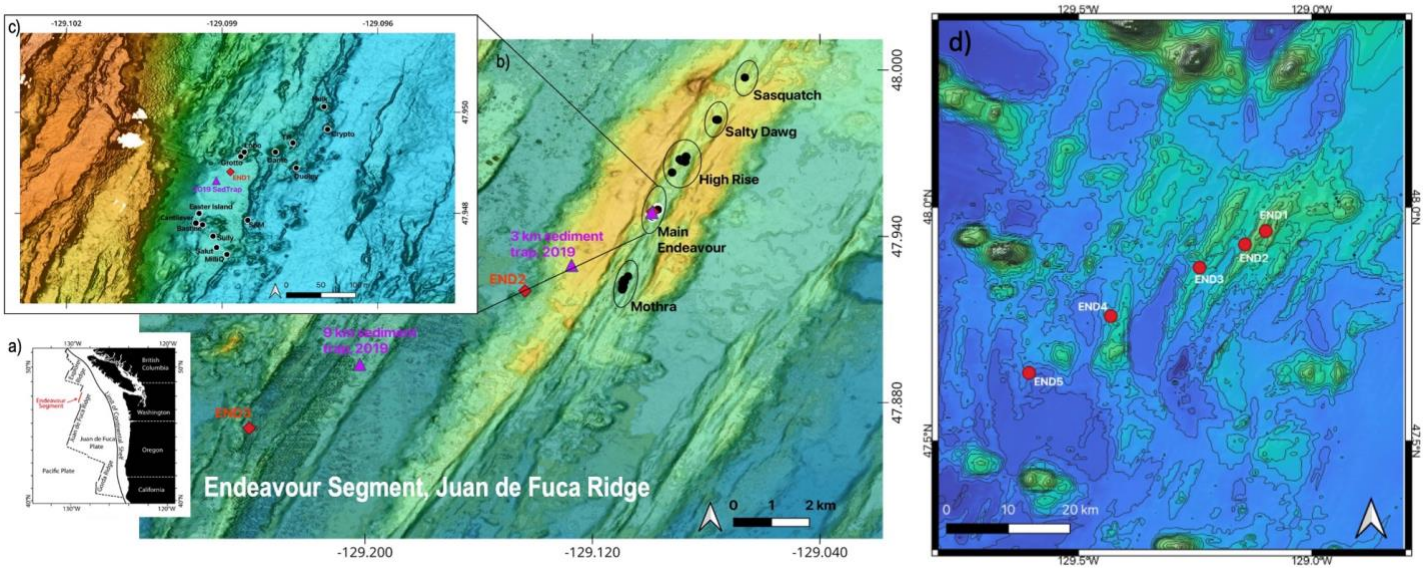

Figure 6. a) Endeavour segment, Juan de Fuca Ridge (inset map from Jaimeson 2013). b)Black points indicate individual vent edifice, red points represent station locations, purple points represent sediment trap locations (Mills 2023). Sampling transect (c,d) starts on-axis (END1) and extends 45 km southwest (END5). Gridded bathymetry data obtained from the General Bathymetric Chart of the Oceans (GEBCO) and Kelley 2002.

2.2 Methods

2.2.1 Sample Collection

Seawater samples were collected at a series of stations to characterize the impact of the Endeavour Hydrothermal Vent complex on trace element distributions in the subsurface waters of the subarctic northeast Pacific (Figure 6). Samples were collected on the *CCGS J.P Tully* between September 10-12, 2021. The sampling transect and depths were pre-determined using historical CTD data obtained from the Marine Geosciences Database. Deviations in temperature, particle concentration (determined by transmissometry), and reduction-oxidation potential (Eh) were used to identify the depth and location of the hydrothermal plume. We occupied five stations along a transect from the Endeavour Hydrothermal Vent complex starting at Main Endeavour (47.968, -129.087) and proceeding southwest (Figure 6). Sampling was conducted at 25 m depth intervals between the depths 1900-2200 m to capture waters influenced by hydrothermal fluids.

Collection of hydrographic information and seawater was performed using a Trace Metal Rosette (TMR) system consisting of a 12-position powder coated rosette frame equipped with 12 L Teflon coated Go-Flo (General Oceanics, Miami, USA) bottles, and a SeaBird 911 conductivity, temperature, and depth (CTD)/SBE 43 Oxygen sensor instrument package (Measures et al. 2008). An Autonomous Plume Recorder (Pacific Marine Environmental Laboratory Miniature, MAPR) equipped with temperature, pressure, optical backscatter and oxidation-reduction potential (ORP) sensors was mounted on the base of the rosette frame. Immediately following retrieval, Go-Flo bottles were removed from the rosette and placed on racks inside a HEPA filtered 10ft container modified for trace metal sampling.

Water samples were collected into 500 mL low density polyethylene (LDPE) bottles, which were pre-cleaned according to GEOTRACES protocols (https://www.geotraces.org/methods-cookbook/). Sample tubes were pre-cleaned in the lab and were stored filled with 1 N HCl until use. Prior to sampling, each bottle was emptied and rinsed three times using an aliquot of the sample water. Unfiltered seawater was collected to determine total acid soluble metal concentrations (TPM, >0.2 μm). Seawater was gravity filtered through a polysulfone-ester membrane filter (0.2-μm Acropak capsule, Pall corporation) connected to Go-Flo's using Teflon tubing for subsequent determinations of total dissolved metals (TDM, <0.2μm). Seawater samples were acidified by volume in a HEPA-filtered flow hood with 12 N HCl to a final pH of ~1.7 to prevent particle precipitation during storage.

Additional unfiltered seawater sampling was conducted using a 24-Niskin bottle rosette equipped with a CTD, oxygen, and PAR sensors. Seawater samples were analyzed for dissolved oxygen, nutrients, and dissolved inorganic carbon by researchers at the Institute of Ocean Sciences in Sidney, British Columbia.

2.2.2 Reagents and Standards

All reagents, blanks, and standards were prepared in a Class 100 laminar flow hood located in a Class 100 clean room using ultrapure deionized water (MQW) from a Milli-Q Element system (Millipore, Darmstadt, Germany). A multi-element stock standard was prepared using open-ocean surface seawater (Line P, subarctic northeast Pacific) and multi-element standard spikes (High Purity Standards, SC, USA) and was acidified to pH ~1.6 using ultrapure 12 N HCl (SeaStar Chemicals, Sidney, BC, Canada). From this stock, six multi-element standards were prepared using differing volumes of stock solution and 60 g of acidified (pH ~1.6) open-ocean seawater . Additional iron (Fe) and manganese (Mn) standards were prepared using single element standards (High Purity Standards, SC, USA), open-ocean seawater, and ultrapure 12 N HCl to ensure coverage of predicted sample concentration ranges.

Reagents used for sample pre-concentration included a 2 N ammonia acetate (NH_4Ac) buffer, a 10% HNO_3 eluate, and a 0.1% ultrapure HCl rinse solution. The NH_4Ac solution (pH 6.0) was prepared by mixing 390 mL of MQ and 70 mL NH4Ac. The eluting solution was prepared with 148.29 g HNO_3, 200 μL rhodium (Rh) internal standard, and was diluted to 1 L using MQW. A rinse solution was prepared by mixing 4000 mL MQW and 4 mL ultrapure HCl. The certified reference standard NASS-7 (National Research Council, Canada) and an in-house reference material of seawater from Line P in the subarctic northeast Pacific were analyzed alongside the pre-made internal standards with each batch of seawater samples (Table 2). Blank solution was prepared using open-ocean seawater, ultrapure HCl and MQW, and was run every 6 samples.

Table 2. Average blanks, detection limits, and reference materials for the trace metal analysis of hydrothermal plume samples.

	Blank n=12	Detection Limit n=8	In house Reference Material n=4	NASS-7 Measured n=2	NASS-7 Consensus
Fe (nmol/L)	0.159	0.378	0.58 ± 0.11	6.6 ± 0.1	6.3 ± 0.5
Mn (nmol/L)	0.023	0.028	1.04 ± 0.05	14.1 ± 0.01	13.6 ± 1.1
Ni (nmol/L)	0.030	0.148	5.66 ± 0.13	4.4 ± 0.1	4.2 ± 0.3
Cu (nmol/L)	0.034	0.082	2.22 ± 0.20	3.3 ±0.001	3.1 ± 0.2
Cd (nmol/L)	0.0005	0.002	0.10 ± 0.01	0.13 ± 0.002	0.14 ± 0.01

2.2.3 Extraction and Analysis

2.2.3.1 Preconcentration

Acidified seawater samples were pre-concentrated using a seaFAST-pico SC4-DX solid phase extraction system (Elemental Scientific Inc., Omaha, NE, USA**)** fitted with a Nobias-1 resin column (Elemental Scientific) consisting of ethylenediaminetriacetic acid and iminodiacetate functional groups for cation binding. A preconcentration factor of 12.5x was achieved by eluting 10 mL of acidified seawater with 800 μL of 10% HNO_3. Extraction followed the procedure below, based on the procedures of Jackson et al. (2018) and Sohrin et al. (2008)**.** SeaFAST instrument parameters used in this study can be found in Table 3.

1. The sample, buffer and eluent lines are cleaned with an ultrapure 0.1% HCl rinse solution.
2. 10 mL of acidified seawater sample is loaded onto the sample loop and the buffer line is filled.
3. Sample and buffer are mixed using syringe pumps and is pushed through the column, selectively binding metal ions.
4. The column is rinsed with MQW, removing unchelated matrix.
5. Elution acid (10% HNO_3) is pushed through the column, eluting the trace metals from the column into pre-cleaned vials.
6. Rinse solution (ultrapure 0.1% HCl) is pushed through the column to condition the column for the following sample.

Table 3. SeaFAST preconcentration parameters used for the analysis of trace metals from hydrothermal plume samples.

Parameter	
Mode of analysis	Offline
Column resin	Nobias-1 EDTRiA and IDA groups
Buffer	2 M ammonia acetate buffer, pH 6.1
Eluent	10% HNO_3
Internal standard	10 ppb Rh
Sample pH	1.6
Preconcentration factor	12.5
Initial volume of sample	10 mL
Final elution volume	800 μL

2.2.3.2 Determination of Trace Metals with QQQ-ICP-MS

Pre-concentrated samples were analyzed using an Agilent 8800 triple quadrupole inductively-coupled plasma mass spectrometer (ICP-MS/MS) (Agilent Technologies) at the University of Victoria following the procedure outlined in Jackson et al. (2018). Instrumental parameters can be found in Table 4.

Table 4. ICP-MS parameters used for trace metal analysis.

Parameter	
Sample flow rate	1 L/min
Nebulizer flow rate	0.84 L/min
Auxiliary gas	0.7 L/min
Plasma gas	12-14 L/min

The accuracy of trace metal measurements by QQQ-ICP-MS was assessed by the use of reference materials, including certified reference standard NASS-7 (National Research Council, Canada) and an in-house reference material of seawater from Line P in the subarctic northeast Pacific (Table 2). Stability of measurements was maintained by the use of an indium internal standard, which was added to the eluent acid, and therefore contained in equal amounts in all blanks, standards, and samples. To ensure reproducibility of analysis, these reference materials were measured with each

sequence, where n = 3 per sequence. Standard error was calculated by taking the standard deviation of five replicate scans of each sample of the same preconcentrated solution.

2.2.4 Calculation of hydrographic anomalies

Previous measurements taken east of the axis, outside the influences of Endeavour, display a near-linear θ - salinity trend over the depth of the Endeavour NBP (Veirs, et al. 2006). Deviations from this relationship is considered the temperature anomaly (ΔT). To calculate the ΔT, a linear regression equation fit to the near-linear θ - salinity background data (Figure 7) of *Line P* station P12 between 1800-2200 m depth (*Water Properties*), where:

$$\Delta T = \theta - (-5.9125 * Salinity) - 206.29$$

Similarly, transmissometer data from END5 for the same water column depth was used determine a background light attenuation (Δc). The increase from this background value is the determined Δc.

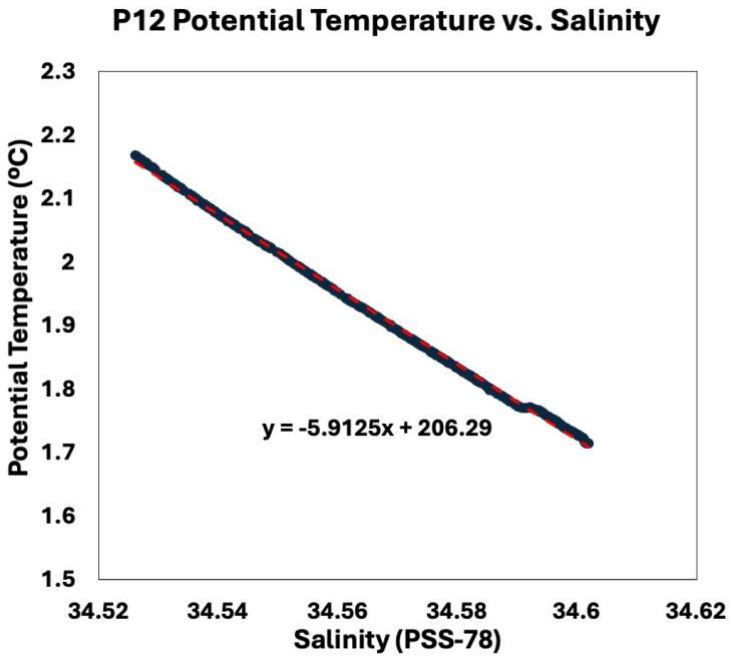

Figure 7. Linear relation between potential temperature and salinity of station P12 between 1800-2200 m depth.

2.3 Results

2.3.1 Hydrography

Physical properties of seawater including potential density, potential temperature, salinity, dissolved oxygen, and light attenuation are used to monitor observed hydrothermal activity. The dissolved oxygen (O_2), potential temperature (θ), salinity (S) and potential density (σ_θ) profiles between 1700 m and 2200 m at each station are shown in Figure 8 to identify and localize the Endeavour non-buoyant plume. The σ_θ, θ and S at END1 all showed the highest values between 2100-2200 m, the depth range identified as the NBP at 27.6-27.675 kg m^{-3}, 1.8-2.1°C, and 34.56-34.64 (PSS-78) respectively. The anomalies observed at the height of the plume are more heterogeneous at END1 in comparison to following stations as these measurements were taken in the axial valley, directly above the Main Endeavour Field. NBP associated anomalies decrease significantly off-axis, with only T anomalies being observed at END2 and 3. Once 35 km to the southwest (END4) is reached, there is no discernable plume signal.

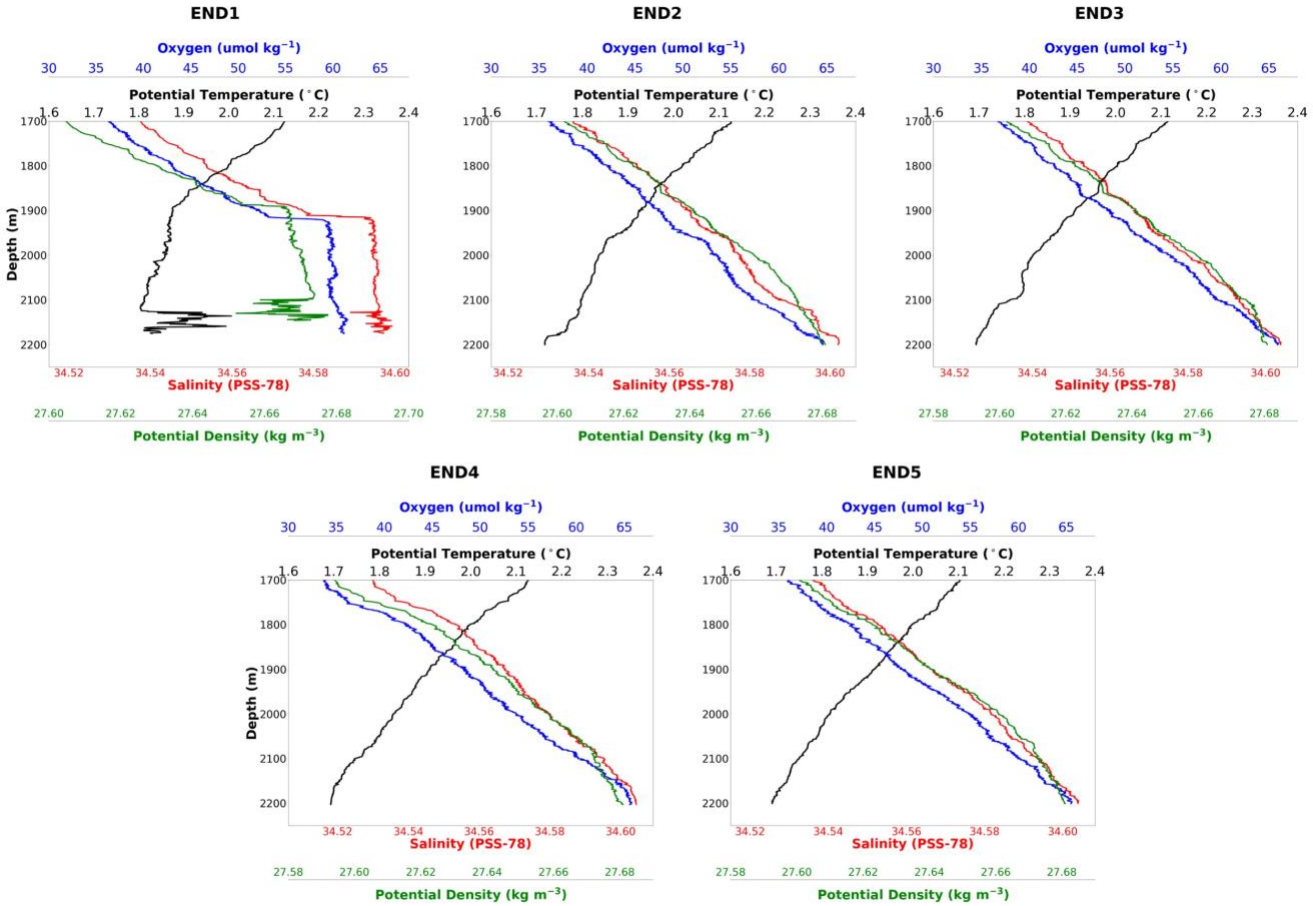

Figure 8. Vertical profiles of oxygen (umol kg^{-1}, blue), potential temperature (℃, black), salinity (PSS-78, red), and potential density (kg m^{-3}, green).

Vertical profiles of potential temperature anomaly (Δθ) and light attenuation anomaly (Δc) (Baker and Massoth 1987; Thomson et al. 1992) in the NBP are shown in Figure 9. These anomalies allow us to identify the location of the plume and track the movement of the plume, shipboard. The presence of a hydrothermal plume signature at END1 is clearly shown in both Δθ and Δc at two separate depth ranges. Between 1900 to 2000 m, values of Δθ reach 0.10 °C and Δc reach 0.2 m^{-1}. At 2100-2200 m, a maximum of 0.27 °C and 0.18 m^{-1} are observed.

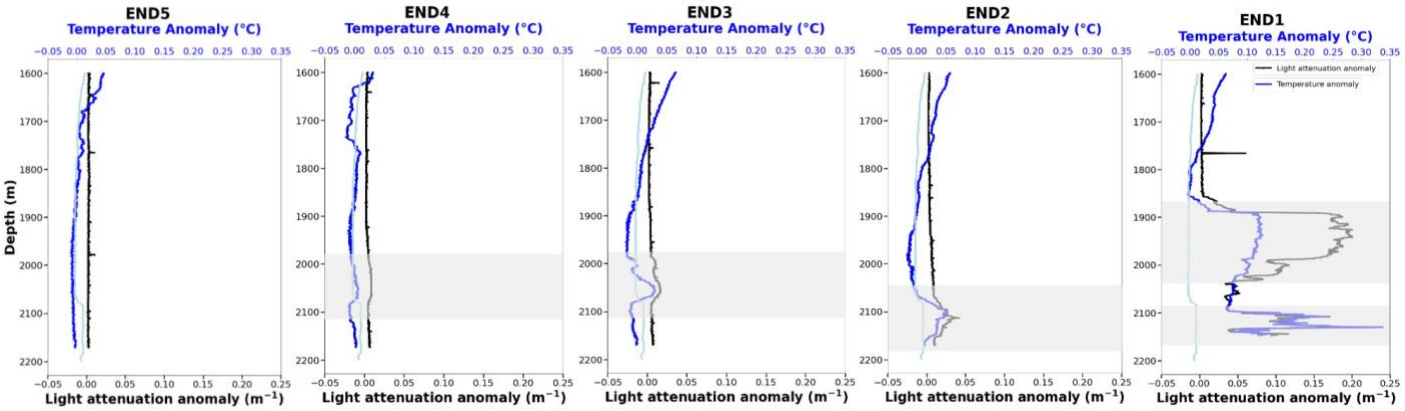

Figure 9. Vertical profile of temperature anomaly (blue) and light attenuation anomaly (black) for each station. From right to left, END1 through 5, on to off-axis. Light blue profiles represent temperature anomaly at station P12.

As the plume moves off-axis the intensity of the anomalies decreases due to mixing with ambient seawater. Clearly defined temperature and light attenuation anomalies are observed up to 30 km off-axis between 1950 – 2100 m with Δθ and Δc values reaching 0.075 °C and 0.017 m^{-1} at END3, and 0.063 °C and 0.01 m^{-1} at END4, while anomalies at END2 (0.9 °C and 0.04 m^{-1}) are observed at 2050-2200 m. Once 50 km off-axis (END5) is reached, Δθ and Δc values have decreased significantly with average values being 0.05 °C and 0.002 m^{-1} respectively, making it difficult to clearly identify the depth at which the non-buoyant plume was located using temperature and light attenuation alone.

Hydrographic anomalies suggest a plume at END2 that is sitting deeper in the water column than those at following stations. As advection spreads the NBP along isopycnal surfaces (constant density surfaces) (Baker and Massoth 1987; German and Seyfried 2013) the depth a plume core sits in the water column may vary depending on tidal cycles or topography, but its density surface will not. Plots of potential temperature and salinity with density (Figure 10) show that there are distinguishable differences in the isopycnal surface the plume lies on depending on the station. Hydrographic

anomalies observed closest to the main vent field (END1) span a range of density surfaces (27.665σ_θ - 27.635σ_θ), with a distinguishable plume core identified at ~27.655σ_θ (Figure 10). This suggests that the plume sampled at this station is likely relatively low density and moving vertically in the water column, entraining surrounding seawater and becoming denser with time, and is consistent with O_2 and salinity profiles (Figure 2). The plume core, where potential temperature anomaly is highest, appears at a slightly greater density (27.660 σ_θ), shown in the anomalies observed at END3 and 4. Plume signals at END2 however, appear on a different density surface (27.675σ_θ - 27.660σ_θ), suggesting it is a plume originating from a different vent, with a different hydrothermal fluid composition or venting temperature.

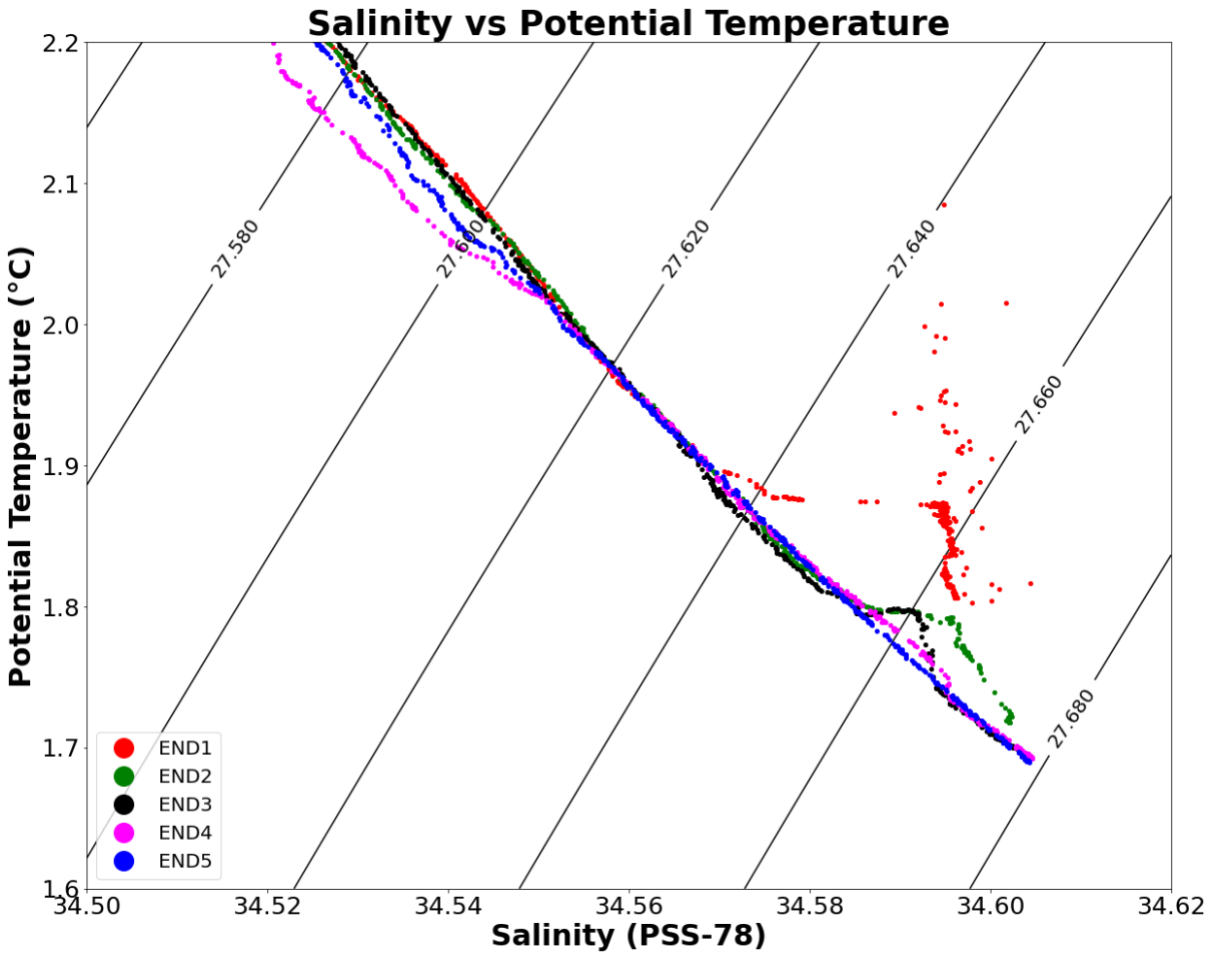

Figure 10. Potential temperature (℃) and salinity (PSS-78) plotted with potential density. END1 shows plume signals falling between 27.665σ_θ - 27.635σ_θ whereas a plume core can be identified at ~27.660σ_θ at END3-4.

2.3.2 Iron and Manganese

Vertical and section profiles of dissolved iron (dFe) and manganese (dMn) concentrations in the non-buoyant plume are shown in Figure 11. Both dFe and dMn concentrations show high values relative to expected background concentrations proximal to the MEF that decrease rapidly with distance off-axis. At END1, closest to the MEF in the axial valley, dFe and dMn concentrations are highest and, similar to hydrography data, show the presence of two plume signatures centred at different depths in the water column. A shallow plume at 1900-2000 m with metal concentrations ranging from 24 to 68 nmol kg^{-1} dFe and 46 to 98 nmol kg^{-1} dMn. The second plume is deeper in the water column, at 2050-2150 m, with concentrations ranging from 7.4 to 23 nmol kg^{-1} dFe and 12.6 to 50 nmol kg^{-1} dMn.

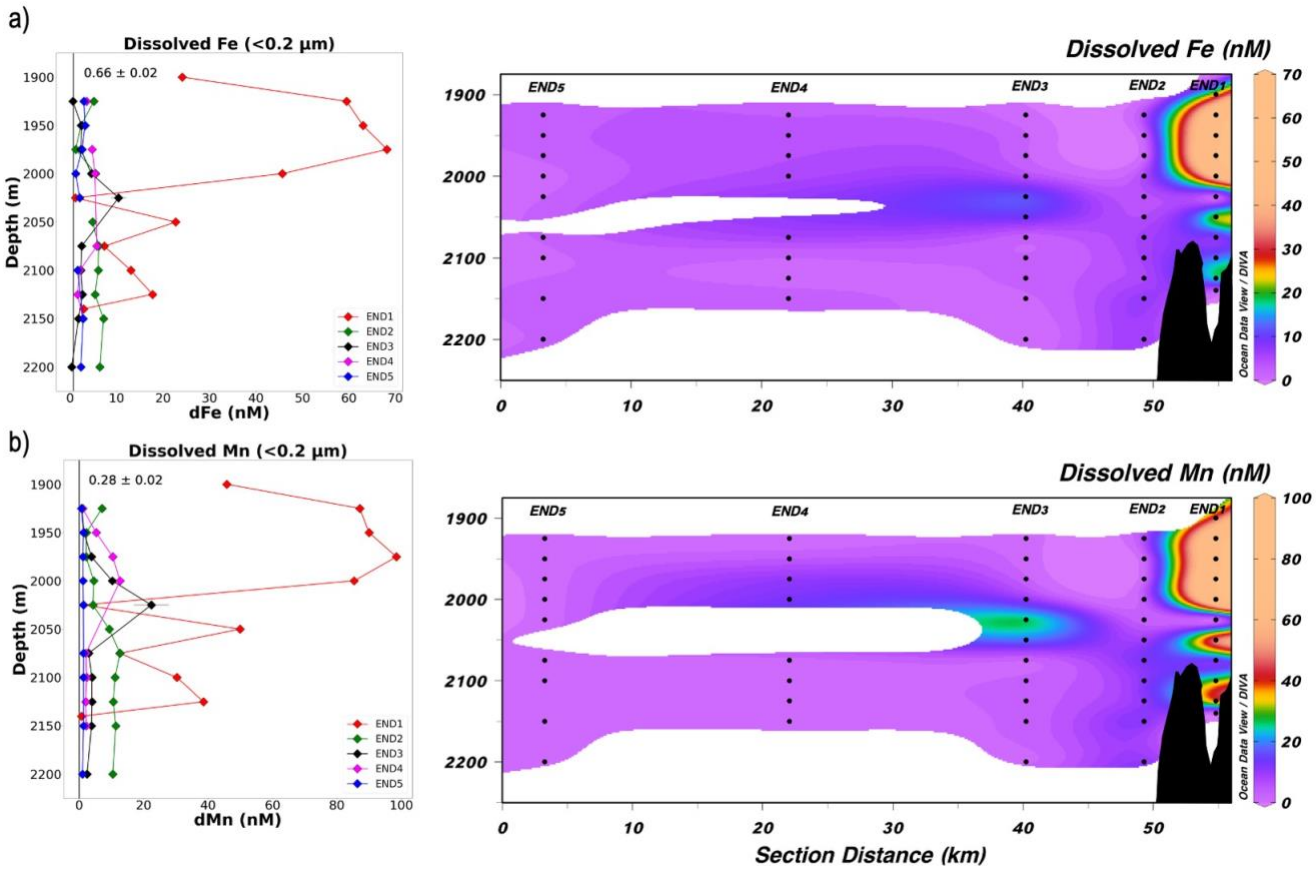

Figure 11. Profiles of dissolved (<0.2 µm) a) iron (nM) and b) manganese (nM) observed in the non-buoyant plume between 1900-2200 m. Black dots on section plots represent sampling depths. Vertical black lines represent the range of background Pacific seawater concentrations, obtained from Martin et al. (1989).

Five kilometers to the southwest at END 2, metal concentrations are ~10-fold lower in the deeper plume ranging from 4.9 to 7.2 nmol/kg dFe and 9.3 to 11nmol/kg for dMn. The presence of the shallow plume observed in the first station is not seen. At END3 and END4, 15 km and 30 km off-axis, signals consistent with the the shallow plume at END1 are observed. dFe and dMn concentrations range from 4.6 to 12 nmol/kg and 10 to 26 nmol/kg at END3 and 4.6 to 5.8 nmol/kg and 4.4 to 13 nmol/kg at END4. At END5, approximately 50 km off-axis, dFe and dMn concentrations diminish to between 1.2 and 2.9 nmol/kg and 0.76 and 1.4 nmol/kg through all measured depths but are still elevated compared to background Pacific seawater concentrations (0.66 ± 0.02 Fe and 0.28 ± 0.02 Mn).

2.3.2.1 Iron and Manganese size fractionation

Understanding how Fe and Mn are partitioned between dissolved and particulate fractions within non-buoyant plumes provides insight into their fate and degree of influence on deep water ocean chemistry. The size partitioning of total dissolvable Fe (TDFe) and Mn (TDMn) between dissolved (<0.2 μm) and particulate (>0.2 μm, estimated as a difference between total dissolvable and dissolved) fractions are shown in Figure 12. Near the MEF, the majority of Fe present is in the particulate form with pFe accounting for 52 to 76 % of the total Fe concentration at END1. The particulate phase remains dominant at all stations, extending 50 km off-axis. To test the statistical significance of changes in the proportion of dissolved and particulate Fe and Mn between near-field (END1) and far-field (END4-5) stations, two one-way ANOVA tests were conducted. Based on hydrographic and trace metal anomalies, it is assumed that those observed at END2 are not part of the same non-buoyant plume as following stations. END2 has therefore been omitted from this analysis. Each ANOVA test used the dissolved and particulate concentrations of either Fe and Mn from all sampled depths as inputs and tested the variance in concentration at each station against the variance between stations. The result of each ANOVA informs us whether there are statistically significant differences in the mean concentrations of Fe and Mn between sampling sites. Those with p-values below 0.05 (95% confidence interval) are considered statistically significant while those above this threshold indicate that differences in mean concentrations are likely due to random variation.

Results of the ANOVA test (Appendix E) show that the change in proportion of particulate and dissolved Fe and Mn is significant across two groupings: between. END1 and END5 and (to a lesser extent) between END3 and END5. In each, the percentage of TDFe present in the particulate phase slightly decreases and that of the dissolved increases with a statistical significance of 0.02 and 0.04

respectively (Figure 12a). This is consistent with the continual removal of trace metals from the non-buoyant plume due to particle settling and dilution within the sampled spatial scale. Generally, the amount of Fe in the pFe fraction is approximately double that in the dFe phase. There are two exceptions to this trend. The first are samples presumed to be at the upper and lower depth limits of the hydrothermal plume, where concentrations of both dFe and pFe are low and proportions are roughly equal. The second exception is at station END2, where there is no significant difference between dFe and pFe concentrations.

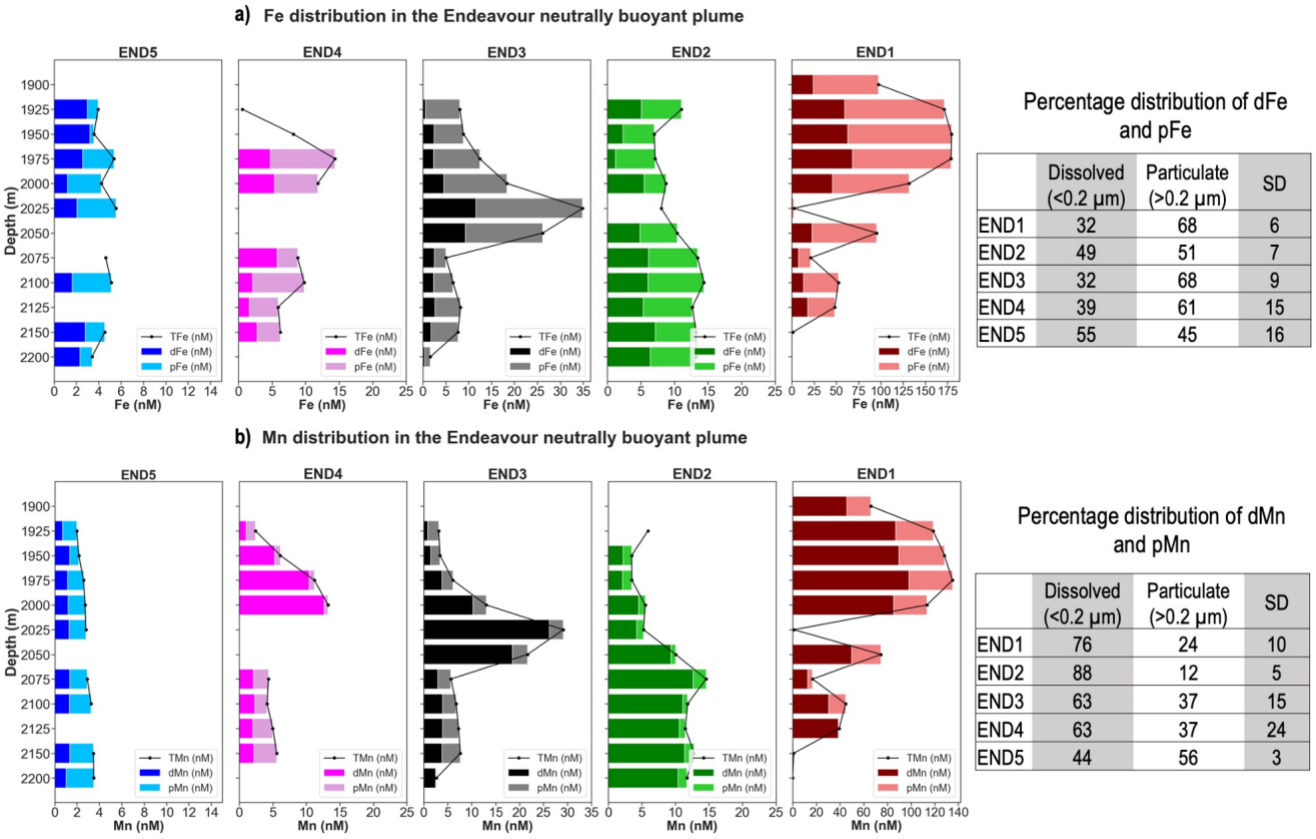

Percentage distribution of dFe and pFe

	Dissolved (<0.2 µm)	Particulate (>0.2 µm)	SD
END1	32	68	6
END2	49	51	7
END3	32	68	9
END4	39	61	15
END5	55	45	16

Percentage distribution of dMn and pMn

	Dissolved (<0.2 µm)	Particulate (>0.2 µm)	SD
END1	76	24	10
END2	88	12	5
END3	63	37	15
END4	63	37	24
END5	44	56	3

Figure 12. a) Iron and b) manganese particle size fractionation and percentage distribution between particulate (>0.2 µm) and dissolved (< 0.2 µm) size fractions. Black dots indicate total trace metal concentrations. Depths with no data are due to Go-Flo bottle malfunction, while those with just a total concentration value contained a dissolved load sample not used due to sample contamination.

Size partitioning of Mn was markedly different than Fe, with the dissolved fraction dominating TDMn concentrations close to the vent. At END1, 67 to 98 % of the total Mn is present in the dMn fraction, and 12 to 32 % as pMn. This remains true to END4, with the percentage of dMn decreasing moving away from the MEF. The concentration of dMn is roughly double that of pMn within the plume. Only at END4 and 5 does pMn exceed dMn.

2.3.2.2 Iron Oxidation

Considering the oxidation half-life of Fe in the plume is useful when considering the fate of Fe and other particle reactive elements during the chemical evolution of a hydrothermal plume. The oxidation of Fe(II) can be described using a pseudo-first order rate constant (k_1), and is shown in Equation 1:

$$-\frac{d[Fe(II)]}{dt} = k_1[Fe(II)] \quad (1)$$

This is a second-order function of pH (Millero 1987):

$$k_1 = k[O_2][OH^-]^2 \quad (2)$$

Giving the overall rate constant (k):

$$-\frac{d[Fe(II)]}{dt} = k[Fe(II)][O_2][OH^-]^2 \quad (3)$$

Where increased concentrations of Fe(II), oxygen, and higher pH will result in a faster oxidation rate. The overall rate constant (k) is a function of temperature (T) (in Kelvin) and salinity (S):

$$\log k = 21.56 - \frac{1545}{T} - \frac{3.29}{I^{\frac{1}{2}}} + 1.52I \quad (4)$$

Where I is the ionic strength of seawater, determined from S:

$$I = \frac{19.924S}{1000 - 1.005S} \quad (5)$$

To calculate the pseudo-first order rate constant (k_1), the $[O_2]$ (mol kg^{-1}) and $[OH^-]$ are needed. The $[O_2]$ was determined analytically by researchers at the Institute of Ocean Sciences in Sidney, British Columbia. The $[OH^-]$ was calculated using the relationship with the water dissociation constant (k_w):

$$K_w = [OH^-][H^+]$$

(6)

Seawater pH was determined using the program CO2SYS using alkalinity and total dissolved inorganic carbon (DIC). Several pH scales exist (NBS, free, total, seawater), each of which consider different ions when determining the hydrogen ion concentration. There exist slight numerical differences between these scales (values can differ by up to 0.12 pH units) (Wolf-Galdrow et al. 1999) therefore attention must be made to the pH scale adopted to maintain accuracy in calculations.

The seawater scale (SWS) takes the sulfate and fluoride ions into account, and was the scale adopted for these calculations. The ion product of water, K_w, on the SWS is a function of T and S at surface ocean pressures (Millero 1995):

$$\ln K_w^* = 148.9802 - \frac{13847.26}{T} - 23.6521 lnT + \left(\frac{118.67}{T} - 5.977 + 1.0495 lnT\right) S^{\frac{1}{2}} - 0.01615 S$$

(7)

To correct for pressure increases with depth, the following can be applied to K_w^*:

$$\ln \frac{K^*_{w,P}}{K^*_{w,P_0}} = -\frac{\Delta V^o}{RT}(P - P_0)$$

(8)

Where K^*_{w,P_0} is the dissociation constant estimated from T and S at surface pressure, $K^*_{w,P}$ is the dissociation constant at some depth corresponding to pressure (P), R is the gas constant, and T is temperature in kelvin (Millero 1995). The change in volume accompanying water dissociation (ΔV^o) is approximated to be constant (-19.506 $cm^{-3}mol^{-1}$), given partial molar volumes for H^+, OH^-, and H_2O reported in Poisson and Chanu (1980) and Millero (1995).

The pseudo-first order rate constant (k1 min^{-1}) is given by:

$$k_1 = k[O_2]\frac{K^*_{w,P}}{[H^+]_{SWS}}$$

(9)

The oxidation half-life time for Fe(II) in hours can be calculated with:

$$t_{\frac{1}{2}} = \frac{\ln 2}{k_1 60 \min hr^{-1}}$$

(10)

The data sources, equations, and parameters used in the calculation of Fe(II) half-lives are listed in the appendix. Rate constants and half-lives were calculated for 12 measured depths. Those falling within the height of the NBP were averaged for a representative half-life. The calculated Fe(II) oxidation half-lives are listed in Table 5.

Table 5. Calculated Fe(II) k1 values and oxidation half-life. Values are within error across all stations.

Fe(II) oxidation rate for the Endeavour non-buoyant plume

Station	Latitude	Longitude	pH_{sws}	k_1 (min^{-1})	Half-life (hour)
END1	47°56.94	129°05.93	7.75 ± 0.014	0.0019 ± 0.00024	6.25 ± 0.98
END2	47°55.22	129°08.62	7.73 ± 0.019	0.0016 ± 0.00033	7.28 ± 1.42
END3	47°52.25	129°14.44	7.74 ± 0.021	0.0017 ± 0.00034	7.00 ± 1.45
END4	47°46.03	129°25.85	7.74 ± 0.020	0.0017 ± 0.00034	6.86 ± 1.35
END5	47°38.75	129°36.33	7.74 ± 0.019	0.0017 ± 0.00032	6.94 ± 1.38

2.4 Discussion

2.4.1 Non-buoyant Plume Distribution

The hydrographic anomaly profiles reveal the presence of two particle-rich layers, between 1900 and 2000 m, and 2100 m and 2150 m, at the station closest to the main vent field (END1). A deeper plume (2100-2200 m) is observed 5 km off-axis, at END2, while chemical and hydrographic anomalies observed at off-axis stations (END3-5) are found between 1950-2100 m. The presence of two distinct hydrothermally derived particle-rich layers across different stations can be indicative of one of two processes (Rudnicki and Elderfield 1993; Sands et al. 2012).

First, as samples collected at END1 are immediately above the MEF and in the axial valley, the two particle-rich layers measured at this station may be a result of the heterogeneity of hydrothermal plumes as they establish neutral buoyancy. When high temperature hydrothermal fluids are expelled,

shear flow between the rising fluid and surrounding seawater creates turbulence, often producing eddies and vortices (German and Seyfried 2013). This turbulence can result in a plume having heterogeneity in its particle density profiles. Profiles of dissolved oxygen, θ, and density (Figure 8) provide further evidence that the samples taken at END1 are likely part of a buoyant plume phase that is experiencing active seawater entrainment. For example, unlike the steady increase in O_2 levels observed in far-field stations, END1 sees a sharp increase in O_2 concentrations from 55 μmol kg^{-1} to 63 μmol kg^{-1} at 1900 m, followed by relatively constant levels (~63 μmol kg^{-1}) between 1900-2200 m. An explanation for this observation is the entrainment of O_2 rich bottom water (60-65 μmol kg^{-1}) which is mixed and funneled up through the buoyant plume. The jagged nature of salinity, potential temperature, and density profiles between 2100-2200 m at END1 (Figure 8) supports this model.

As the height at which a non-buoyant plume is emplaced will be a function of water column stratification and individual vent fluid flux (Lupton 1995, Bennett et al. 2008), two vents situated proximal to each other might produce buoyant plumes which rise to different emplacement heights due to their individual venting intensity or topographic location (Bennett et al. 2008). Therefore, as the sample region is highly hydrothermally active with numerous clusters of active vents, the two signatures may be an indication that the two layers are the result of two different vent sources.

Plots of potential temperature and salinity with density (Figure 10) provide evidence that both of the above processes likely contribute to the plume cores observed across all stations. Hydrographic anomalies observed closest to the main vent field (END1) span a large range of density surfaces ($27.665\sigma_\theta$ - $27.635\sigma_\theta$) with a distinguishable plume core identified at ~$27.655\sigma_\theta$ (Figure 10). Plume signals at END2 however, appear on a different density surface ($27.675\sigma_\theta$ - $27.660\sigma_\theta$) compared to subsequent stations ($27.660\ \sigma_\theta$). These observations further support the model of a buoyant plume experiencing bottom water entrainment at END1, while END2 anomalies may reflect a plume originating from a different vent which could possess a markedly different hydrothermal fluid composition and/or venting temperature. The vent field Mothra is located ~2 km to the east of END2, making it closer than the MEF. With a markedly different fluid composition and temperature, mixing between the Mothra and MEF NBP may play a role in the differences observed at END2.

The profiles of hydrographic anomalies are consistent with previous measurements (Baker and Massoth 1987; Cave et al. 2002; Kadko et al. 1990; Thomson et al. 1992). Baker and Massoth (1987)

noted the presence of a 200 m thick plume at 1900-2100 m with temperature and light attenuation anomalies of 0.02-0.05°C and 0.01-0.08 m^{-1} respectively, while Kadko (1990) noted the presence of a plume core centered at 2000 m, with light attenuation anomalies reaching 0.371 m^{-1}. Slight differences in the water column depth and the magnitude of temperature and light attenuation anomalies observed between these studies and our data may be a reflection of temporal changes in the hydrothermal output or due to fluctuations in local current regimes (James and Elderfield 1996; Kadko et al. 1990; Massoth 1994) and can help explain differences in plume depth observed at different stations.

2.4.2 Plume particle formation and distribution

The Fe(II) oxidation half-life, as well as the size fractionation of trace metals can provide insight into how particles are formed during hydrothermal plume rise, horizontal transport and dispersion. Reversible exchange processes occurring between the dissolved and particulate phases play a role in Fe and Mn persistence in non-buoyant plumes detected thousands of kilometers away from the source of venting (Fitzsimmons et al. 2017; Fitzsimmons et al. 2014; Hawkes et al. 2013; Resing et al. 2015). Additionally, differences between Fe and Mn distributions and size partitioning in space and time may point to possible differences in the processes governing their transport.

2.4.2.1 Reversible exchange processes governing iron distribution

The general behaviour of Fe in the Endeavour plume is a decrease in the percentage of pFe and concurrent increase in the proportion of dFe moving from END1 to END5 ($p = 0.02$) (Figure 12). The high percentage of pFe observed proximal to the main vent field is likely a result of several processes. During the early stages of plume formation, rapid precipitation of sulfide minerals (e.g., pyrite, chalcopyrite, sphalerite) occurs due to the mixing of hot vent fluid and the cold surrounding seawater (Feely et al. 1992; Gartman and Findlay 2020). As the plume evolves, Fe(II) is rapidly oxidized forming Fe(III)-oxyhydroxide particles (Field and Sherrell 2000; Statham et al. 2005; Toner et al. 2009) further contributing to the observed increase in pFe. Increases in the particulate phase from vent sites to 1-3 km off-axis has been previously observed by Field and Sherrell in a non-buoyant plume over the East Pacific Rise (EPR), and hypothesized to be the result of vent derived Fe(II) being oxidized and forming colloidal Fe(III)-oxyhydroxides, which aggregate to form particulate Fe-oxyhydroxides (Field and Sherrell 2000). Therefore, the distribution of pFe in the near-field (within 5 km of the MEF, END1-2) plume is likely to result from the precipitation of Fe-bearing sulfides and the

concurrent oxidation of Fe(II) to form Fe(III)-oxyhydroxide particles, with continual plume dilution, which slows aggregation and sinking, playing a role in particle transport further off-axis. This corresponds with observed correlations between Fe and Δc at END1 (Figure 13), with higher proportions of the particulate phase and therefore larger concentrations of particles in the water column.

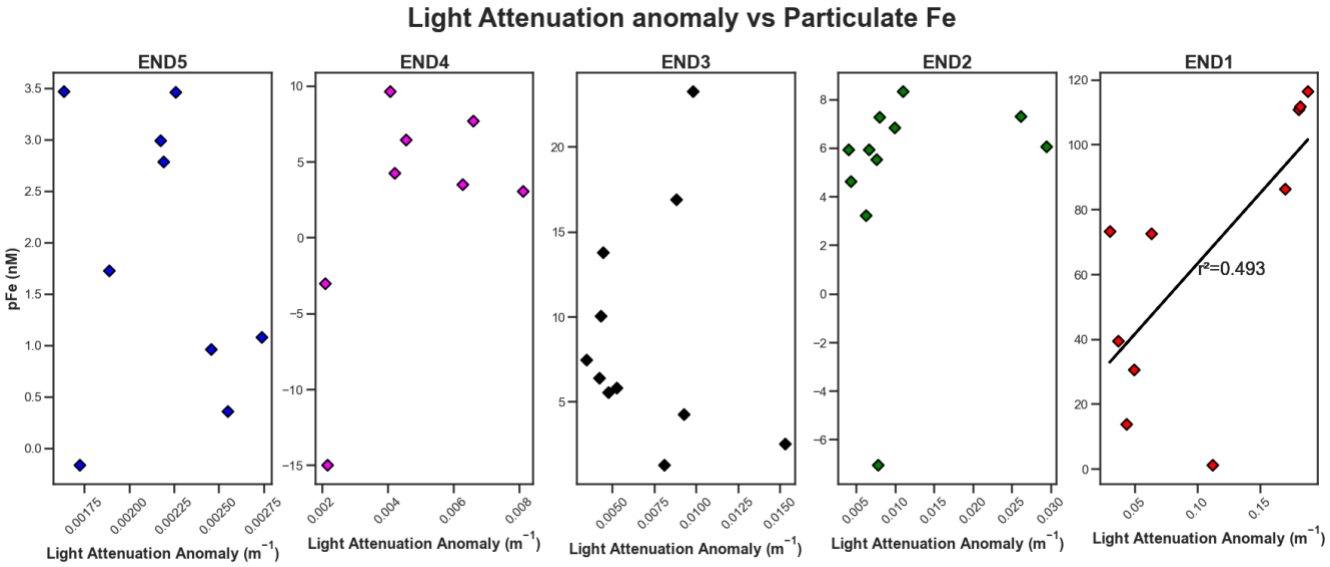

Figure 13. Particulate Fe vs light attenuation anomaly (Δc) for each station. Slight correlation is observed at END1 (r^2=0.49), while no correlation exists in subsequent stations.

Due to its slower oxidation rate when compared with Fe, dMn has previously been used as a near-conservative tracer of vent fluid dilution on short (hours-days) time scales (Cowen et al., 1990; Field and Sherrell 2000; James and Elderfield 1996; Massoth 1994). Correlations between Fe and Mn, or lack thereof, provide additional insight into the processes influencing trace element particle distribution and transport within the non-buoyant plume. Strong linear correlations of TFe with dMn (r^2=0.966) in the buoyant/early NBP (END1) indicate that the TFe pool is conservative with respect to dMn. The decrease observed in the TFe inventory will primarily be influenced by mixing and dilution during plume dispersion (Figure 13), while variations in pFe:dFe is due to conversions between the two size fractions (Field and Sherrell 2000). As the plume moves off-axis, the strength of the correlation between TFe and dMn decreases, suggesting a change in the dominant process impacting trace metal distribution. The particulate phase is likely to settle out quickly, while the dissolved pool may be impacted by scavenging and aggregation processes.

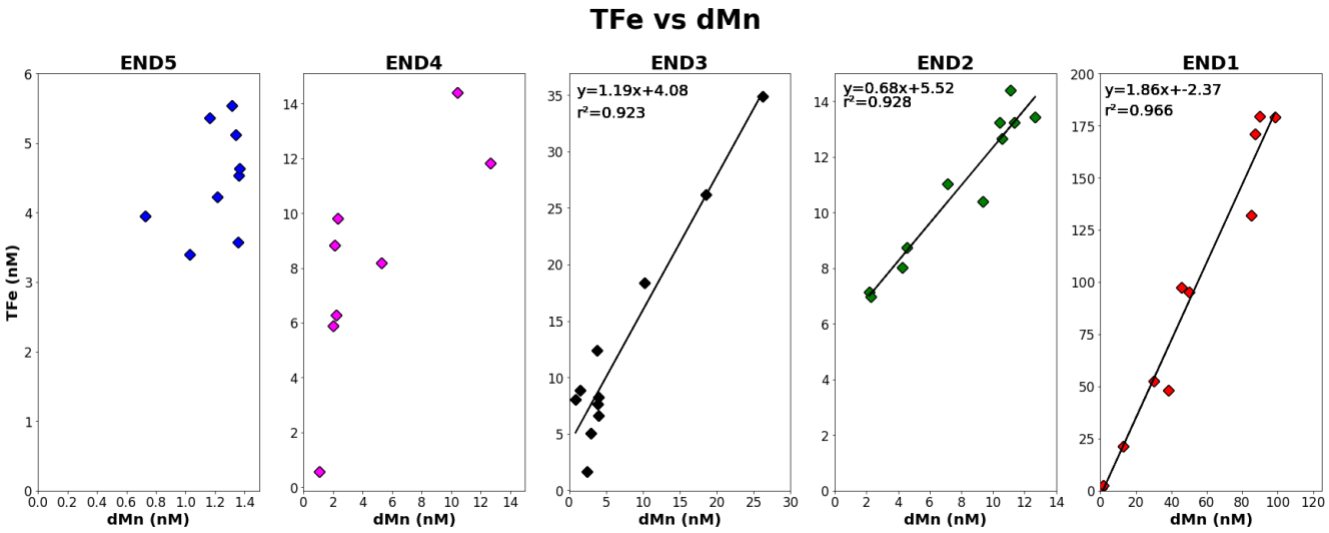

Figure 14. TFe plotted against dMn for each station. Strong linear correlations are observed in near-field stations (END1-3).

For example, Fe(III)-oxyhydroxides are known to scavenge trace metals from the water column (German and Seyfried 2013; Lee et al. 2021; Mandernack and Tebo 1993). Scavenging, which involves the adsorption of trace elements onto Fe-oxyhydroxide particles and their subsequent aggregation with other material in the water column (lithogenic, biogenic), creates larger sized particles that are more prone to settling out of the water column (Field and Sherrell 2000; German et al. 1990; Lee et al. 2021). The continual decrease in Fe concentrations in off-axis stations (END4-5) can be attributed to both the aggregation and sinking of these larger particles (Fitzsimmons et al. 2017) and continual mixing with background seawater.

To assess the impact that aggregation and sinking processes have on the Fe pool, the dFe/TFe can be considered as its variability will be controlled by changes in the fraction of dFe and/or pFe present. Increases in the dFe/TFe can indicate either diminishing TFe through pFe sinking or the dissolution of pFe into dFe, maintaining the TFe pool. Decreases in TFe are likely caused by the oxidation, aggregation, and sinking of dFe and Fe-sulfides (González-Santana et al. 2020), and dilution processes. The dFe/TFe (Figure 15) proximal to the vent (END1) shows little variation in the buoyant plume, with an average of 0.312 ± 0.06. Moving off axis, by 10 km (END3) and 30 km (END4), dFe/TFe are 0.323 ± 0.09 and 0.395 ± 0.15 respectively at the height of the non-buoyant plume. While changes in the dFe/TFe between individual stations are not statistically significant, those between near-field (END1) and far-field (END4 and 5) are, providing insight into the driving forces behind large scale TFe loss.

By the time far-field stations are reached, sufficient time has elapsed (~7 h, Table 5) that the majority of the Fe(II) present, not otherwise protected by ligand stabilization or present in Fe(II) nanoparticles (Toner et al. 2009; Yücel et al. 2011) has likely been oxidized into particulate Fe(III)-oxyhydroxides (Baker and Massoth 1987; Fitzsimmons et al. 2017; Gartman and Findlay 2020; German and Seyfried 2013; González-Santana et al. 2020) This would suggest that sinking and disaggregation of particulate Fe(III)-oxyhydroxides along with the presence of nano-particulate Fe-sulfides that is controlling the Fe pool. It is likely that both oxidation and aggregation processes play a role in particle loss, which is either fuelled/replaced by the continued loss from the dFe pool. This highlights both the complexity of hydrothermal systems and the need for additional research into the mechanisms that control trace metal transport in NBPs.

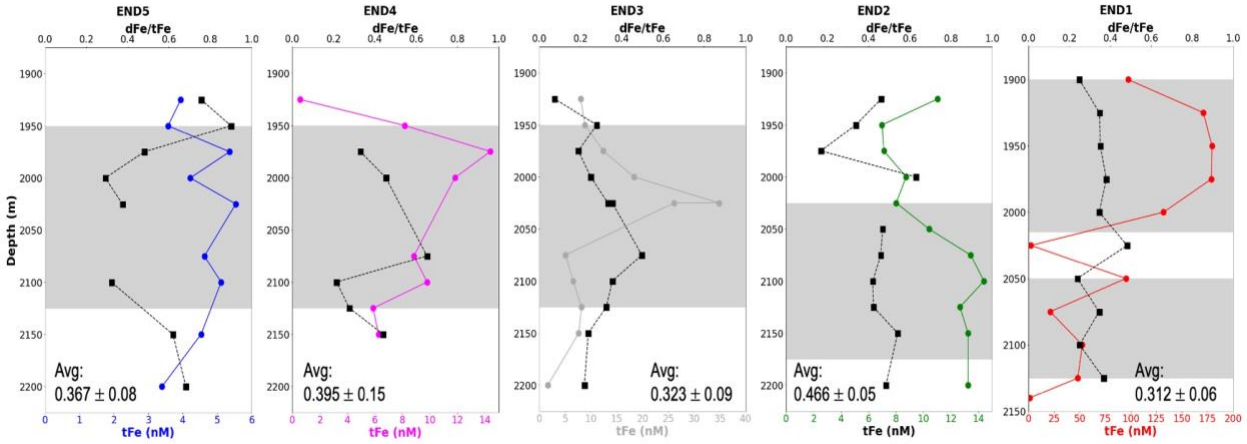

Figure 15. Vertical profiles of dFe/TFe (black, dashed line) and TFe. Greyed areas indicated the hypothesized non-buoyant plume. Average dFe/TFe are calculated for values that fall within the height of the non-buoyant plume.

2.4.2.2 Iron oxidation on particle formation

The total Fe flux that is transported away from the axial valley will be highly dependent on Fe(II) oxidation and Fe(III) particle formation. The rate at which Fe(II) will be oxidized is an important control on the rate of Fe-oxyhydroxide formation, with slower oxidation rates limiting the concentration of particulate Fe(III) observed in non-buoyant plumes, allowing dilution to limit aggregation and particle fallout (Field and Sherrell 2000). Rates of oxidation, which depend on both physicochemical and biological factors, can therefore be used to evaluate the degree to which dFe will remain within a non-buoyant plume.

The oxidation half-life of Fe(II) and subsequent formation of Fe(III)-oxyhydroxides will occur due to the mixing of seawater and hydrothermal fluids, and oxidative dissolution of sulfides (Coogan et al. 2019; Millero et al. 1987). It is highly dependent on bottom water oxygen and pH and will vary between ocean basins: 2.1 min in the oxygenated, high pH Atlantic to 7 hours in the less oxygenated, more acidic Pacific (Table 5; Field and Sherrell 2000; Millero 1987). Slower oxidation rates in the Pacific (Table 6) will result in higher amounts of plume dilution before Fe(II) is entirely oxidized to Fe(III), decreasing the chance of Fe oxyhydroxide nanoparticulate coagulation to form larger Fe oxyhydroxide particles with higher settling velocities (Field and Sherrell 2000; Statham et al. 2005). As a result, Fe(II) will survive longer, oxidizing within the non-buoyant plume, and be transported farther from the ridge axis. The ambient conditions found in the Atlantic however, will lead to faster oxidation rates, with most Fe(II) oxidation occurring closer to the vent, in the buoyant plume (Field and Sherrell 2000). This results in a shorter residence time for Fe in the non-buoyant plume, providing less Fe to the far-field ocean (Coogan 2019; Tagliabue et al. 2010).

The half-lives of Fe(II) (Table 5) calculated for the Endeavour non-buoyant plume were consistent across our stations, ranging from 6.25 h to 7.29 h. These slower rates are expected given Endeavour's location in the Pacific and are comparable to the 6.38 hours calculated for non-buoyant plumes along the Juan de Fuca ridge by Field and Sherrell (2000) (Table 6).

Table 6. Fe(II) oxidation half-lives for hydrothermal plumes around the globe. Data obtained from Field and Sherrell 2000 and Gartman and Findlay 2020.

Fe oxidation half-lives for global hydrothermal plumes

Location	Oxidation half-life (h)	Measurement method	Study
Kairei, Indian Ocean	2.3	Fe(II) spikes	Statham (2005)
SWIR, Indian Ocean	1.31	Calculated	Calculated by Field and Sherrell (2000), data from Toole (1999)
TAG, Atlantic Ocean	0.35	Bottles in plume	Rudnicki and Elderfield (1993)
TAG, Atlantic Ocean	0.45	Calculated	Calculated by Field and Sherrell (2000), data from WOCE

EPR (9°N), Pacific Ocean	3.3	Calculated	Field and Sherrell (2000)
EPR (21°N), Pacific Ocean	3.7	Calculated	Calculated by Field and Sherrell (2000), data from Taft (1999)
Juan de Fuca, Pacific Ocean	6.38	Calculated	Calculated by Field and Sherrell (2000), data from Musgrave (1999)
Gorda, Pacific Ocean	3.1	Calculated	Field and Sherrell (2000)
Cleft segment, Juan de Fuca, Pacific Ocean	9	Calculated	Coale (1991)
Main Endeavour Vent field, Juan de Fuca, Pacific Ocean	6.9 ± 1.3	Calculated	This Study

In near-field stations (END1-3), dFe is removed from the plume to a greater extent compared to dMn with the peak dFe concentration decreasing by 83% compared to the 73% decrease seen in dMn. This may be due to two processes. The only 10% difference between dFe and dMn removal suggests that dilution may be dominating the removal of each. However, as particle formation is one of the major controls on the decrease in the dissolved fraction (the second being mixing with background seawater), the precipitation of Fe-oxyhydroxides may be greater than the precipitation of Mn-oxides (Lee et al. 2021). Considering the ~7 h half-life calculated for the Endeavour non-buoyant plume (Table 5), it is likely that the high removal rate of dFe is driven by the oxidation of Fe(II) and precipitation of Fe-bearing mineral phases (sulfides and oxyhydroxides), with mixing processes playing an important role as well.

A first order approximation of the impact oxidation has on particle formation extending away from the vent field can be calculated using the determined half-life and measured concentrations (Statham et al., 2005). If the half-life calculated (average of 6.87 +/- 0.38 h) is applied to the maximum concentration observed at END1 (179 nM) over a period of 8 half-lives (54.94 h), 99% of the Fe

present will have been oxidized to Fe(III) phases reaching typical Pacific deep water dFe concentrations. While flow in the axial valley is not simply uni-directional, current speeds can be used to estimate the extent to which oxidation will impact Fe concentrations. Using deep water current speeds measured at the Endeavour ridge (~5 cm/s, Thomson et al., 2005), the maximum distance traveled before all Fe is oxidized is calculated at ~9.89 km. This would suggest that the majority of Fe(II) has been oxidized by the time END3 is reached. We know, however, that higher than background dFe concentrations persist past this station. There have been several proposed mechanisms for Fe stabilization in the dissolved phase. The small size of Fe-bearing nanoparticles (accounting for 5-25% of the dFe in global vent fluids, Fitzsimmons 2014) would result in very slow sinking, allowing for Fe to be transported away from the vents. Fe may also be bound to organic ligands and compounds, protecting it from precipitation and oxidation, thus stabilizing it in the dissolved form (Bennett et al. 2008; Fitzsimmons, Boyle, and Jenkins 2014; Hawkes et al. 2013; Tagliabue et al. 2022). Each of these processes are likely at play within the Endeavour non-buoyant plume, contributing to the persistence of high Fe concentrations both past END3 and likely farther than our most distal station.

2.4.3 Manganese oxidation and particle formation

The size fractionation of Mn differs markedly to that of Fe in the plume at Endeavour. While the plume experiences a similar exponential decrease in total concentrations moving from END1 to END5, it is the dissolved phase that is dominant over particulate across all stations (Figure 12). Dissolved Mn appears to control the distribution of the TMn pool, with pMn concentrations remaining relatively consistent (between 0.8 nM and 3.8 nM) at all of the off-axis stations (END3-5). A predominant dissolved phase is consistent with previous studies conducted across various hydrothermal systems (Massoth 1994). Differences in the size partitioning indicate variation in the processes that govern the cycling and distribution of Fe and Mn particles in the near-field plume. For example, Mn experiences much slower oxidation kinetics compared to Fe (Cowen 1992; Cowen et al. 1990; Davies and Morgan 1989). As such, the precipitation of Mn oxides is likely to occur at stations farther from the main vent field.

The oxidation of Mn can occur both biotically, through microbial mediated oxidation, and abiotically, through autocatalytic Mn-oxide formation. It is likely that both processes have an impact on Mn oxide formation, and therefore Mn distribution in the plume (Bargar et al. 2000; Lee et al. 2021; Luther 2005; Tebo et al. 2004). Microbially mediated Mn(II) oxidation will produce a Mn(IV)-oxide

(Bargar et al. 2000; Lee et al. 2021) that, in the presence of additional dissolved Mn(II) will be followed by an inorganic autocatalytic oxidation. This will cause dMn(II) adsorbed to the surface of the Mn(IV) oxide to oxidize, while reducing the Mn(IV) of the mineral to Mn(III) (Tebo et al. 2004, Learman et al. 2011). This formation of Mn oxides through a coupled biotic and abiotic oxidation process was observed in a non-buoyant plume from the 15°S East Pacific Rise during the GEOTRACES GP16 cruise (Lee et al. 2021). Lee and colleagues noted a non-buoyant plume dominated by oxidative processes (biotic and abiotic) producing Mn(III) oxide particles near-field (<80 km) followed by a greater influence of removal processes (aggregation and settling) in the far-field (>80 km).

The presence of organic material will also play a role in Mn particle aggregation. Cowen noted that that pMn oxides in a Juan de Fuca non-buoyant plume appears as metal encrusted bacteria. Due to the shape and sticky (polysaccharide) nature of these cells, aggregation efficiency is likely increased, resulting in additional pMn formation (Cowen 1992; Toner et al. 2009). It is likely that the size distribution of Mn in the Endeavour non-buoyant plume is influenced by similar processes described above. Increasing percentages of pMn moving from END1 to END5 ($p = 0.001$) suggests a plume that is actively experiencing both Mn(II) oxidation to form Mn(III) oxides in the pMn size fraction, as well as entrained organic material increasing aggregation to form additional particulate material (Figure 16).

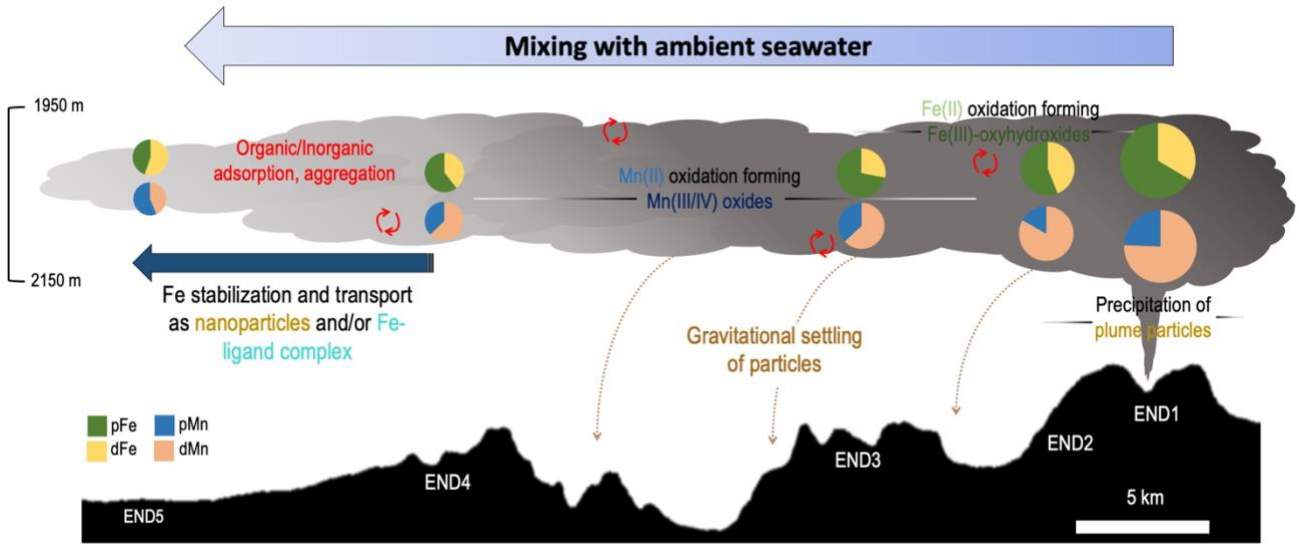

Figure 16. Illustration of the processes controlling Fe and Mn transport along the Endeavour NBP. Circles represent relative elemental concentrations at each station, with pie slices representing the average percentage of particulate and dissolved fractions.

2.4.4 Mixing and diffuse flow on Iron and Manganese plume inventories

A controlling factor on particle formation and trace metal transport in hydrothermal plumes is the mixing of vent fluid with ambient seawater during plume formation and transport. Temperature anomaly and previously measured vent fluid temperatures can be used to calculate dilution factors of the Endeavour NBP. Given the varying stages of hydrothermal plume observed through each station, average temperature anomalies were calculated for each separate station at the depth range hydrothermal plume signatures were identified (Table 7). These, along with an average vent fluid temperature of ~350 °C (Butterfield et al. 1994; Evans et al. 2023; Seyfried et al. 2003) give a dilution factor that ranges from 3400 in the axial valley to 66000 ~45 km southwest. This is comparable to the average temperature anomaly and dilution factor of 0.043 °C and 8000 calculated for a plume over MEF by Coogan 2017, and 0.06 °C and 4000 at the Endeavour Segment by Baker and Massoth 1987.

Table 7. Average temperature anomaly and calculated dilution factors.

Station	Depth range (m)	Temperature Anomaly (°C)	Dilution Factor
END1	1900-2000, 2100-2200	0.103 ± 0.033	3400 ± 1100
END2	2050-2200	0.024 ± 0.010	15000 ± 6600
END3	1950-2150	0.008 ± 0.010	46000 ± 62000
END4	1950-2150	0.008 ± 0.004	46000 ± 23000
END5	1950-2150	0.005 ± 0.002	66000 ± 29000

Dilution factors can be used to quantify the degree of change in TFe and TMn resulting from dilution and estimate how much loss may be due to precipitation or sedimentation processes. There are, however, several caveats to consider when using temperature anomalies and end member fluid temperature to estimate the fate of trace metals in the NBP. While the MEF is known for its network of high-temperature black smoker vents, the region also contains a number of diffuse flow locations (Kelley et al. 2012). As diffuse flow will add additional heat, but few particles, their influence would be observed in spots of higher temperature anomaly and a corresponding low light attenuation

anomaly. The relationship between these anomalies can provide insight into the proportion of excess heat diffuse flow adds to the plume, and therefore the impact the MEF fluxes can have on ocean chemistry (Coogan et al. 2017). The ratio of light attenuation to temperature anomaly ranges from 1.25 at END1 and progressively decreases to 0.45 at END5, suggesting either an excess of particles near-field or an excess in temperature anomaly moving off-axis (Figure 16). The high ratio proximal to vents is consistent with the ~1.25 $m^{-1}°C^{-1}$ maximum calculated by Coogan (2017) for the MEF who calculated that ~50% of the observed temperature anomaly was derived from diffuse flow (0.025°C of 0.043°C). It is therefore likely that this ~50% stands the same for stations proximal to the vent field. If this value is applied to our data, the correlation between dilution factors and changes in concentrations near-field would suggest the dominant influence on particulate metal inventories is plume mixing between these stations, with sedimentation being more important proximal to the vent field.

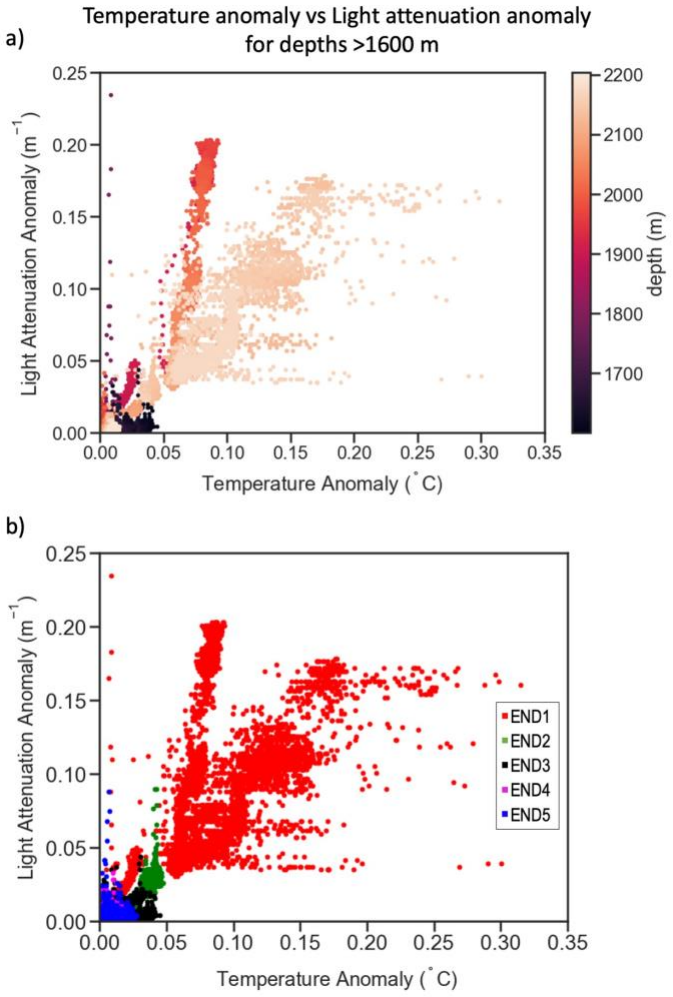

Figure 17. Plots of temperature anomaly and light attenuation anomaly for depths greater than 1600 m, color coded by a) depth and b) station. Maximums in light attenuation and temperature anomaly center at both the height of the NBP and at END1.

Trace metal concentrations were used to calculate total Fe and Mn inventories for each station using the same depth range used in the calculations of dilution factors (Table 7). Inventories are compared with dilution factors and sediment mass accumulation rates (MAR) (Table 8) for the MEF to assess the relative contribution particle fallout and plume mixing have on total trace metal inventories in the plume. Depth-integrated inventories were estimated according to the method outlined in Resing (2014), where the product of the average concentration of samples from sequential depths and the difference in depth between those samples was summed.

Due to incomplete rosette sampling bottle closures, trace metal concentrations at 2025 m and 2050 m at END4, and 2050 m and 2125 m at END5 were not obtained. Based on temperature and light attenuation anomalies, these are depths are where high concentrations of plume waters are expected. The absence of these samples will limit our ability to make quantitative inventory estimations. We are, however, reasonably confident that the trace metal distribution within the plume at these missing depths will be similar to the stations that have full plume coverage, allowing us to incorporate information from stations END4 and 5 into our discussion of trace metal inventories. To estimate concentrations for these missing depths, profiles of TFe and TMn were plotted with Δc and missing concentrations were calculated by extrapolating from Δc profiles.

Table 8. Mass accumulation rates calculated from 3 sediment traps at the MEF (Mills 2023), and depth integrated inventories for total Fe and Mn.

Mass Accumulation Rates, 2019-2020 sediment traps				
Sediment Trap	Fe (nmol m^{-2} s^{-1})		Mn (nmol m^{-2} s^{-1})	
	Avg	SD	Avg	SD
on-axis	2.132	1.120	0.024	0.015
3 km	0.019	0.006	0.004	0.001
9 km	0.060	0.041	0.035	0.020
Total metal inventories (nmol m^{-2})				
Station	TFe	dFe	TMn	dMn
END1	2.30E+07	7.70E+06	1.74E+07	1.27E+07
END2	3.01E+06	1.28E+06	2.49E+06	2.11E+06
END3	3.44E+06	1.03E+06	2.72E+06	1.99E+06
END4	2.07E+06	8.03E+05	1.65E+06	1.28E+06
END5	1.26E+06	5.51E+05	8.09E+05	3.47E+05

A major influence on trace metal loss is the mixing of the NBP with surrounding seawater. Dilution factors at stations END1 and 3 (Table 7) suggest that the NBP at END3 is ~13x diluted to that of samples at END1, while differences in depth integrated concentrations of TFe and TMn suggest that the change in concentration between these two stations is by a factor of ~7. If the ~50% of the measured temperature anomaly determined to be derived from diffuse flow (Coogan 2017) is considered, then the correlation between dilution factors and changes in concentrations near-field would suggest the dominant influence on particulate metal inventories is plume mixing between these stations. Similar comparisons can be made between dilution factors and calculated inventories. If we consider dilution as the only contributing factor to metal loss, END5 would have just ~5% of the trace metal contents of END1 (Table 7). Applying this to the calculated inventories at END1 would suggest that ~1.15 x 10^6 nmol m^{-2} Fe and ~8.72 x 10^5 nmol m^{-2} Mn should remain at END5. These values, however, are slightly smaller than calculated inventories (~1.26 x 10^6 nmol m^{-2} Fe and ~8.09 x 10^5 nmol m^{-2} Fe at END5), creating a higher Fe:heat and Mn:heat than what is expected from simple mixing.

Differences in the Fe and Mn:heat between END1 and END5 can be due to various processes. The first is differences in the influence of direct and focused flow. With diffuse flow adding additional heat, but no significant trace metal concentrations, its influence would decrease the metal:heat with as the influence of diffuse flow increases. The second is the mixing with a plume originating from a different vent field with a different metal:heat. The Mothra vent field is located ~2 km East of END2 (Figure 6), making is potential influence on the Endeavour NBP high. Significant differences exist between Mothra and MEF. While MEF is known for its up to 100 individual black smoker chimneys and high temperature vent fluids (reaching 380°C, Kelley, 2001; Glickson 2007), the Mothra vent field contains far fewer black smokers and is significantly cooler with the average heat content anomaly being lower compared to MEF (Kellogg et al., 2006; Glickson et al., 2007). Mixing between the Mothra and MEF NBP would result in a different metal:heat, and may account for differences observed in the near and far-field.

Mass accumulation rates (MAR) have been previously calculated for sediment samples collected in three sediment traps (Table 8) at varying distances from the MEF between 2019-2020 (Mills 2023). While collected a year apart, the path of NBP samples fall directly over that of the sediment traps (Figure 6), providing an opportunity to make observations between near-field NBP trace metal inventories with hydrothermal sediment mass accumulation rates. Fe MAR are highest on-axis, with 80-99% of the total determined to be hydrothermally derived which dramatically decreased to 16-

28 % just 9 km off-axis (Mills 2023). The dilution factor follows a similar pattern of being significantly higher off-axis, reflecting NBP concentrations becoming closer to background seawater levels through mixing. Particle loss, as evidenced by the sediment trap fluxes, occurs proximal to the vent field, and combined with progressive plume mixing lead to the decrease in TFe concentrations and decreasing pFe proportions moving off-axis. While significantly lower than Fe, the trends of Mn MAR in sediment traps are consistent with that of dissolved and particulate Mn in the NBP. In contrast to Fe, increases are observed in both MAR and pMn in stations further off-axis, reflecting its slower oxidation kinetics and therefore delayed particle formation (Cowen 1986). The caveat in comparing these two datasets is the roughly year-long gap between the collection of sediment trap and NBP samples. As hydrothermal systems are highly dynamic, changes in the intensity of hydrothermal activity and bottom water currents can influence both the total hydrothermal flux and sedimentation rate of the system. Therefore, changes in the MEF dynamics may account for some of the uncertainties associated with these estimations.

2.5 Conclusions

Analysis of seawater samples from a NBP at the MEF provides insight into the vertical and spatial distribution of the NBP, the range of Fe and Mn concentrations extending off-axis, and the processes that impact trace metal transport away from the ridge. Temperature and light attenuation anomalies suggest the ~200 m thick plume sits at ~1900-2100 m depth and extends at least 45 km southwest from the axial valley. Sharp decreases in these hydrographic signatures indicate a significant influence of plume mixing, with light attenuation and temperature anomalies going from a maximum 0.18 m^{-1} and 0.37°C at END1 to 0.002 m^{-1} and 0.05°C at END5. When plotted with density, physicochemical data provide additional insight into NBP distribution. Plume signals spanning multiple density surfaces at END1 suggest this station likely captured a buoyant plume that is still establishing neutrally buoyancy, while those at END2 sit on a different surface than the following stations suggesting it is a plume originating from a different vent field on the ridge.

Distributions of Fe and Mn also characterize the location of the NBP with high concentrations at END1 (24.11-68.20 nmol kg^{-1}dFe and 45.77-98.43 nmol kg^{-1} dMn) which diminish dramatically off-axis (1.23-2.98 nmol kg^{-1} dFe and 0.76-1.36 nmol kg^{-1} dMn) coincident with trends observed in hydrographic anomalies. The size partitioning of Fe and Mn between the dissolved and particulate phase provide additional insight into near and far-field processes controlling their removal and/or transport. The high percentage of pFe compared to dFe proximal to the vent field suggest a large

portion of the Fe released at vents precipitate as various sulfide minerals, with oxidation and Fe(III)-oxyhydroxide formation becoming more important as the plume evolves. Comparatively, the percentage of pMn progressively increases with distance from the vent field. As Mn experiences slower oxidation kinetics, the precipitation of Mn oxides is likely to occur in stations further from the vent field.

Depth integrated metal concentrations were used to calculate Fe and Mn inventories within the Endeavour NBP. Decreases in Fe and Mn inventories between END1 and END5 by one order of magnitude correlate well with models of rapid loss near-field from both particle formation and fallout and plume dilution, followed by their retention in the dissolved form. Ratios of dilution factors and Fe and Mn concentrations between stations END1 and 3 correlate well, suggesting that plume mixing and dilution of the NBP dominates the particulate metal inventory decreases with distance from the ridge axis. Given the dynamic nature of hydrothermal systems, our estimates may not be easily generalized to other vent fields. Changes in vent intensity, hydrothermal vent chemical composition, bottom water currents and other environmental factors including biological activity may influence sedimentation rates and total flux from the vent field and highlights the need for continuous observation and data collection.

Chapter 3: Chalcophile Element distribution in the Endeavour Non-buoyant plume

3.1 Introduction

Hydrothermal systems are an important source of trace metals to the deep ocean which factor prominently in ocean biogeochemical cycles and marine geochemical budgets (Lough et al. 2023; Resing et al. 2015; Tagliabue et al. 2022). High-temperature hydrothermal fluids result from the circulation and subsequent heating and reaction of seawater with ocean crust. Once they vent at the seafloor, these fluids rapidly mix with surrounding ambient seawater, precipitating particulate material including various metal sulfide mineral phases (Campbell et al. 1988; Von Damm 1995; German and Seyfried 2013). These vent derived particles, such as Fe-oxyhydroxides, and Mn-oxides, become a sink for other trace metals, removing them from the water column through adsorption onto the particle surfaces (Dunk and Mills 2006; German et al. 1997; German and Seyfried 2013; Lee et al. 2021). These particles are highly effective at removing trace metals from seawater and are typically most abundant close to the ridge axis. With time, these particles fall out of the plume and accumulate in the sediments below. The deposition of particles acts as an important removal mechanism of trace metals from seawater, with the rate of sedimentation controlling the loss of hydrothermal components and associated scavenged elements (German and Seyfried 2013).

Following venting, the mixture of vent fluid and surrounding seawater forms a buoyant plume which rises until reaching a state of neutral buoyancy thereafter spreading laterally with prevailing currents, away from the vent site within a non-buoyant plume (NBP). While a portion of the metals within hydrothermal fluids are lost close to the vent due to a combination of precipitation and oxidation processes forming sulfide and oxides particles, much of the trace metals present remain within the NBP, enriched relative to ambient seawater, and can be carried thousands of kilometers into the ocean interior (Baker et al. 1995; Elderfield and Schultz 1996; Fitzsimmons et al. 2014; Gonzalez-Santana et al. 2023; Hoffman et al. 2018; Tagliabue et al. 2022). The extent to which these chemical enrichments are transported away from the ridge is dependent on various physical and chemical processes that act to either remove or stabilize elements within the hydrothermal plume.

Temporal and spatial variability of dissolved and particulate trace metal concentrations in plumes will be dictated by several different physical, chemical, and in some cases, biological processes

(Dunk and Mills 2006; Gartman and Findlay 2020; González-Santana et al. 2020; D. C. Kadko et al. 1990; Thomson et al. 1992). Plume dilution due to mixing with surrounding seawater is the primary cause of decreases in concentration of dissolved constituents moving away from the MEF while trace metal scavenging onto plume particles from surrounding seawater or the dissolution of plume particles will increase trace metal concentrations in the particulate or dissolved phase respectively. Chalcophile elements are defined as elements which have an affinity for a sulfide phase. Copper (Cu), zinc (Zn), cadmium (Cd), cobalt (Co), nickel (Ni), and lead (Pb) are not only enriched in hydrothermal systems but exhibit chalcophile behaviour precipitating as various sulfide mineral phases within vent chimneys and hydrothermal plumes (Butterfield, et al. 1994; Dunk and Mills 2006; Findlay et al. 2019; German and Seyfried 2013; Sarradin et al. 2009; Schott et al. 2012).

Quantifying the chemical fluxes from hydrothermal systems is a major goal in marine geochemistry given their contribution to trace element budgets and important interactions with marine biogeochemical cycles (Cave et al. 2002; Coogan and Dosso 2012; Von Damm 1995; Edmond, et al., 1979; Elderfield and Schultz 1996; German et al., 1991). For example, various trace metal nutrients, such as Fe, Mn, and Zn, have large hydrothermal inputs and are therefore important to consider when assessing metal budgets and potential impacts on the biogeochemistry of major elements (C, S, N, P, and O) in the ocean. The net trace metal flux from hydrothermal systems will be dependent on several processes including particle formation, aggregation, precipitation, oxidation, mixing with ambient seawater, and regional current regimes. Each of these processes should be considered when assessing how and what proportion of each metal is lost from the NBP and what proportion will persist past the ridge axis. Understanding how net trace metal fluxes from hydrothermal systems into the ocean interior impact marine metal inventories and cycling requires both a multi-disciplinary approach and the use of long-term, time-series, data collection.

While significant research has been conducted on the various components of hydrothermal systems (i.e., plume, endmember, sediment geochemistry), few have directly compared near contemporaneous hydrothermal plume, sediment trap and sediment data from one region. Here, near-field processes of metal-sulfide precipitation and plume mixing are assessed in their impact on chalcophile elements including Co, Ni, Cu, Cd, and Pb. In conjunction with geochemical data collected from 3 sediment traps in 2019 we investigate interactions between the vent fluid and surrounding seawater and correlate processes impacting particle distribution in the non-buoyant plume with its underlying sediments.

3.2 Methods

Seawater samples were collected at a series of stations to characterize the impact of the Endeavour Hydrothermal Vent complex on trace element distributions in the subsurface waters of the subarctic northeast Pacific (Figure 6). Samples were collected on the *CCGS J.P Tully* between September 10-12, 2021. The sampling transect and depths were pre-determined using historical CTD data obtained from the Marine Geosciences Database. Deviations in temperature, particle concentration (determined by transmissometry) and reduction-oxidation potential (Eh) were used to identify the likely depth and location of the hydrothermal plume. We occupied five stations along a transect from the Endeavour Hydrothermal Vent complex starting at High Rise (47.968, -129.087) and proceeding ~45 km southwest. Sampling was conducted at 25 m depth intervals between the depths 1900-2200 m to capture waters influenced by hydrothermal fluids. Water samples were collected into 500 mL low density polyethylene (LDPE) bottles, which were pre-cleaned according to GEOTRACES protocols (https://www.geotraces.org/methods-cookbook/). The full methodology is outlined in Chapter 2: *Iron and Manganese distribution in the Endeavour Non-buoyant Plume.*

3.2.1 Analytical Methods

Reagent preparation and procedures to extract and analyze trace metals from seawater samples are outlined in Chapter 2: *Iron and Manganese distribution in the Endeavour Non-buoyant Plume.*

3.3 Results

3.3.1 Chalcophile Elements – Copper, Zinc, Cadmium, Lead, Nickel, Cobalt

Dissolved concentrations of Zn (dZn) at each station are elevated compared to background Pacific seawater concentrations ranging from 24 nM proximal to the vent field (END1) to 0.01 nM 45 km southwest of the axial valley (END5). Dissolved Cu (dCu) concentrations are depleted or close to background concentrations ranging from 1.1 nM to 4.0 nM (Figure 18). Despite these differences, both dZn and dCu show heterogeneity with depth at the on-axis (END1) station. As Cu and Zn precipitate quickly with the formation of sulfide minerals in the buoyant and early non-buoyant plume, this near-field variation is likely due to a combination of chemical (precipitation of Cu- and Zn-sulphides) and physical (mixing) processes that operate close to the vents. Concentrations at END1 range from 1.3 nM to 4.0 nM dCu and 3.7 nM to 24 nM dZn, with maximums being observed at 2150 m. Concentrations

measured 5 km to the southwest (END2) remain relatively uniform through all measured depths, with an average of 2.5 nM dCu and 11 dZn. A high value of 3.3 nM dCu is observed at 1925 m, and 17 nM dZn at 2000 m. Concentrations of dCu and dZn increase slightly at END3. A presumed plume signal is observed in dCu, with an elevation in concentration to 3.3 nM between 1950 – 2050 m, a similar depth to plume signals seen in dFe, dMn, and hydrographic anomalies (Chapter 2, Figure 9). This signal is not observed in dZn, with concentrations being between 10.24 nM and 15.69 nM through all measured depths.

Similar to the previous station, END4 shows elevated concentrations (average 2.7 nM) of dCu through 1950 – 2100 m. The larger depth range of the observed plume signal compared to END3 is likely a reflection of plume dispersion, and the decrease in concentration a reflection of plume mixing with seawater. dZn concentrations at END4 are similar to those observed at END3, with an average of 14 nM. A high of 21 nM occurs at 1950 m. dCu ~45 km off-axis (END5) is characterized by uniformly low concentrations through all measured depths, ranging from 1.7 nM to 2.3 nM dCu. The same can be said for dZn concentrations (12 nM to 19 nM), apart from 2075 m which has an elevated concentration of 24 nM.

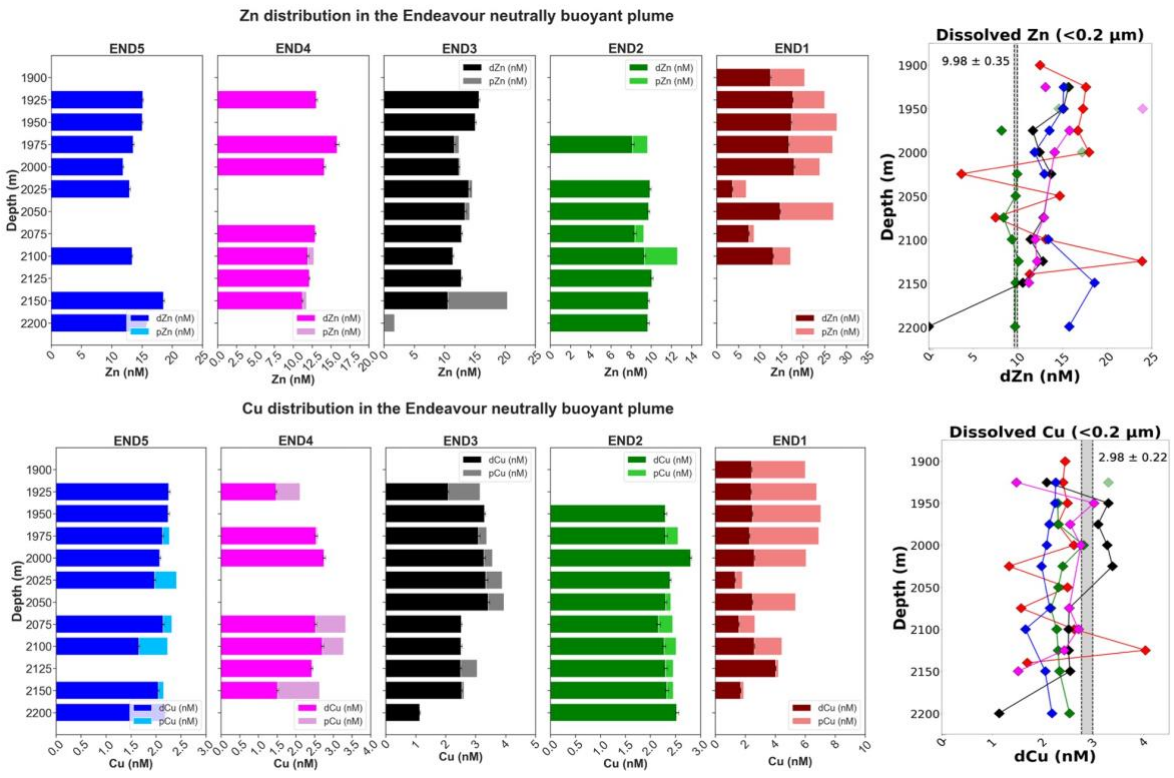

Figure 18. Zn and Cu size partitioning between dissolved (<0.2 µm) and particulate (>0.2 µm) size fractions for Zn and Cu, along with vertical profiles of dissolved Zn and Cu. Grey bars on vertical profiles indicate background Pacific seawater concentrations, obtained from Martin 1989.

Lead (Pb), cobalt (Co), Nickel (Ni), and cadmium (Cd) can be scavenged onto or incorporated into Fe-Mn-oxyhydroxides within NBPs (Feely et al. 1992; Kadko 1993; Mottl and McConachy 1990), and are each similar to or slightly enriched with respect to ambient seawater. Dissolved concentrations of Cd (dCd) and Ni (dNi) show similar bimodal distributions with slight depletions in near-axis stations (0.77 nM dCd and 7.8 nM dNi at END1) followed by an increase to at or just above (1.04 nM dCd and 11.2 nM dNi at END5) background seawater concentrations (Figure 19). A similar trend of increasing concentrations from 0.06 nM at END1 to 0.13 nM at END5 is observed in dPb profiles, with all stations being elevated compared to background seawater concentrations (Figure 19). Unlike dCd and dNi, elevated concentrations of dPb are observed at 2000 m from END2-5, matching the height of the plume observed through previously described trace metals (Chapter 2, Figure 11) and hydrographic anomalies. The distribution of dCo does not change significantly spatially or vertically through the water column, showing no significant plume signal. Average concentrations fall between 0.01 nM and 0.02 nM across all stations. An anomalously high concentration of 0.07 nM dCo is observed at 1950 m at END4, and 0.06 nM and 0.05 nM at 2140 m and 2025 m respectively, at END1. Similar to the trends observed in dZn and dCu, the water column profiles of each trace metal at END1 are heterogeneous. As these elements can precipitate as metal sulfides, these trends likely represent a buoyant plume and reflect precipitation and mixing factors that operate close to the vent.

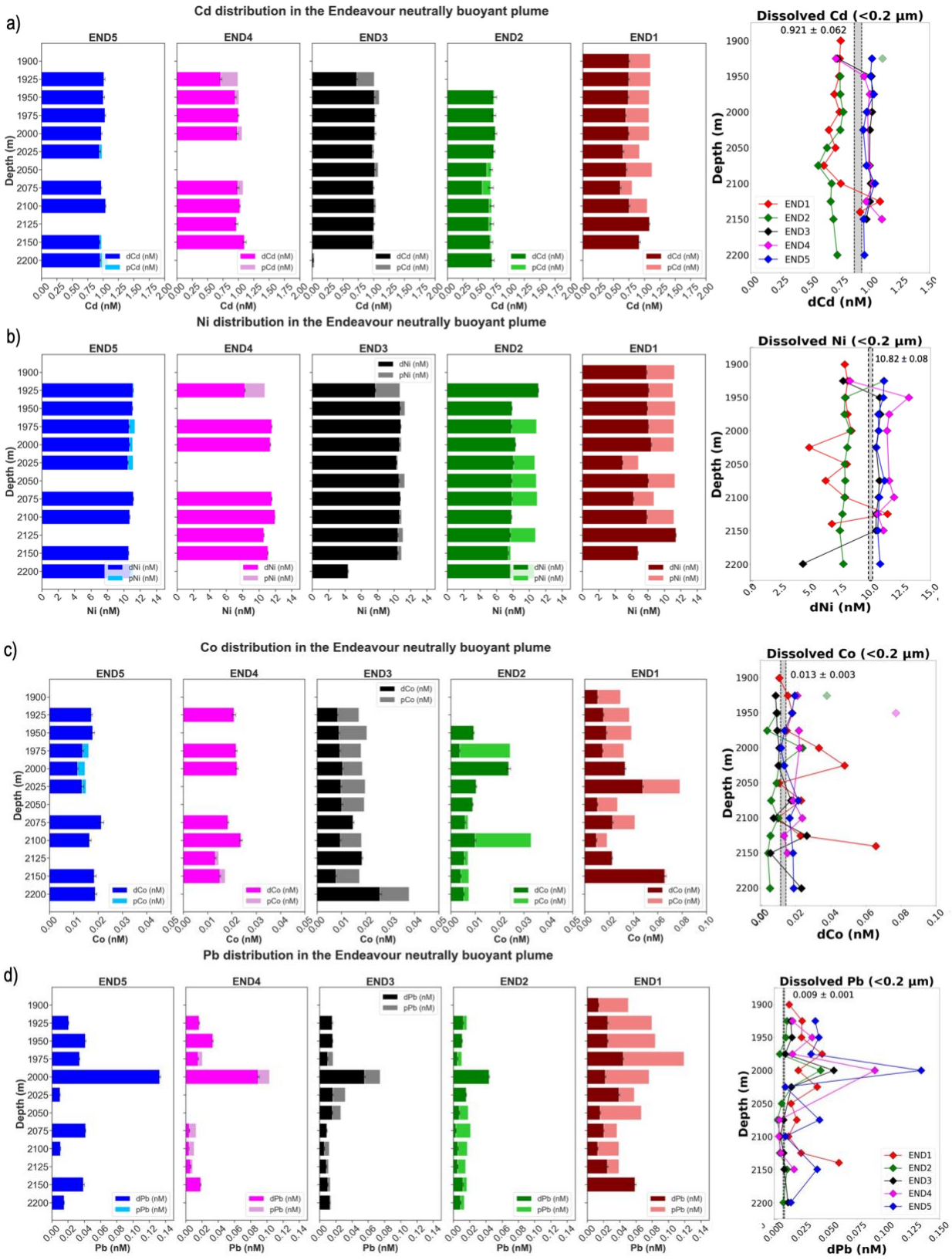

Figure 19. Size partitioning between dissolved (<0.2 µm) and particulate (>0.2 µm) size fractions, and vertical profiles of dissolved a) Cd, b) Ni, c) Co, and d) Pb. Grey bars on vertical profiles indicate background Pacific seawater concentrations, obtained from Martin 1989.

3.3.2 Trace Metal Inventories

Given the large concentrations of trace metals released by hydrothermal systems, it stands to reason they may represent an important source or sink of trace metals to the ocean. Quantifying the concentration of trace metals that are both released by hydrothermal systems and are transported from the ridge axis is an area of ongoing research. There are, however, few studies that have investigated dissolved trace metal concentrations (other than Fe and Mn) over large distances and time scales, and even fewer who have estimated chemical inventories and fluxes. Depth integrated total and dissolved trace metal inventories are presented below (Table 9).

Table 9. a) Total and b) Dissolved trace metal inventories calculated using measured depth-integrated concentrations.

Total Metal Inventory (nmol m^{-2})								
Station	**tMn**	**tFe**	**tCu**	**tZn**	**tCo**	**tCd**	**tNi**	**tPb**
END1	1.74×10^{7}	2.30×10^{7}	2.34×10^{5}	9.15×10^{5}	1.75×10^{3}	2.58×10^{5}	2.56×10^{6}	1.63×10^{4}
END2	2.49×10^{6}	3.01×10^{6}	1.27×10^{5}	3.75×10^{5}	5.91×10^{2}	1.90×10^{5}	2.62×10^{6}	4.51×10^{3}
END3	2.72×10^{6}	3.44×10^{6}	1.54×10^{5}	6.68×10^{5}	1.05×10^{3}	2.56×10^{5}	2.84×10^{6}	5.93×10^{3}
END4	1.65×10^{6}	2.07×10^{6}	1.07×10^{5}	4.39×10^{5}	6.53×10^{2}	2.32×10^{5}	2.42×10^{6}	7.63×10^{3}
END5	8.09×10^{5}	1.26×10^{6}	1.14×10^{5}	5.25×10^{5}	7.39×10^{2}	2.72×10^{5}	2.99×10^{6}	7.64×10^{3}
Dissolved Metal inventory (nmol m^{-2})								
Station	**dMn**	**dFe**	**dCu**	**dZn**	**dCo**	**dCd**	**dNi**	**dPb**
END1	1.27×10^{7}	7.70×10^{6}	5.83×10^{3}	3.61×10^{6}	5.83×10^{3}	1.90×10^{5}	1.96×10^{6}	6.59×10^{3}
END2	2.11×10^{6}	1.28×10^{6}	2.70×10^{3}	2.00×10^{6}	2.70×10^{3}	1.84×10^{5}	2.20×10^{6}	3.14×10^{3}
END3	1.99×10^{6}	1.03×10^{6}	3.39×10^{3}	3.18×10^{6}	3.39×10^{3}	2.47×10^{5}	2.73×10^{6}	4.21×10^{3}
END4	1.28×10^{6}	8.03×10^{5}	5.87×10^{3}	2.65×10^{6}	3.94×10^{3}	2.20×10^{5}	2.57×10^{6}	6.76×10^{3}
END5	3.47×10^{5}	5.51×10^{5}	4.63×10^{3}	2.19×10^{6}	4.63×10^{3}	2.70×10^{5}	2.97×10^{6}	1.03×10^{4}

Spatial trends of total and dissolved trace metal inventories match that of measured concentrations with higher proportions of the near field (END1), and steadily decreasing with distance from the axial valley within uncertainty. Of the chalcophile elements, TCo experiences the greates loss between END1 (1.75×10^{3}) and END5 (7.39×10^{2}), while TCd and TNi see the least amount of change between stations. Inventories of dNi, and dCd show increases between END1 (1.96×10^{6} dNi, 1.90×10^{5} dCd) and END5 (2.97×10^{6} dNi, 2.97×10^{6}, 2.70×10^{5} dCd). dCo, dZn, and dCu each show slight decreases in their dissolved inventories.

3.4 Discussion

The primary determinant of the chemistry of hydrothermal plumes are processes that control particle formation and sinking. The composition and fate of these particles are dependent on numerous factors including the initial hydrothermal fluid and surrounding seawater chemistry, fluid flux, and any chemical and/or biological processes that transfer these elements between the dissolved and particulate phases (German and Seyfried 2013). Among the processes that control particle formation is the precipitation of metal-sulfide mineral phases resulting from the mixing of hydrothermal fluid and ambient seawater. Chalcophile elements (Cu, Cd, Zn, Co, Pb), a major component of hydrothermal fluids, are often incorporated into these sulfide minerals (Dunk and Mills 2006; Findlay et al. 2015; German and Seyfried 2013; Rudnicki and Elderfield 1993). The distribution of chalcophile elements within non-buoyant plume samples suggest that the majority of these trace metals precipitate relatively early, with the percent of total measured concentrations being in the dissolved phase increasing from ~55-77% proximal to the main vent field to ~93-99% at stations with increasing distance from the hydrothermal field.

3.4.1 Chalcophile Element Distribution

3.4.1.1 Copper and Zinc

Cu and Zn are hydrothermally derived elements known to precipitate almost instantaneously within the early buoyant plume or chimney itself as various metal-sulfide phases (Feely et al. 1992; Metz and Trefry 2000; Rudnicki and Elderfield 1993). Early studies of plume particles from the Endeavour segment identified Fe, Cu, and Zn rich particles with pyrite (FeS_2), chalcopyrite ($CuFeS_2$) and sphalerite (ZnS) being dominant mineral phases present (Dymond and Roth 1988; Feely 1987). In addition, they are often associated with Fe-oxyhydroxide phases through co-precipitation and sorption reactions during oxyhydroxide formation (Dunk and Mills 2006). Once formed, these particles are preferentially removed from the plume due to settling and/or are transferred to the dissolved phase through oxidative dissolution (Cullen and Coogan 2017; Edmonds and German 2004). Due to its proximity to the MEF, it is likely that these processes of precipitation, co-precipitation, and sorption will be observed at or before END1, which is located above the MEF in the positively buoyant phase of the plume. Linear correlations between pCu and pZn (r^2=0.77) at END1 (Figure 21) suggest that the two metals may be removed at similar rates, through mineral precipitation, or experience similar degrees of mixing between background seawater and vent fluid.

Despite their similar distribution in the early phase of plume evolution, dCu and dZn display differing behaviours within the NBP, with dCu being depleted and dZn enriched with respect to seawater (Figure 18). Slightly elevated dZn concentrations have been previously observed in a plume at the Tans-Atlantic Geotraverse (TAG) over the Mid-Atlantic Ridge (MAR) by Conway and John (2014). In this instance, Conway and John (2014) identified enrichments in dZn coincident with trends toward isotopically light δ^{66}Zn of the dZn. As the formation of ZnS typically drives δ^{66}Zn towards enrichment in the heavier isotope, it was suggested that this elevated dZn was comprised of a large nanoparticulate Zn-sulfide phase that can pass through filters that precipitated from the isotopically light vent fluids and was subsequently transported within the NBP (Conway and John 2014). Similar enrichments of dZn in a nanoparticulate phase were identified in black smoker fluids from the Niua South vent field in the Lau Basin, South Pacific Ocean (Gartman et al. 2019), as well as in the EPR (Lough 2019), however the long-range transport of dZn within the NBP was discounted due to particle fallout.

The elevation of dZn compared to background seawater may also be the result of the oxidative dissolution of Zn-sulfides (German et al., 1991; Rudnicki and Elderfield 1993; Trocine and Trefry 1988). Mineralogic studies conducted at vents along the Endeavour Segment noted black smoker particles that are highly enriched in Fe, S, Ca, Cu, and Zn, as well as a high proportion of Zn-bearing sulfides such as sphalerite (Butterfield, et al. 1994; Feely et al 1987). High concentrations of dZn, along with a high dZn:H_2S ratio of vent fluid, indicates that a large portion of Zn emitted from hydrothermal vents will react to form ZnS, contributing to both the possible formation of nanoparticulate ZnS and the eventual transport and oxidative dissolution of larger ZnS particles to release dZn into the NBP.

While Zn and Cu experience similar processes of precipitation proximal to the vent site, the depletion of dCu with respect to background seawater suggests there is some variation in the processes that control their fate off-axis. Like Zn, Cu within hydrothermal fluids is rapidly removed forming Cu-rich precipitates with chalcopyrite ($CuFeS_2$) and isocubanite ($CuFe_2S_3$) being major mineral phases identified at the MEF (Dymond and Roth 1988; Feely 1987; Feely et al. 1994). Minimums of dCu due to sulfide precipitation and sedimentation is a likely explanation for the near-field station, END1, given the higher proportion of particulate phase present (Figure 18). Increases observed in subsequent stations bringing dCu concentrations close to background seawater may be due to a number of factors. The formation and dissolution of Cu-sulfides near the vent can release Cu from these particulates into the dissolved form (Jacquot and Moffett 2015). This would increase concentrations further off-axis and

may be responsible for the increase observed at END3. Another explanation for the slight increase in dCu is due to the mixing of a dCu depleted NBP with surrounding seawater, bringing concentrations closer to background concentrations.

Another interesting trend is the apparent decrease in dCu between END3 and 5. Jacquot and Moffett (2015) observed similar depletions in dCu concentrations at the TAG vent field station USGT11-16 compared to seawater samples both above and below the plume. In this instance, trends were attributed to intense scavenging of dCu, by Fe-oxyhydroxides given the high concentration of oxyhydroxides observed in the plume, as well as a smaller influence of organic ligand complexation (Jaquot and Moffett 2015, Lee 2018, German 1991). Similarly, Trefrey (1985) found that suspended particles in plumes along the Mid-Atlantic Ridge (MAR) were primarily composed of Cu- and Zn-enriched Fe-oxyhydroxides. While it is difficult to determine the specific process impacting dCu distribution in the Endeavour NBP, given the dynamic nature of hydrothermal systems, it is likely that a combination of these factors are at play.

3.4.1.2 Cadmium, lead, nickel, and cobalt

Due to their association with metal-sulfide phases, the distribution of Co, Ni, Cd and Pb in hydrothermal plumes is typically controlled by processes that impact the fate of Fe, Mn, Cu, and Zn. Co-precipitation, sorption, scavenging, and mixing will influence the distribution of these elements, acting to remove or retain them from the buoyant or non-buoyant plume. Both dCd and dNi show two different or bimodal distributions reflecting some of these processes, with slight depletions proximal to the vent field and enrichments further off-axis (Figure 19). Higher proportions of the particulate phase in near field stations can be explained by the precipitation of sulfide phases proximal to the vent, a process which is likely controlling their removal near-field. As the NBP travels far-field, continual mixing with seawater adds dCd and dNi, increasing concentrations to background seawater concentrations.

Elevated TPb concentrations across all stations may be explained, in part, by both its incorporation into metal sulfide and oxyhydroxide phases and scavenging by Mn- and Fe-oxyhydroxide particles (Fang and Wang 2021, German 1991, Hrisheva and Scott 2007, Lee 2021, Bargar 1997). Elevated concentrations of pPb have been previously observed in plumes over Middle Valley on the JdFR (Zheng et al. 2017), the EPR (Lee et al. 2021), and TAG on the MAR (Trocine and Trefry 1988).

In each case, high concentrations were attributed to Pb scavenging by plume particles. The influence of scavenging on Pb at MEF is further evidenced by Pb isotopes, with Coogan (2017) finding sediment trap and push core samples collected near the MEF (<1 km) to have a Pb-isotopic composition most similar to the massive sulfides typical of Endeavour field basalts, while those collected >1 km from the vents have higher Pb-isotopic ratios suggesting greater scavenging of seawater Pb (Coogan et al 2017).

The spatial distribution of dCo shows little variation, being close to background seawater concentrations (~0.013 +/- 0.003, Martin et al. 1989) at all stations. Unlike pCd and pCu, pCo does not show linear correlations with pZn, and while Co is known to precipitate with Cu (Metz and Trefry 2000; Seyfried et al. 2003), it too shows scatter at stations proximal to the vent field. Lack of correlations with Fe, along with near background concentrations suggest the majority of Co present in vent fluids is rapidly precipitated and lost to sedimentation.

3.4.2 Metal sulfide precipitation and dissolution

Due to their association with Fe-sulfides, chalcophile elements will typically exhibit negative, non-conservative concavity when plotted against dFe, a reflection of their rapid removal from the plume due to precipitation, settling, and oxidative dissolution (Feely et al. 1992; German et al. 1991; Metz and Trefry 2000; Rudnicki and Elderfield 1993). While scatter is observed in dissolved chalcophile element/Fe correlations, likely due to removal within the buoyant plume, there are linear relationships in near-field (END1) particulate Pb ($r^2 = 0.92$), Cu ($r^2 = 0.98$), Cd ($r^2 = 0.83$), and Zn ($r^2 = 0.74$) and pFe (Figure 20). Associations of these trace metals suggest a conservative behaviour relative to Fe, with similar removal pathways including sulfide precipitation and plume mixing.

Previous studies have identified an abundance of the Cu and Zn bearing sulfides chalcopyrite ($CuFeS_2$) and sphalerite ((Zn, Fe)S) in black smoker particles and sediments proximal to the MEF (Feely 1987, Dymond and Roth 1988, Hrischeva and Scott 2007). This, combined with near-field correlations of pZn and pCu with pFe, would indicate that the precipitation of these two mineral phases is an important control on the concentration of particulate Fe, Cu and Zn. With similar correlations to pFe, pCd and pPb distributions are likely influenced by their association with these mineral precipitation processes in the near field as well. Sphalerite has been shown to incorporate Cd and Pb into its mineral structure (Hsu-Kim 2008, Klevenz 2011, Lough 2019), making its precipitation a possible controlling factor in pCd and pPb concentrations. Correlations of pZn with pCd ($r^2 = 0.91$) and

pPb (r^2 = 0.80) at END1 provides evidence that this is the case (Figure 20). Given these precipitation processes are characteristic of early plume mixing, correlations are only seen at END1 (within the buoyant or early non-buoyant plume), while no correlations exist in the dissolved fraction.

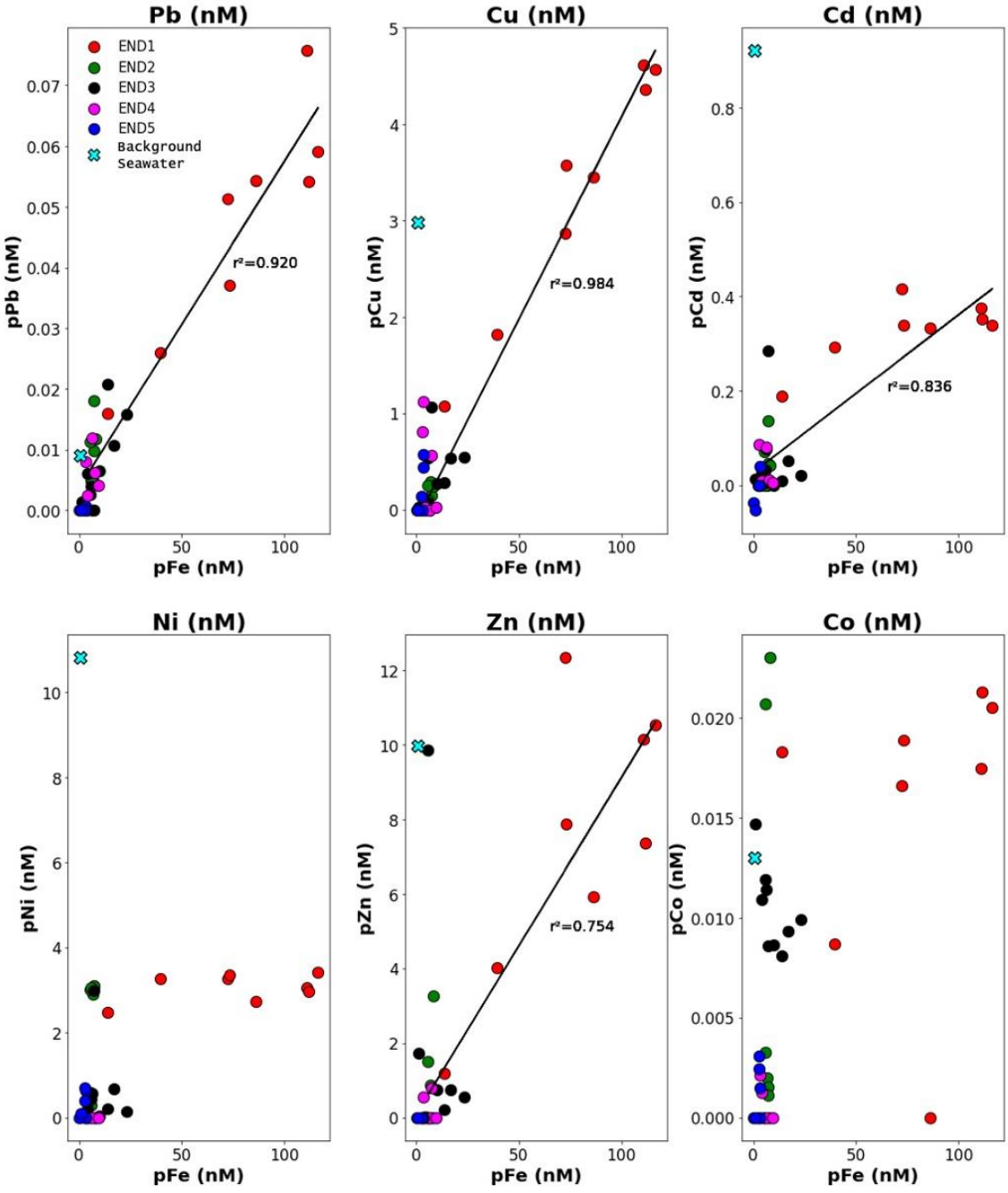

Figure 20. The concentration of pFe relative to particulate fraction of chalcophile elements. All trends are linear for END1 except pNi/pFe and pCo/pFe.

Element/Fe ratios (Figure 22) can provide additional insight into the behaviour of chalcophile elements as the NBP evolves. The dissolved element/Fe for each of the chalcophile elements exhibit similar behaviour – a low ratio proximal to the vent, followed by a progressive increase moving off-axis each approaching typical background seawater values (Martin et al. 1989; Zheng et al. 2017). This suggests that, despite the subtle differences in distribution and behaviour, the large-scale processes impacting their fate in the NBP are similar. These spatial trends in chalcophile element/Fe may reflect several processes including a decrease in dFe or increase in dissolved chalcophile element concentrations.

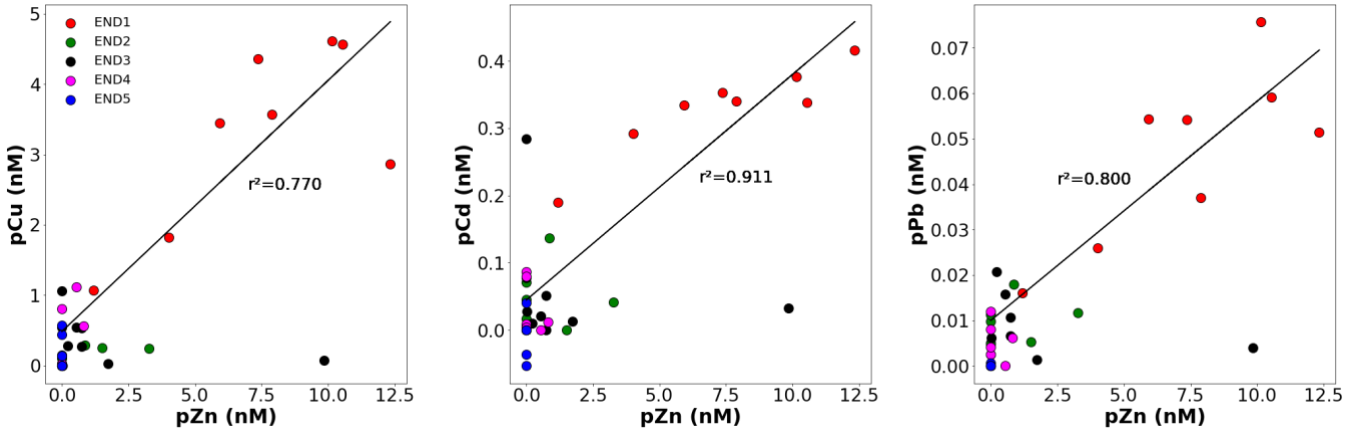

Figure 21. The concentration of pZn relative to particulate Cu, Cd, and Pb. Linear correlations are observed for each.

Given the high amount of metal-bearing sulfide precipitation experienced at END1, as well as chalcophile affinity for adsorption onto Fe-oxyhydroxides and Mn-oxide particles, the increase in element/Fe ratios may be due to either the early sedimentation or oxidative dissolution of these sulfide and oxyhydroxide particles. These hypotheses are consistent with high concentrations of sulfides within sediments of the MEF, rapid drops in the hydrothermal component of Cd/Fe and Cu/Fe of sediments within 500 m of the vents (Coogan 2017), and observed increases in dissolved fraction of Ni, Cd, and Pb.

Should increases in dissolved chalcophile element concentrations be the primary influence on dissolved element/Fe trends, dFe concentrations would need to remain relatively constant through all stations, likely through more stable forms of Fe. This is not the case. While stabilized forms of dFe (nanoparticulate or ligand bound) have been identified in NBP far from vent sites (Bennett et al. 2008; Fitzsimmons et al. 2015; Gartman and Findlay 2020; Hawkes et al. 2013; Tagliabue et al. 2022) it is unlikely that the dFe observed in these samples have been fully stabilized given their proximity to vents

(~45 km) compared to those of these studies (thousands of km). Removal of Fe from the NBP is likely taking place across all of the stations, and can attributed to several processes including sedimentation, dissolution, and progressive mixing with surrounding seawater. It is likely that each of these processes are influencing trace metal distribution and flux from the vent field.

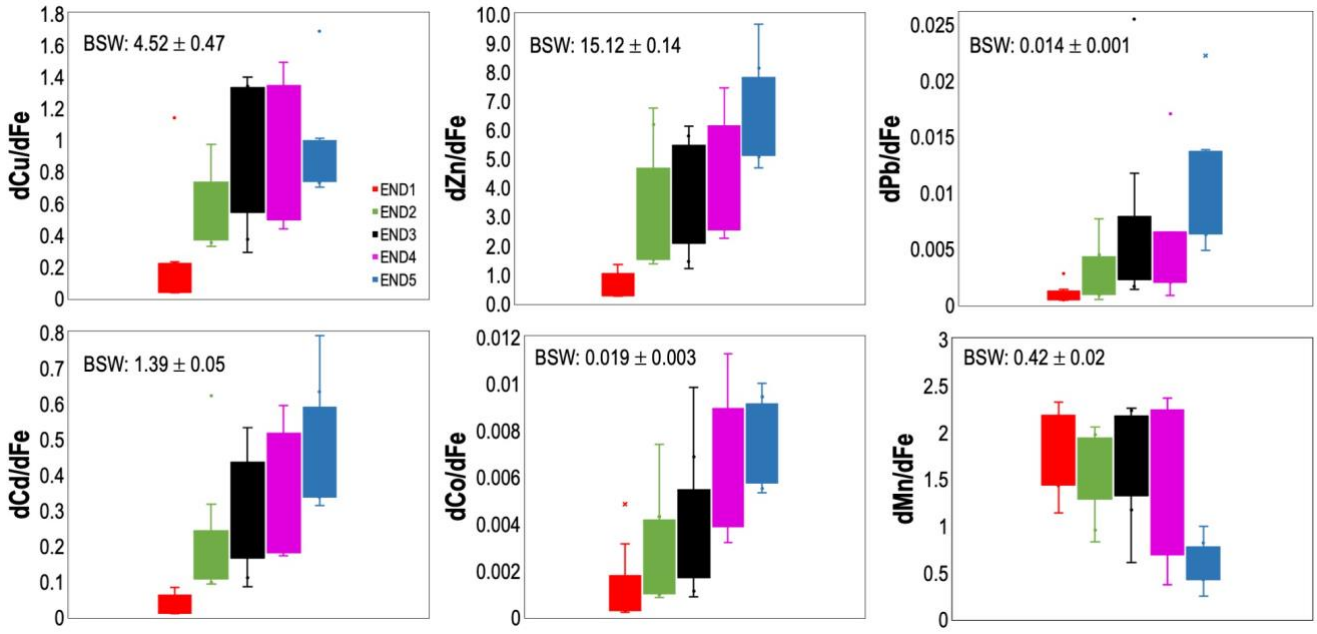

Figure 22. Dissolved chalcophile element/Fe ratios for the height of the NBP (1950-2150) for each station. BSW values are background seawater ratios, values obtained from Martin 1989. Top and bottom ends of boxes represent the upper and lower quartiles, while the box covers the area where 50% of data is found. Whiskers represent minimum and maximums of data. Dots represent outliers in the data.

3.4.3 Comparing non-buoyant plume and sediment geochemistry

The relative proximity of the MEF to major research centres, in part, explains why the geochemistry of black smoker particles and sediments have been extensively studied. The region, therefore, provides the opportunity to make on and off-axis trace metal observations and can be used to further investigate the processes that will impact metal fate. The spatial distribution of chalcophile elements, the high proportion of the dissolved phase and lack of particulate phase in the NBP indicates the bulk of these processes likely occur before or during NBP emplacement early on in the evolution of the plume.

The geochemistry and mass accumulation rates (MAR) for hydrothermal sediments collected from sediment traps proximal to the MEF in the axial valley (on-axis) and 9 km southwest (off-axis) in 2020 (Mills 2023) provide further context to the trends in near-field chalcophile element distribution in

the NBP. High MAR of Zn (18.8 μmol m^{-2} day^{-1}) and Cu (9.48 μmol m^{-2} day^{-1}) in on-axis sediment traps were attributed to the precipitation and fast fallout of chalcopyrite and sphalerite proximal to the vent field. This was followed by a large decrease 9 km off-axis (0.072 μmol m^{-2} day^{-1} Zn and 0.069 μmol m^{-2} day^{-1} Cu) due to the progressive sedimentation of particles and mixing with ambient seawater (Mills 2023). Trends in the MAR observed in this study correlate well with NBP chemistry, with the high proportion of Zn and Cu-sulfide minerals in sediments explaining the lack of particulate material observed in the plume.

These observations are consistent with previous studies by Feely (1987) on black smoker particles from a buoyant plume at the Endeavour Segment, and Dymond and Roth (1988) on plume particles collected 2 km northeast of the MEF that identified large proportions of sulfide minerals including chalcopyrite, pyrite, and sphalerite, as well as less abundant sulfide and oxide phases. Observations made by Hrischeva and Scott (2007) on the geochemistry and mineralogy of near-vent sediments (35 and 200 m from vent) and ridge flank sediments (~3 km from the vent field) identified high proportions of Fe, Cu, Zn, Pb, As, Mo, and As in near-field sediments followed by a progressive decrease in these elemental concentrations with lateral dispersal of the NBP. This trend is consistent with settling flux estimates made by Dymond and Roth (1988), which show a high particle flux enriched in Fe and Cu proximal to the MEF. Furthermore, Coogan (2017) analyzed the geochemistry of push cores at MEF finding that the composition of sediments changes systematically with distance from the vent fields with Fe, Cu, and S enriched sediments near-field followed by a rapid decrease with distance due to the rapid sedimentation of sulfide minerals.

Additionally, the distribution of sulfides in black smoker particles and sediments both on and off-axis from these studies reflect processes of rapid aggregation and settling from the plume and indicate that the majority of sulfide grains will settle proximal to the vent field (Dymond and Roth 1988; Feely et al. 1992; Hrischeva and Scott 2007). The early formation and sedimentation of Cu, Zn, Cd, and Co-bearing sulfides can be used to explain the low proportion of particulate material observed in our NBP seawater samples as well as the near background level concentrations. Subtle differences in the distribution of these chalcophile elements in the far-field NBP will therefore reflect chemical and/or biological processes more specific to each element.

3.5 Conclusions

Distributions of chalcophile elements in the NBP suggest a high proportion of metal sulfide precipitation and sedimentation proximal to the MEF. The size partitioning between particulate and dissolved fractions show similarities across all chalcophile elements with the highest proportion of the particulate phase being observed proximal to the MEF (END1) and the dissolved phase dominating all subsequent stations. Subtle differences exist in the spatial distributions of dissolved element concentrations. dZn is slightly elevated in concentration compared to background seawater, likely owing to the oxidative dissolution of Zn-sulfides such as sphalerite releasing Zn into the dissolved form. Concentrations of dCu are slightly depleted in far-field stations due to possible scavenging by Fe-oxyhydroxide particles in the NBP. Both dNi and dCd show two different or bimodal distributions, with depletions in the near-field (END1-2) followed by increases to near or just above background concentrations in following stations. The incorporation of these elements into various metal-sulfide phases can help explain the depletion near the MEF, while continual mixing with seawater will add dNi and dCd back into the plume, replenishing concentrations in the NBP. Similar to dZn, dPb shows elevated concentrations at all stations, explained by its incorporation into metal sulfide phases and scavenging by metal-sulfide and oxyhydroxide phases followed by remobilization, while dCo shows very little variation.

General trends of increasing dissolved element/Fe ratios moving off axis do not differ significantly amongst chalcophile elements, suggesting that despite small scale differences in their distribution, the large-scale processes impacting their fate are similar. With the high proportion of metal-sulfide precipitation proximal to the MEF, dissolved element/Fe ratios likely reflect a combination of early sulfide sedimentation, oxidative dissolution, and plume mixing with surrounding seawater. Linear correlations of pFe with pPb, pCu, pCd, and pZn at END1 support models of sulfide precipitation, with Fe playing a large role in chalcophile element distribution, while correlations of pZn with pCd, pCu, and pPb suggest the incorporation of these trace metals into various metal-sulfide mineral structures such as sphalerite.

The distributions of chalcophile elements for the Endeavour NBP match well with previous studies of hydrothermal sediments in the region. High mass accumulation rates of Zn and Cu on-axis, followed by an exponential decrease just 9 km off-axis observed by Mills (2023) helps explain the lack of particulate phase measured in off-axis stations (END3-5). In addition, observations of chalcopyrite,

pyrite, and sphalerite within black smoker particles and sediments within ~3 km of the vent field would confirm the important role precipitation and sedimentation processes play in controlling near-field chalcophile element distributions.

Chapter 4: Conclusions

The investigation into the trace metal chemistry of the Endeavour non-buoyant plume provides insights into the processes that affect trace metal retention and loss within hydrothermal plumes as well as what drives variation in plume chemistry with distance from the main axial valley. While hydrothermal systems have been studied in depth, from sediment geochemistry (Dunk and Mills 2006; German et al. 1997; Hrischeva and Scott 2007) or vent fluid chemistry (Butterfield et al. 1994; Evans et al., 2023; Seyfried et al. 2003), few have provided a comprehensive chemical characterization of NBP's or for positively buoyant plumes early in their chemical evolution. The collection of buoyant and non-buoyant plume samples starting at the MEF and extending ~45 km southwest add to the growing database of hydrothermal plume data and will help towards better understanding the role hydrothermal systems play in trace metal sources and sinks, and what processes control their chemistry on and off-axis.

The spatial distribution of the Endeavour hydrothermal plume can be described as a ~200 m thick plume sitting at ~1900 m – 2100 m depth, extending at least 45 km southwest from the main axial valley. Physicochemical characteristics including temperature and light attenuation anomaly, dissolved oxygen, density, and salinity, capture a hydrothermal plume at two stages. Near-field, at END1, two particle rich layers, along with sharp increases in O_2 at the top of the plume followed by steady levels down to its lower limit. These suggest a buoyant plume phase experiencing the entrainment and mixing of oxygen rich bottom water with background seawater. The mixing experienced in positively buoyant plumes is an important control on particle formation, promoting mineral precipitation and Fe oxidation. The differences in dissolved and particulate trace metal separation between Fe and Mn highlight differences in the processes that govern their distribution in the near field. The size partitioning of Fe at END1 fit well with a buoyant plume model, with higher proportions of the particulate phase near-field being the result of the precipitation of various Fe-sulfide phases including pyrite, chalcopyrite, and sphalerite. The size partitioning of Mn differs from that of Fe, with increasing proportions of the particulate phase moving away from the MEF. With slower oxidation kinetics driving the precipitation of Mn-oxides to occur further off-axis, this is to be expected. Moving away from the MEF (END3-5), a more established non-buoyant plume is captured with hydrographic anomalies and Fe and Mn concentrations decreasing with distance due to a combination of plume mixing and particle settling.

Noticeable differences in hydrographic and chemical anomalies, as well as the height of these anomalies in the water column exist between END2 and stations following. A plume core identified at ($27.685\sigma_\theta$ - $27.650\sigma_\theta$) compared to the $27.680\sigma_\theta$ plume core identified at following stations suggests that the plume associated anomalies sampled at END2 are distinct features compared to the other stations. There are a number of potential causes for these observed differences such as the mixing of NBP's originating from different vent fields.

The mixing of vent fluid with seawater is an important control on particle formation. Dilution factors provide insight into the influence mixing with seawater has on NBP trace metal concentrations. Calculated using temperature anomaly and vent fluid temperature, dilution factors range from 3400 in the axial valley to 66000 ~45 km southwest at END5. By examining dilution factors, it is found that just ~5% of the trace metal inventory of END1 would be present at END5 should dilution be the only factor on NBP trace metal concentrations. However, when compared to measured concentrations and calculated Fe and Mn inventories, it is found that these values are lower than expected metal inventories indicating an excess of Fe and Mn in the NBP. Retention of these trace metals through various stabilization processes including the formation of nanoparticles as well as binding with organic ligands are likely causes.

Chapter 3 focuses on chalcophile element (Cu, Co, Cd, Zn, Ni, Pb) distribution, and their incorporation into metal sulfide and oxide mineral phases. When vent fluid is released at the seafloor, it mixes with the much cooler, oxidizing seawater. This results in the precipitation of a number of metal sulfide phases including pyrite, chalcopyrite and sphalerite (Baker 1995, Feely 1992). The precipitation of metal sulfides, as well as the incorporation of chalcophile elements into these mineral phases, help explain the higher proportion of the particulate phase proximal to the vent (END1). This is followed by a dominant dissolved phase in all off-axis stations. Despite this, there exist subtle differences in their spatial distributions. Dissolved Zn and Pb have slightly elevated concentrations compared to background seawater, owing to the oxidative dissolution of Zn-bearing sulfides such as sphalerite which have been shown to incorporate Pb into its structure (Lough 2019, Hsu-Kim 2008), while dCu is slightly depleted in the far-field due to possible scavenging. dNi and dCd both show similar bimodal distributions with depletions in the near field followed by increases to just above or at background seawater concentrations due to mixing processes. Linear correlations of pFe with pPb, pCu, pCd, and pZn at END1 suggest a conservative behaviour relative to Fe, with similar removal pathways including

sulfide precipitation and plume mixing. In addition, these relationships highlight the important role sulfide precipitation plays in controlling chalcophile element flux in the near field.

4.1 Future Work

There are several questions that were unable to be addressed and should therefore be the focus of future work. While there has been significant dedication to studying Fe and Mn in buoyant and NBP due to both their long-range transport in NBP's and impact on ocean biogeochemistry, there are few that have constrained the impact and transport dissolved concentrations of other hydrothermally derived transition metals including Zn, Co, Cu, and Cd have in hydrothermal systems. Additional studies that incorporate bulk buoyant and NBP plume chemistry can help add to a growing database of hydrothermal plume chemistry, providing insight into whether hydrothermal plumes act as a source or sink to these trace metals. Quantifying these trace metal fluxes also remains a key question, for NBP's in particular, where precipitation processes are less likely to play a role in trace metal concentrations.

In addition to studying a larger suite of trace metals, a higher resolution of data points is needed in the near-field. This study has shown the highly dynamic and complex nature of hydrothermal systems with just 5 stations extending 45 km southwest. Capturing hydrothermal plumes, in their entirety, is a difficult task. The majority of studies have sampled NBPs over very large distances, often in single directions. Recent studies, however, have modeled the paths of hydrothermal plumes, finding a large degree of variation in plume dispersion. Xu and German (2023), for example, have simulated the dispersion of hydrothermal plumes at the Endeavour Segment, finding that tidal forcing, topographic features, and buoyancy fluxes impact plume mixing and dispersion. In addition, comparisons of data from different years revealed significant inter-annual variability in the direction of hydrothermal plume dispersion. Studies such as these reveal the need for higher resolution data through space, capturing greater portions of the buoyant and early NBP, and time, capturing potential variability in venting intensity or dispersion direction. Due to these complexities, local and regional variabilities in plume processes should be taken into account in future calculations of trace metal fluxes.

Finally, understanding the relationship between plume and sediment chemistry is important when creating models of plume particle transport and trace metal flux. While there have been several studies focusing on either sediment geochemistry or vent fluid/plume chemistry, there are very few which integrate the two. Developing studies which collect sediment and plume samples along similar transects

and within similar timeframes can help provide insight into the short term processes that remove trace metals from hydrothermal plumes, helping to constrain the degree to which hydrothermal systems act as a source or sink from important trace metals.

Bibliography

Anderson, Robert F. 2020. “GEOTRACES: Accelerating Research on the Marine Biogeochemical Cycles of Trace Elements and Their Isotopes.” *Annual Review of Marine Science* 12: 49–85.

Baker, Edward T., Christopher R. German, and Henry Elderfield. 1995. “Hydrothermal Plumes over Spreading-Center Axes: Global Distributions and Geological Inferences.” *Geophysical Monograph Series* 91: 47–71.

Baker, Edward T., and Gary J. Massoth. 1987. “Characteristics of Hydrothermal Plumes from Two Vent Fields on the Juan de Fuca Ridge, Northeast Pacific Ocean.” *Earth and Planetary Science Letters* 85(1–3): 59–73.

Bargar, J. R., B. M. Tebo, and J. E. Villinski. 2000. “In Situ Characterization of Mn(II) Oxidation by Spores of the Marine Bacillus Sp. Strain SG-1.” *Geochimica et Cosmochimica Acta* 64(16): 2775–78.

Bennett, Sarah A. et al. 2008. “The Distribution and Stabilisation of Dissolved Fe in Deep-Sea Hydrothermal Plumes.” *Earth and Planetary Science Letters* 270(3–4): 157–67.

Bischoff, James L., and Kenneth S. Pitzer. 1985. “Phase Relations and Adiabats in Boiling Seafloor Geothermal Systems.” *Earth and Planetary Science Letters* 75(4): 327–38.

Bruland, K. W., R. Middag, and M. C. Lohan. 2013. 8 Treatise on Geochemistry: Second Edition *Controls of Trace Metals in Seawater*. 2nd ed. Elsevier Ltd. http://dx.doi.org/10.1016/B978-0-08-095975-7.00602-1.

Butterfield, D. A., R. E. McDuff, M. J. Mottl, et al. 1994. “Gradients in the Composition of Hydrothermal Fluids from the Endeavour Segment Vent Field: Phase Separation and Brine Loss.” *Journal of Geophysical Research* 99(B5): 9561–83.

Butterfield, D.A., R.E. McDuff, J. Franklin, and C.G. Wheat. 1994. “Geochemistry of Hydrothermal Vent Fluids from Middle Valley, Juan de Fuca Ridge.” *Proceedings of the Ocean Drilling Program, 139 Scientific Results* (April 2015).

Campbell, A. C. et al. 1988. “Chemistry of Hot Springs on the Mid-Atlantic Ridge.” *Nature* 335(6190): 514–19.

Cave, R. R., C. R. German, J. Thomson, and R. W. Nesbitt. 2002. “Fluxes to Sediments Underlying the Rainbow Hydrothermal Plume at 36°14’N on the Mid-Atlantic Ridge.” *Geochimica et Cosmochimica Acta* 66(11): 1905–23.

Conway, Tim M, and Seth G John. 2014. “Global Biogeochemical Cycling of Zinc and Zinc Isotopes in the North Atlantic Ocean.” *Global Biogeochemical cycles*: 1111–28.

Coogan, L. A.; Attar, A.; Mihaly, S. F.; Jeffries, M.; Pope, M. 2017. “Near-Vent Chemical Processes in a Hydrothermal Plume: Insights from an Integrated Study of the Endeavour Segment.” *Geochemistry, Geophysics, Geosystems* 116(1): 1–12. http://linkinghub.elsevier.com/retrieve/pii/S0012825216303713%5Cnhttp://doi.wiley.com/10.1029/2001JB000204%5Cnhttp://linkinghub.elsevier.com/retrieve/pii/S0012821X17301036%5Cnhttp://www.nature.com/doifinder/10.1038/nature14502%5Cnhttp://www.agu.org/pubs/c.

Coogan, Laurence A., and Stan Dosso. 2012. “An Internally Consistent, Probabilistic, Determination of Ridge-Axis Hydrothermal Fluxes from Basalt-Hosted Systems.” *Earth and Planetary Science Letters* 323–324: 92–101. http://dx.doi.org/10.1016/j.epsl.2012.01.017.

Coogan, Laurence A., William E. Seyfried, and Nicholas J. Pester. 2019. “Environmental Controls on Mid-Ocean Ridge Hydrothermal Fluxes.” *Chemical Geology* 528(September): 119285. https://doi.org/10.1016/j.chemgeo.2019.119285.

Cowen, J. P. 1992. “Morphological Study of Marine Bacterial Capsules: Implications for Marine Aggregates.” *Marine Biology* 114(1): 85–95.

Cowen, James P., Gary J. Massoth, and Richard A. Feely. 1990. “Scavenging Rates of Dissolved Manganese in a Hydrothermal Vent Plume.” *Deep Sea Research Part A, Oceanographic Research*

Papers 37(10): 1619–37.
Cullen, J. T., and L. A. Coogan. 2017. “Changes in Fe Oxidation Rate in Hydrothermal Plumes as a Potential Driver of Enhanced Hydrothermal Input to Near-Ridge Sediments During Glacial Terminations.” *Geophysical Research Letters* 44(23): 11,951-11,958.
Von Damm, K. L. 1995. “Temporal and Compositional Diversity in Seafloor Hydrothermal Fluids.” *Reviews of Geophysics* 33(2 S): 1297–1305.
Davies, Simon H.R., and James J. Morgan. 1989. “Manganese(II) Oxidation Kinetics on Metal Oxide Surfaces.” *Journal of Colloid And Interface Science* 129(1): 63–77.
Dunk, Rachel M., and Rachel A. Mills. 2006. “The Impact of Oxic Alteration on Plume-Derived Transition Metals in Ridge Flank Sediments from the East Pacific Rise.” *Marine Geology* 229(3–4): 133–57.
Dymond, Jack, and Sharon Roth. 1988. “Plume Dispersed Hydrothermal Particles: A Time-Series Record of Settling Flux from the Endeavour Ridge Using Moored Sensors.” *Geochimica et Cosmochimica Acta* 52(10): 2525–36.
Edmond, J. M., Measures,C., McDuff.R.E., Chan.L.J., Collier.R., Grant.B. 1979. “Ridge Crest Hydrothermal Activity and the Balances of the Major and Minor Elements in the Ocean: The Galapagos Data.” *Earth and Planetary Science Letters* 46: 1–18.
Edmonds, Henrietta N., and Christopher R. German. 2004. “Particle Geochemistry in the Rainbow Hydrothermal Plume, Mid-Atlantic Ridge.” *Geochimica et Cosmochimica Acta* 68(4): 759–72.
Elderfield, H., and A. Schultz. 1996. “Mid-Ocean Ridge Hydrothermal Fluxes and the Chemical Composition of the Ocean.” *Annual Review of Earth & Planetary Sciences* 24: 191–224.
Evans, Guy N., William E. Seyfried, and Chunyang Tan. 2023. “Nutrient Transition Metals in a Time Series of Hydrothermal Vent Fluids from Main Endeavour Field, Juan de Fuca Ridge, Pacific Ocean.” *Earth and Planetary Science Letters* 602: 117943. https://doi.org/10.1016/j.epsl.2022.117943.
Feely, R. A. 1987. “Composition and Dissolution of Black Smoker Particulates from Active Vents on the Juan de Fuca Ridge.” *Journal of Geophysical Research* 92(B11).
Feely, R. A., et al. 1994. “Composition and Sedimentation of Hydrothermal Plume Particles from North Cleft Segment, Juan de Fuca Ridge.” *Journal of Geophysical Research* 99(B3): 4985–5006.
Feely, Richard A et al. 1992. “Tracking the Dispersal of Hydrothermal Plumes from the Juan de Fuca Ridge Using Suspended Matter Compositions.” *Geophysical Research* 97: 3457–68.
Field, M.Paul, and Robert M Sherrell. 2000. “Dissolved and Particulate Fe in a Hydrothermal Plume at 9°45′N, East Pacific Rise:” *Geochimica et Cosmochimica Acta* 64(4): 619–28.
Findlay, Alyssa J. et al. 2019. “Iron and Sulfide Nanoparticle Formation and Transport in Nascent Hydrothermal Vent Plumes.” *Nature Communications* 10(1): 1–7. http://dx.doi.org/10.1038/s41467-019-09580-5.
Findlay, Alyssa J., Amy Gartman, Timothy J. Shaw, and George W. Luther. 2015. “Trace Metal Concentration and Partitioning in the First 1.5m of Hydrothermal Vent Plumes along the Mid-Atlantic Ridge: TAG, Snakepit, and Rainbow.” *Chemical Geology* 412: 117–31. http://dx.doi.org/10.1016/j.chemgeo.2015.07.021.
Fitzsimmons, J. et al. 2015. “Partitioning of Dissolved Iron and Iron Isotopes into Soluble and Colloidal Phases along the GA03 GEOTRACES North Atlantic Transect.” *Deep-Sea Research Part II: Topical Studies in Oceanography* 116: 130–51. http://dx.doi.org/10.1016/j.dsr2.2014.11.014.
Fitzsimmons, J., et al. 2017. “Iron Persistence in a Distal Hydrothermal Plume Supported by Dissolved-Particulate Exchange.” *Nature Geoscience* 10(3): 195–201.
Fitzsimmons, J., Boyle, E., and Jenkins, W. 2014. “Distal Transport of Dissolved Hydrothermal Iron in the Deep South Pacific Ocean.” *Proceedings of the National Academy of Sciences of the United States of America* 111(47): 16654–61.

Gartman, Amy et al. 2019. “The Role of Nanoparticles in Mediating Element Deposition and Transport at Hydrothermal Vents.” *Geochimica et Cosmochimica Acta* 261: 113–31.
Gartman, Amy, and Alyssa J. Findlay. 2020. “Impacts of Hydrothermal Plume Processes on Oceanic Metal Cycles and Transport.” *Nature Geoscience* 13(6): 396–402. http://dx.doi.org/10.1038/s41561-020-0579-0.
German, C. R. et al. 1990. “Hydrothermal Scavenging of Rare-Earth Elements in the Ocean.” *Letters to Nature* 345: 516–18.
German, R., et al. 1997. “Hydrothermal Scavenging on the Juan de Fuca Ridge: 230Thxs, 10Be, and REEs in Ridge-Flank Sediments.” *Geochimica et Cosmochimica Acta* 61(19): 4067–78.
German, R., et al. 2016. “Hydrothermal Impacts on Trace Element and Isotope Ocean Biogeochemistry.” *Philosophical Transactions of the Royal Society A: Mathematical, Physical and Engineering Sciences* 374(2081).
German, C. R., A. C. Campbell, and J. M. Edmond. 1991. “Hydrothermal Scavenging at the Mid-Atlantic Ridge: Modification of Trace Element Dissolved Fluxes.” *Earth and Planetary Science Letters* 107(1): 101–14.
German, C. R., and W. E. Seyfried. 2013. 8 Treatise on Geochemistry: Second Edition *Hydrothermal Processes*. 2nd ed. Elsevier Ltd. http://dx.doi.org/10.1016/B978-0-08-095975-7.00607-0.
Glickson, D. A., Kelley, D. S., Delaney, J. R. 2007. "Geology and hydrothermal evolution of the Mothra Field, Endeavour Segment, Juan de Fuca Ridge. *Geochemistry, Geophysics, Geosystems. 8(6).*
Gonzalez-Santana, David et al. 2021. “Variability in Iron (II) Oxidation Kinetics across Diverse Hydrothermal Sites on the Northern Mid Atlantic Ridge.” *Geochimica et Cosmochimica Acta* 297: 143–57.
González-Santana, David et al. 2020. “Processes Driving Iron and Manganese Dispersal From the TAG Hydrothermal Plume (Mid-Atlantic Ridge): Results From a GEOTRACES Process Study.” *Frontiers in Marine Science* 7(July): 1–17.
Hawkes, J. A., D. P. Connelly, M. Gledhill, and E. P. Achterberg. 2013. “The Stabilisation and Transportation of Dissolved Iron from High Temperature Hydrothermal Vent Systems.” *Earth and Planetary Science Letters* 375: 280–90. http://dx.doi.org/10.1016/j.epsl.2013.05.047.
Hoffman, Colleen L. et al. 2018. “Near-Field Iron and Carbon Chemistry of Non-Buoyant Hydrothermal Plume Particles, Southern East Pacific Rise 15°S.” *Marine Chemistry* 201(July 2017): 183–97.
Hrischeva, Elitsa, and Steven D. Scott. 2007. “Geochemistry and Morphology of Metalliferous Sediments and Oxyhydroxides from the Endeavour Segment, Juan de Fuca Ridge.” *Geochimica et Cosmochimica Acta* 71(14): 3476–97.
Hsu-Kim, H., Mullaugh, K. M., Tsang, J. J., Yucel, M., and Luther, G. W.: Formation of Zn- and Fe-sulfides near hydrothermal vents at the Eastern Lau Spreading Center: Implications for sul- fide bioavailability to chemoautotrophs, Geochem. Trans., 9, 6.
Jackson, S. L. et al. 2018. “Determination of Mn, Fe, Ni, Cu, Zn, Cd and Pb in Seawater Using Offline Extraction and Triple Quadrupole ICP-MS/MS.” *Journal of Analytical Atomic Spectrometry* 33(2): 304–13.
James, R.H, and H. Elderfield. 1996. “Dissolved and Particulate Trace Metals in Hydrothermal Plumes at the Mid-Atlantic Ridge.” *Geophysical Research Letters* 23(23): 3499–3502.
Jamieson, J. W., D. A. Clague, and M. D. Hannington. 2014. “Hydrothermal Sulfide Accumulation along the Endeavour Segment, Juan de Fuca Ridge.” *Earth and Planetary Science Letters* 395: 136–48. http://dx.doi.org/10.1016/j.epsl.2014.03.035.
Jacquot, J., Moffett, J. 2015. "Copper distribution and speciation across the International GEOTRACES Section GA03." *Deep Sea Research II*: *Topical Studies in Oceanography.* 187-207.
Jenkins, William J. 2020. “Using Excess 3He to Estimate Southern Ocean Upwelling Time Scales.”

Geophysical Research Letters 47(15): 1–10.
Johnson, H. Paul et al. 2000. “Earthquake-Induced Changes in a Hydrothermal System on the Juan de Fuca Mid-Ocean Ridge.” *Nature* 407(6801): 174–77.
Kadko, D. C. et al. 1990. “Chemical Reaction Rates and Entrainment within the Endeavour Ridge Hydrothermal Plume.” *Earth and Planetary Science Letters* 99(4): 315–35.
Kadko, David. 1993. “An Assessment of the Effect of Chemical Scavenging within Submarine Hydrothermal Plumes upon Ocean Geochemistry.” *Earth and Planetary Science Letters* 120(3–4): 361–74.
Karsten, J. L., S. R. Hammond, E. E. Davis, and R. G. Currie. 1986. “Detailed Geomorphology and Neotectonics of the Endeavour Segment, Juan de Fuca Ridge: New Results from Seabeam Swath Mapping.” *Geological Society of America Bulletin* 97(2): 213–21.
Kelley, D. S., J. R. Delaney, D. R. Yoerger. 2001. "Geology and venting characteristics of the Mothra hydrothermal field, Endeavour Segment, Juan de Fuca Ridge. *Geology*, 29, 959-962.
Kelley, Deborah S. et al. 2012. “Endeavour Segment of the Juan de Fuca Ridge, One of the Mos t Remarkable Places on Earth.” *Oceanography* 25(1): 44–61.
Kellogg, J.P., McDuff, R. E., Thomson, R. E., and Stahr, F. R. 2006. "Repeat hydrography at the Endeavour Integrated Study Site, 2004-2006. *Eos Trans. AGU, 87(52), Fall Meet.*
Klinkhammer, G., H. Elderfield, and A. Hudson. 1983. “Rare Earth Elements in Seawater near Hydrothermal Vents.” *Nature* 305(5931): 185–88.
Klunder, M. B. et al. 2012. “Dissolved Iron in the Arctic Ocean: Important Role of Hydrothermal Sources, Shelf Input and Scavenging Removal.” *Journal of Geophysical Research: Oceans* 117(4): 1–17.
Lee, J., Heller, I. M., Lam, J. P. 2018. "Size distribution of particulate trace elements in the U.S. GEOTRACES Eastern Pacific Zonal Transect (GP16). *Marine Chemistry*. 201:108-123.
Lee, J et al. 2021. “Changing Chemistry of Particulate Manganese in the Near- and Far-Field Hydrothermal Plumes from 15°S East Pacific Rise and Its Influence on Metal Scavenging.” *Geochimica et Cosmochimica Acta* 300: 95–118. https://doi.org/10.1016/j.gca.2021.02.020.
Lilley, Marvin O., David A. Butterfield, John E. Lupton, and Eric J. Olson. 2003. “Magmatic Events Can Produce Rapid Changes in Hydrothermal Vent Chemistry.” *Nature* 422(6934): 878–81.
Lough, Alastair J. M. et al. 2023. “Tracing Differences in Iron Supply to the Mid-Atlantic Ridge Valley between Hydrothermal Vent Sites: Implications for the Addition of Iron to the Deep Ocean.” *Biogeosciences* 20(2): 405–20.
Lupton, John E., and Harmon Craig. 1981. “A Major Helium-3 Source at 15°S on the East Pacific Rise.” *Science* 214(4516): 13–18.
Luther, George W. 2005. “Manganese(II) Oxidation and Mn(IV) Reduction in the Environment - Two One-Electron Transfer Steps versus a Single Two-Electron Step.” *Geomicrobiology Journal* 22(3–4): 195–203.
Mandernack, Kevin W., and Bradley M. Tebo. 1993. “Manganese Scavenging and Oxidation at Hydrothermal Vents and in Vent Plumes.” *Geochimica et Cosmochimica Acta* 57(16): 3907–23.
Martin, John H., R. Michael Gordon, Steve Fitzwater, and William W. Broenkow. 1989. “Vertex: Phytoplankton/Iron Studies in the Gulf of Alaska.” *Deep Sea Research Part A, Oceanographic Research Papers* 36(5): 649–80.
Massoth, G. J. 1994. “Temporal and Spatial Variability of Hydrothermal Manganese and Iron at Cleft Segment, Juan de Fuca Ridge.” *Journal of Geophysical Research* 99(B3): 4905–23.
Measures, Christopher I., William M. Landing, Matthew T. Brown, and Clifton S. Buck. 2008. “A Commercially Available Rosette System for Trace Metal-Clean Sampling.” *Limnology and Oceanography: Methods* 6(9): 384–94.
Meskhidze, Nicholas et al. 2019. “Perspective on Identifying and Characterizing the Processes Controlling Iron Speciation and Residence Time at the Atmosphere-Ocean Interface.” *Marine*

Chemistry 217(October): 103704. https://doi.org/10.1016/j.marchem.2019.103704.
Metz, Simone, and J. H. Trefry. 2000. "Chemical and Mineralogical Influences on Concentrations of Trace Metals in Hydrothermal Fluids." *Geochemica et Cosmochimica* 64(13): 2267–79.
Millero, Frank J. 1995. "Thermodynamics of the Carbon Dioxide System in the Oceans." *Geochimica et Cosmochimica Acta* 59(4): 661–77.
Millero, Frank J., Sara Sotolongo, and Miguel Izaguirre. 1987. "The Oxidation Kinetics of Fe(II) in Seawater." *Geochimica et Cosmochimica Acta* 51(4): 793–801.
Moore, C. M. et al. 2013. "Processes and Patterns of Oceanic Nutrient Limitation." *Nature Geoscience* 6(9): 701–10.
Morel, F. M.M., and N. M. Price. 2003. "The Biogeochemical Cycles of Trace Metals in the Oceans." *Science* 300(5621): 944–47.
Mottl, Michael J., and Timothy F. McConachy. 1990. "Chemical Processes in Buoyant Hydrothermal Plumes on the East Pacific Rise near 21°N." *Geochimica et Cosmochimica Acta* 54(7): 1911–27.
Resing, Joseph A. et al. 2015. "Basin-Scale Transport of Hydrothermal Dissolved Metals across the South Pacific Ocean." *Nature* 523(7559): 200–203.
Riddihough, Robin P. 1978. "The Juan De Fuca Plate." *Eos, Transactions American Geophysical Union* 59(9): 836–42.
Rudnicki, M. D., and H. Elderfield. 1993. "A Chemical Model of the Buoyant and Non-buoyant Plume above the TAG Vent Field, 26 Degrees N, Mid-Atlantic Ridge." *Geochimica et Cosmochimica Acta* 57(13): 2939–57.
Sands, C. M., D. P. Connelly, P. J. Statham, and C. R. German. 2012. "Size Fractionation of Trace Metals in the Edmond Hydrothermal Plume, Central Indian Ocean." *Earth and Planetary Science Letters* 319–320: 15–22. http://dx.doi.org/10.1016/j.epsl.2011.12.031.
Sarradin, Pierre Marie et al. 2009. "Speciation of Dissolved Copper within an Active Hydrothermal Edifice on the Lucky Strike Vent Field (MAR, 37°N)." *Science of the Total Environment* 407(2): 869–78. http://dx.doi.org/10.1016/j.scitotenv.2008.09.056.
Schott, Jacques et al. 2012. "Formation, Growth and Transformation of Leached Layers during Silicate Minerals Dissolution: The Example of Wollastonite." *Geochimica et Cosmochimica Acta* 98: 259–81.
Seyfried, W. E. et al. 2003. "Chemistry of Hydrothermal Vent Fluids from the Main Endeavour Field, Northern Juan de Fuca Ridge: Geochemical Controls in the Aftermath of June 1999 Seismic Events." *Journal of Geophysical Research: Solid Earth* 108(B9): 1–23.
Seyfried, W E, and W C Shanks III. 2004. "Alteration and Mass Transport in Mid-Ocean Ridge Hydrothermal Systems: Controls on the Chemical and Isotopic Evolution of High-Temperature Crustal Fluids." *Hydrology of the ocean lithosphere* (October): 451–94.
Sohrin, Yoshiki et al. 2008. "Multielemental Determination of GEOTRACES Key Trace Metals in Seawater by ICPMS after Preconcentration Using an Ethylenediaminetriacetic Acid Chelating Resin." *Analytical Chemistry* 80(16): 6267–73.
Statham, P. J., C. R. German, and D. P. Connelly. 2005. "Iron (II) Distribution and Oxidation Kinetics in Hydrothermal Plumes at the Kairei and Edmond Vent Sites, Indian Ocean." *Earth and Planetary Science Letters* 236(3–4): 588–96.
Tagliabue, A., et al. 2010. "Hydrothermal Contribution to the Oceanic Dissolved Iron Inventory." *Nature Geoscience* 3(4): 252–56.
Tagliabue, A., et al. 2022. "Mechanisms Driving the Dispersal of Hydrothermal Iron From the Northern Mid Atlantic Ridge." *Geophysical Research Letters* 49(22): 1–11.
Tebo, Bradley M. et al. 2004. "Biogenic Manganese Oxides: Properties and Mechanisms of Formation." *Annual Review of Earth and Planetary Sciences* 32(Goldberg 1954): 287–328.
Thomson, R. E. et al. 1992. "Physical Characteristics of the Endeavour Ridge Hydrothermal Plume during July 1988." *Earth and Planetary Science Letters* 111(1): 141–54.

Thomson, R. E., Marina M. Subbotina, and Mikhail V. Anisimov. 2005. “Numerical Simulation of Hydrothermal Vent-Induced Circulation at Endeavour Ridge.” *Journal of Geophysical Research: Oceans* 110(1): 1–14.

Toner, Brandy M., Cara M. Santelli, et al. 2009. “Biogenic Iron Oxyhydroxide Formation at Mid-Ocean Ridge Hydrothermal Vents: Juan de Fuca Ridge.” *Geochimica et Cosmochimica Acta* 73(2): 388–403. http://dx.doi.org/10.1016/j.gca.2008.09.035.

Toner, Brandy M., Sirine C. Fakra, et al. 2009. “Preservation of Iron(II) by Carbon-Rich Matrices in a Hydrothermal Plume.” *Nature Geoscience* 2(3): 197–201.

Trocine, Robert P., and John H. Trefry. 1988. “Distribution and Chemistry of Suspended Particles from an Active Hydrothermal Vent Site on the Mid-Atlantic Ridge at 26°N.” *Earth and Planetary Science Letters* 88(1–2): 1–15.

Veirs, Scott R., Russell E. McDuff, and Frederick R. Stahr. 2006. “Magnitude and Variance of Near-Bottom Horizontal Heat Flux at the Main Endeavour Hydrothermal Vent Field.” *Geochemistry, Geophysics, Geosystems* 7(2).

Wang, Hu et al. 2021. “The Characteristics of Fe Speciation and Fe-Binding Ligands in the Mariana Back-Arc Hydrothermal Plumes.” *Geochimica et Cosmochimica Acta* 292: 24–36. https://doi.org/10.1016/j.gca.2020.09.016.

Water Properties. (n.d.). https://www.waterproperties.ca

Wilcock, William S.D. et al. 2009. “The Role of Magma Injection in Localizing Black-Smoker Activity.” *Nature Geoscience* 2(7): 509–13.

Wolf-Galdrow, Dieter A, Ulf Riebesell, Steffen Burkhardt, and Buma Jelle. 1999. “Direct Effects of CO2 Concentration on Growth and Isotopic Composition of Marine Plankton.” *Tellus B: Chemical and Physical Meteorology* 0889: 461–76.

Wu, Jingfeng, Mark L. Wells, and Robert Rember. 2011. “Dissolved Iron Anomaly in the Deep Tropical-Subtropical Pacific: Evidence for Long-Range Transport of Hydrothermal Iron.” *Geochimica et Cosmochimica Acta* 75(2): 460–68. http://dx.doi.org/10.1016/j.gca.2010.10.024.

Yücel, Mustafa, Amy Gartman, Clara S. Chan, and George W. Luther. 2011. “Hydrothermal Vents as a Kinetically Stable Source of Iron-Sulphide-Bearing Nanoparticles to the Ocean.” *Nature Geoscience* 4(6): 367–71.

Zheng, Linjie et al. 2017. “Distribution and Stoichiometry of Al, Mn, Fe, Co, Ni, Cu, Zn, Cd, and Pb in Seawater around the Juan de Fuca Ridge.” *Journal of Oceanography* 73(5): 669–85.

Appendix

Appendix A. Data tables of dissolved transition and REE

Table A1. Dissolved (<0.02 μm) transition metal concentrations.

Station	Depth	dMn	error	dFe	error	dCo	error	dCu	error
	m	nM	nM	nM	nM	nM	nM	nM	nM
END1 (47.957, -129.094)	2140	0.681	1.31E-02	2.933	5.32E-02	0.066	1.19E-03	1.695	1.05E-02
	2125	38.561	9.72E-01	17.725	6.31E-01	0.023	3.32E-04	4.036	1.32E-02
	2100	30.306	5.82E-01	13.072	4.81E-01	0.010	2.97E-04	2.624	1.48E-02
	2075	12.628	2.93E-01	7.354	1.11E-01	0.023	4.76E-04	1.571	1.73E-02
	2050	49.874	1.39E+00	22.732	4.02E-01	0.010	2.08E-04	2.491	1.70E-02
	2025	1.332	1.80E-02	1.170	2.13E-02	0.048	5.42E-04	1.334	1.59E-02
	2000	85.256	1.15E+00	45.673	1.08E+00	0.033	7.04E-04	2.620	1.15E-02
	1975	98.426	1.34E+00	68.204	7.77E-01	0.015	2.95E-04	2.303	1.30E-02
	1950	89.940	2.29E+00	63.050	1.15E+00	0.018	4.31E-04	2.489	1.25E-02
	1925	87.079	1.55E+00	59.527	1.10E+00	0.015	2.93E-04	2.403	1.83E-02
	1900	45.773	5.81E-01	24.113	6.56E-01	0.011	3.16E-04	2.445	1.05E-02
END2 (47.920, -129.144)	2200	10.427	1.00E-01	6.424	7.36E-02	0.005	1.14E-04	2.533	3.43E-02
	2150	11.363	3.04E-01	7.177	9.64E-02	0.004	1.16E-04	2.333	3.10E-02
	2125	10.578	1.95E-01	5.365	5.40E-02	0.006	1.62E-04	2.308	3.31E-02
	2100	11.111	2.03E-01	6.059	1.05E-01	0.010	2.47E-04	2.277	3.33E-02
	2075	12.676	2.56E-01	6.169	7.31E-02	0.006	1.96E-04	2.163	4.15E-02
	2050	9.343	1.44E-01	4.871	6.85E-02	0.009	1.51E-04	2.310	2.30E-02
	2025	4.254	4.81E-02	15.061	2.79E-01	0.010	2.65E-04	2.397	1.93E-02
	2000	4.550	6.47E-02	5.507	8.63E-02	0.024	7.63E-04	2.806	2.48E-02
	1975	2.157	2.45E-02	1.209	9.99E-03	0.004	1.29E-04	2.309	3.15E-02
	1950	2.256	1.73E-02	2.363	2.30E-02	0.009	2.51E-04	2.300	3.43E-02

	1925	7.117	1.06E-01	5.098	6.02E-02	0.038	7.60E-04	3.297	4.56E-02
END3 (47.871, -129.241)	2200	2.554	2.67E-02	0.349	2.90E-03	0.026	6.71E-04	1.130	1.24E-02
	2150	4.044	5.48E-02	1.988	3.07E-02	0.008	1.90E-04	2.452	2.12E-02
	2125	4.060	5.03E-02	2.679	3.42E-02	0.018	3.68E-04	2.453	2.61E-02
	2100	4.101	2.00E-02	2.189	2.86E-02	0.010	3.12E-04	2.413	3.49E-02
	2075	3.042	4.13E-02	2.666	2.96E-02	0.015	2.92E-04	2.471	2.26E-02
	2025	18.519	5.17E-01	9.262	2.32E-01	0.010	3.68E-04	3.421	4.44E-02
	2025	26.204	1.01E+00	11.602	2.29E-01	0.010	3.04E-04	3.344	6.46E-02
	2000	10.256	3.53E-01	4.595	7.02E-02	0.011	2.70E-04	3.279	4.76E-02
	1975	3.811	4.49E-02	2.350	1.09E-02	0.009	2.88E-04	3.096	5.60E-02
	1950	1.492	2.87E-02	2.468	2.67E-02	0.009	1.76E-04	3.301	3.15E-02
	1925	0.852	9.40E-03	0.596	7.97E-03	0.009	1.22E-04	2.082	2.49E-02
END4 (47.767, -129.431)	2150	2.218	3.36E-02	2.762	4.36E-02	0.015	2.73E-04	1.514	1.79E-02
	2125	2.009	1.79E-02	1.629	1.64E-02	0.013	2.86E-04	2.428	2.90E-02
	2100	2.328	3.61E-02	2.103	5.55E-02	0.024	6.00E-04	2.708	3.46E-02
	2075	2.108	3.08E-02	5.767	8.10E-02	0.018	2.73E-04	2.526	2.93E-02
	2000	12.681	2.60E-01	5.360	1.03E-01	0.022	5.64E-04	2.756	3.16E-02
	1975	10.412	1.78E-01	4.751	1.09E-01	0.022	4.46E-04	2.545	3.77E-02
	1950	5.270	6.92E-02	23.155	7.02E-01	0.077	2.13E-03	3.014	4.51E-02
	1925	1.075	1.36E-02	3.586	4.61E-02	0.021	7.59E-04	1.478	1.76E-02
END5 (47.645, -129.605)	2200	1.027	1.12E-02	2.322	2.08E-02	0.019	6.42E-04	2.185	2.47E-02
	2150	1.364	1.76E-02	2.810	3.24E-02	0.018	7.76E-04	2.049	1.13E-02
	2100	1.340	1.48E-02	1.647	1.92E-02	0.016	6.87E-04	1.660	1.10E-02
	2075	1.367	8.21E-03	4.795	4.80E-02	0.021	9.57E-04	2.145	1.86E-02
	2025	1.313	1.39E-02	2.080	2.33E-02	0.013	6.60E-04	1.976	1.90E-02
	2000	1.218	1.73E-02	1.232	1.76E-02	0.012	1.65E-04	2.078	1.81E-02
	1975	1.161	1.11E-02	2.579	2.40E-02	0.014	4.44E-04	2.134	1.77E-02
	1950	1.357	1.10E-02	3.221	2.72E-02	0.018	7.41E-04	2.247	2.51E-02
	1925	0.856	1.27E-02	2.729	2.75E-02	0.017	3.23E-04	2.382	2.69E-02

Station	Depth	dZn	error	dCd	error	dPb	error	dNi	error
	m	nM	nM	nM	nM	nM	nM	nM	nM
END1 (47.957, -129.094)	2140	11.311	1.26E-01	0.916	1.91E-02	0.059	1.32E-03	6.781	9.33E-02
	2125	23.909	1.40E-01	1.084	6.25E-03	0.025	8.49E-04	11.420	1.19E-01
	2100	13.110	7.38E-02	0.756	8.87E-03	0.013	2.14E-04	7.886	3.69E-02
	2075	7.492	9.11E-02	0.612	1.11E-02	0.020	3.65E-04	6.252	7.55E-02
	2050	14.674	6.88E-02	0.710	7.35E-03	0.016	3.57E-04	8.031	6.49E-02
	2025	3.689	5.23E-02	0.654	1.21E-02	0.039	8.32E-04	4.894	9.28E-02
	2000	17.975	1.55E-01	0.746	5.67E-03	0.022	6.21E-04	8.420	3.23E-02
	1975	16.702	1.19E-01	0.700	6.98E-03	0.044	3.75E-04	8.097	6.94E-02
	1950	17.290	1.29E-01	0.741	7.06E-03	0.025	3.33E-04	7.924	8.02E-02
	1925	17.622	5.97E-02	0.747	9.58E-03	0.026	5.34E-04	8.101	8.25E-02
	1900	12.481	1.23E-01	0.755	7.33E-03	0.014	2.29E-04	7.862	1.22E-01
END2 (47.920, -129.144)	2200	9.689	1.39E-01	0.726	1.01E-02	0.009	2.46E-04	7.747	3.45E-02
	2150	9.737	1.13E-01	0.692	1.29E-02	0.012	1.73E-04	7.444	6.16E-02
	2125	10.071	1.37E-01	0.671	9.31E-03	0.005	1.82E-04	7.664	4.63E-02
	2100	9.328	1.03E-01	0.677	1.34E-02	0.006	1.40E-04	7.841	1.19E-01
	2075	8.385	1.45E-01	0.567	5.82E-03	0.003	1.59E-04	7.891	5.65E-02
	2050	9.756	1.08E-01	0.638	8.91E-03	0.007	2.79E-04	7.859	3.79E-02
	2025	9.904	8.83E-02	0.752	1.10E-02	0.016	1.88E-04	8.067	7.84E-02
	2000	17.187	1.88E-01	0.775	1.02E-02	0.044	5.01E-04	8.324	1.35E-01
	1975	8.155	1.43E-01	0.751	1.76E-02	0.005	1.77E-04	7.831	1.19E-01
	1950	14.598	1.58E-01	0.751	1.24E-02	0.011	3.15E-04	7.877	8.17E-02
	1925	15.527	1.28E-01	1.106	1.63E-02	0.012	2.77E-04	11.120	1.81E-01
END3 (47.871, -129.241)	2200	0.246	6.53E-03	0.021	1.47E-03	0.013	3.10E-04	4.368	6.18E-02
	2150	11.054	9.36E-02	0.987	1.35E-02	0.010	1.80E-04	10.453	7.76E-02
	2125	12.706	1.45E-01	1.002	1.17E-02	0.008	1.89E-04	10.486	1.20E-01
	2100	11.677	1.24E-01	1.008	1.90E-02	0.006	1.78E-04	10.674	1.22E-01
	2075	13.213	1.06E-01	0.997	8.12E-03	0.009	3.50E-04	10.754	1.91E-01

	2025	13.427	1.66E-01	1.020	1.19E-02	0.016	2.87E-04	10.620	1.23E-01
	2025	14.048	2.27E-01	0.980	1.86E-02	0.016	5.82E-04	10.311	5.40E-02
	2000	12.405	1.45E-01	1.018	1.97E-02	0.056	7.91E-04	10.674	1.74E-01
	1975	11.672	1.80E-01	1.019	1.91E-02	0.010	2.19E-04	10.825	1.86E-01
	1950	15.094	1.64E-01	1.013	1.36E-02	0.016	2.65E-04	10.769	1.38E-01
	1925	15.688	1.68E-01	0.727	1.31E-02	0.015	5.27E-04	7.728	1.16E-01
END4 (47.767, -129.431)	2150	11.215	8.45E-02	1.099	2.62E-02	0.019	3.72E-04	11.081	1.84E-01
	2125	12.136	8.14E-02	0.969	2.34E-02	0.006	2.02E-04	10.589	5.61E-02
	2100	11.938	1.41E-01	1.025	6.62E-03	0.004	6.10E-05	11.961	8.57E-02
	2075	12.913	1.11E-01	0.991	1.95E-02	0.005	1.44E-04	11.555	1.77E-01
	2000	14.120	1.65E-01	0.982	1.52E-02	0.089	1.03E-03	11.392	1.19E-01
	1975	15.789	2.69E-01	0.999	9.69E-03	0.015	3.70E-04	11.554	1.45E-01
	1950	21.409	2.93E-01	0.952	1.33E-02	0.033	5.42E-04	13.198	1.16E-01
	1925	13.073	1.42E-01	0.715	1.60E-02	0.017	3.74E-04	8.289	1.03E-01
END5 (47.645, -129.605)	2200	15.742	1.06E-01	0.953	7.83E-03	0.015	2.63E-04	10.803	7.68E-02
	2150	18.573	1.72E-01	0.947	4.90E-03	0.039	8.25E-04	10.603	1.65E-01
	2100	13.393	8.31E-02	1.041	6.01E-03	0.011	1.51E-04	10.732	1.46E-01
	2075	23.951	2.44E-01	0.971	6.97E-03	0.042	2.85E-04	11.166	1.68E-01
	2025	12.941	1.33E-01	0.944	1.34E-02	0.010	3.73E-04	10.505	1.38E-01
	2000	11.876	1.22E-01	0.972	1.20E-02	0.133	1.12E-03	10.690	2.48E-01
	1975	13.545	1.59E-01	1.032	1.04E-02	0.034	6.50E-04	10.656	1.68E-01
	1950	15.047	7.71E-02	1.005	2.04E-02	0.041	6.96E-04	11.076	9.61E-02
	1925	12.956	1.16E-01	1.013	1.80E-02	0.021	2.75E-04	11.127	1.26E-01

Table A2. Dissolved (<0.02 μm) REE concentrations.

Station	Depth	dY	error	dLa	error	dCe	error	dNd	error
	m	nM	nM	nM	nM	nM	nM	nM	nM
END1 (47.957, -129.094)	2140	1.45E-01	4.04E-03	2.34E-02	5.24E-04	2.85E-03	8.83E-05	1.36E-02	4.18E-04
	2125	2.82E-01	6.97E-03	4.67E-02	1.54E-03	1.52E-03	3.35E-05	2.77E-02	3.71E-04
	2100	1.99E-01	6.08E-03	3.30E-02	8.57E-04	9.86E-04	3.35E-05	1.94E-02	7.76E-04
	2075	1.36E-01	3.72E-03	2.28E-02	8.33E-04	2.56E-03	1.10E-04	1.35E-02	3.03E-04
	2050	1.92E-01	7.62E-03	3.21E-02	1.57E-03	1.12E-03	4.15E-05	1.90E-02	8.25E-04
	2025	1.02E-01	3.63E-03	1.66E-02	3.93E-04	2.06E-03	8.41E-05	9.81E-03	3.47E-05
	2000	2.02E-01	6.77E-03	3.30E-02	1.10E-03	1.43E-03	6.23E-05	1.94E-02	1.15E-03
	1975	1.92E-01	6.71E-03	3.13E-02	9.44E-04	1.07E-03	3.21E-05	1.81E-02	6.40E-04
	1950	1.91E-01	6.78E-03	3.11E-02	1.39E-03	1.13E-03	2.78E-05	1.78E-02	4.16E-04
	1925	1.93E-01	7.10E-03	3.14E-02	1.09E-03	1.19E-03	5.00E-05	1.79E-02	7.30E-04
	1900	1.91E-01	7.86E-03	3.16E-02	1.37E-03	9.95E-04	5.68E-05	1.82E-02	8.17E-04
END2 (47.920, -129.144)	2200	1.93E-01	7.36E-03	3.31E-02	1.25E-03	9.49E-04	3.43E-05	1.96E-02	8.34E-04
	2150	1.86E-01	6.26E-03	3.16E-02	7.78E-04	9.63E-04	3.22E-05	1.91E-02	5.76E-04
	2125	1.94E-01	6.37E-03	3.34E-02	1.24E-03	9.98E-04	2.40E-05	1.98E-02	6.32E-04
	2100	1.92E-01	7.90E-03	3.31E-02	1.61E-03	1.17E-03	4.67E-05	1.99E-02	5.71E-04
	2075	1.94E-01	7.16E-03	3.32E-02	1.33E-03	1.04E-03	4.29E-05	1.98E-02	8.60E-04
	2050	1.99E-01	5.37E-03	3.31E-02	9.79E-04	1.41E-03	4.13E-05	1.97E-02	8.08E-04
	2025	1.95E-01	4.31E-03	3.31E-02	7.13E-04	9.81E-04	3.19E-05	1.97E-02	5.88E-04
	2000	2.00E-01	8.57E-03	3.61E-02	1.39E-03	5.05E-03	1.96E-04	2.13E-02	8.13E-04
	1975	1.92E-01	7.24E-03	3.26E-02	8.93E-04	8.32E-04	5.02E-05	1.95E-02	5.97E-04
	1950	1.89E-01	7.60E-03	3.24E-02	1.54E-03	1.05E-03	5.58E-05	1.92E-02	6.21E-04
	1925	2.66E-01	8.93E-03	4.54E-02	1.54E-03	1.91E-03	9.34E-05	2.71E-02	7.54E-04
END3 (47.871, -129.241)	2200	8.50E-02	3.29E-03	1.17E-02	5.00E-04	5.44E-03	2.83E-04	8.62E-03	4.46E-04
	2150	2.61E-01	9.50E-03	4.48E-02	1.61E-03	1.16E-03	7.23E-05	2.72E-02	1.20E-03
	2125	2.68E-01	1.14E-02	4.60E-02	1.69E-03	1.54E-03	8.50E-05	2.73E-02	8.41E-04

	2100	2.62E-01	7.43E-03	4.46E-02	2.15E-03	1.27E-03	5.22E-05	2.72E-02	1.53E-03
	2075	2.63E-01	7.88E-03	4.49E-02	1.16E-03	1.42E-03	4.74E-05	2.74E-02	1.11E-03
	2025	2.58E-01	1.14E-02	4.48E-02	2.18E-03	1.42E-03	5.58E-05	2.67E-02	5.85E-04
	2025	2.53E-01	7.65E-03	4.27E-02	1.67E-03	1.41E-03	5.40E-05	2.51E-02	9.07E-04
	2000	2.59E-01	1.02E-02	4.43E-02	1.58E-03	1.32E-03	3.51E-05	2.69E-02	1.09E-03
	1975	2.62E-01	8.46E-03	4.42E-02	1.63E-03	1.40E-03	7.49E-05	2.62E-02	8.59E-04
	1950	2.56E-01	3.70E-03	4.40E-02	9.94E-04	1.56E-03	2.67E-05	2.59E-02	8.52E-04
	1925	1.81E-01	6.22E-03	3.08E-02	1.17E-03	1.04E-03	7.16E-05	1.81E-02	4.65E-04
END4 (47.767, -129.431)	2150	2.97E-01	1.20E-02	5.19E-02	1.98E-03	1.36E-03	3.91E-05	3.02E-02	1.48E-03
	2125	2.96E-01	8.94E-03	4.86E-02	1.98E-03	1.19E-03	5.11E-05	2.79E-02	1.89E-03
	2100	3.22E-01	1.09E-02	5.04E-02	1.71E-03	1.44E-03	5.12E-05	2.94E-02	1.25E-03
	2075	3.26E-01	9.45E-03	5.01E-02	1.58E-03	1.34E-03	5.25E-05	2.92E-02	1.46E-03
	2000	3.21E-01	1.10E-02	4.81E-02	1.66E-03	1.46E-03	5.08E-05	2.71E-02	1.31E-03
	1975	3.18E-01	1.10E-02	4.81E-02	1.66E-03	1.45E-03	6.42E-05	2.73E-02	1.38E-03
	1950	2.87E-01	9.94E-03	4.49E-02	1.44E-03	2.84E-03	7.81E-05	2.57E-02	9.80E-04
	1925	2.01E-01	8.22E-03	3.24E-02	1.19E-03	1.70E-03	5.50E-05	1.84E-02	6.63E-04
END5 (47.645, -129.605)	2200	2.93E-01	8.77E-03	4.86E-02	1.26E-03	1.30E-03	4.06E-05	2.79E-02	6.83E-04
	2150	2.88E-01	1.04E-02	4.79E-02	1.85E-03	1.64E-03	5.88E-05	2.71E-02	1.21E-03
	2100	2.79E-01	1.10E-02	4.87E-02	1.80E-03	1.39E-03	4.37E-05	2.81E-02	1.46E-03
	2075	2.83E-01	7.65E-03	4.71E-02	1.13E-03	1.87E-03	6.61E-05	2.65E-02	9.06E-04
	2025	2.78E-01	8.07E-03	4.54E-02	1.27E-03	1.55E-03	3.89E-05	2.57E-02	1.03E-03
	2000	2.83E-01	1.02E-02	4.65E-02	1.33E-03	1.42E-03	5.53E-05	2.61E-02	6.14E-04
	1975	2.77E-01	8.94E-03	4.73E-02	1.09E-03	1.75E-03	8.20E-05	2.70E-02	4.36E-04
	1950	2.85E-01	9.39E-03	4.67E-02	1.20E-03	2.12E-03	2.73E-05	2.68E-02	7.47E-04
	1925	2.79E-01	7.92E-03	4.69E-02	1.07E-03	1.96E-03	9.70E-05	2.66E-02	5.81E-04

Station	Depth	dSm	error	dEu	error	dGd	error	dTb	error	dDy	error
	m	nM	nM	nM	nM	nM	nM	nM	nM	nM	nM
END1 (47.957, -129.094)	2140	2.59E-03	1.71E-04	6.20E-04	2.97E-05	4.02E-03	1.78E-04	5.16E-04	2.33E-05	5.07E-03	2.53E-04
	2125	5.17E-03	1.99E-04	1.43E-03	4.11E-05	8.10E-03	1.69E-04	1.19E-03	6.71E-05	1.03E-02	4.50E-04
	2100	3.53E-03	3.22E-04	9.42E-04	3.40E-05	5.73E-03	2.46E-04	7.90E-04	1.74E-05	7.10E-03	2.59E-04
	2075	2.55E-03	1.33E-04	5.71E-04	2.23E-05	3.75E-03	2.48E-04	4.97E-04	3.85E-05	4.60E-03	2.68E-04
	2050	3.31E-03	1.51E-04	9.45E-04	2.45E-05	5.34E-03	3.40E-04	7.54E-04	3.69E-05	6.73E-03	4.32E-04
	2025	1.79E-03	1.02E-04	3.69E-04	1.25E-05	2.74E-03	2.14E-04	3.43E-04	9.74E-06	3.47E-03	1.86E-04
	2000	3.72E-03	2.62E-04	1.01E-03	5.81E-05	5.47E-03	3.04E-04	7.69E-04	4.34E-05	6.98E-03	1.59E-04
	1975	3.34E-03	2.15E-04	8.95E-04	4.40E-05	5.43E-03	2.90E-04	7.06E-04	2.77E-05	6.65E-03	2.63E-04
	1950	3.25E-03	2.03E-04	8.74E-04	3.64E-05	5.29E-03	3.92E-04	7.34E-04	4.37E-05	6.49E-03	2.57E-04
	1925	3.37E-03	2.50E-04	8.58E-04	6.04E-05	5.39E-03	2.07E-04	7.67E-04	1.92E-05	6.50E-03	3.59E-04
	1900	3.49E-03	1.88E-04	8.42E-04	5.16E-05	5.25E-03	2.14E-04	7.34E-04	4.33E-05	6.49E-03	2.63E-04
END2 (47.920, -129.144)	2200	3.64E-03	3.85E-04	1.00E-03	7.32E-05	5.83E-03	2.38E-04	8.25E-04	5.69E-05	7.17E-03	3.05E-04
	2150	3.56E-03	2.84E-04	9.43E-04	3.59E-05	5.56E-03	2.67E-04	7.94E-04	6.14E-05	6.88E-03	3.42E-04
	2125	3.74E-03	2.44E-04	9.94E-04	6.76E-05	5.91E-03	2.42E-04	8.35E-04	4.25E-05	7.16E-03	3.65E-04
	2100	3.58E-03	4.05E-04	9.77E-04	5.41E-05	5.86E-03	1.71E-04	8.49E-04	8.04E-05	7.29E-03	3.82E-04
	2075	3.61E-03	3.23E-04	9.19E-04	6.59E-05	5.90E-03	3.65E-04	8.27E-04	4.13E-05	7.36E-03	3.07E-04
	2050	3.66E-03	1.50E-04	9.45E-04	2.55E-05	6.06E-03	2.69E-04	8.27E-04	4.05E-05	7.24E-03	3.56E-04
	2025	3.55E-03	1.48E-04	8.92E-04	4.09E-05	5.64E-03	3.32E-04	8.03E-04	4.02E-05	7.14E-03	1.14E-04
	2000	3.78E-03	4.01E-04	1.03E-03	4.65E-05	5.77E-03	3.39E-04	8.77E-04	7.23E-05	7.36E-03	2.70E-04
	1975	3.64E-03	2.46E-04	9.05E-04	3.95E-05	5.91E-03	4.07E-04	7.94E-04	4.41E-05	7.09E-03	2.55E-04
	1950	3.48E-03	2.33E-04	9.11E-04	6.74E-05	5.64E-03	3.46E-04	7.66E-04	4.45E-05	6.77E-03	2.82E-04
	1925	4.86E-03	3.25E-04	1.34E-03	1.11E-04	8.12E-03	3.14E-04	1.19E-03	4.98E-05	1.01E-02	1.67E-04
END3 (47.871, -129.241)	2200	1.50E-03	2.37E-04	3.78E-04	4.28E-05	2.31E-03	1.27E-04	2.51E-04	2.93E-05	2.53E-03	1.10E-04
	2150	5.11E-03	2.98E-04	1.31E-03	8.15E-05	8.00E-03	1.62E-04	1.18E-03	4.37E-05	9.43E-03	3.84E-04
	2125	5.19E-03	3.49E-04	1.36E-03	8.81E-05	8.08E-03	3.92E-04	1.17E-03	4.20E-05	9.92E-03	4.56E-04
	2100	5.01E-03	2.28E-04	1.34E-03	5.75E-05	7.91E-03	5.20E-04	1.14E-03	7.15E-05	9.80E-03	5.33E-04
	2075	5.23E-03	3.12E-04	1.28E-03	1.03E-04	8.08E-03	3.79E-04	1.16E-03	6.17E-05	9.79E-03	2.58E-04

	2025	4.85E-03	5.25E-04	1.33E-03	7.05E-05	7.67E-03	2.92E-04	1.17E-03	6.64E-05	9.66E-03	4.01E-04
	2025	4.45E-03	3.29E-04	1.23E-03	5.26E-05	7.44E-03	4.11E-04	1.05E-03	4.02E-05	9.35E-03	3.50E-04
	2000	4.95E-03	3.36E-04	1.36E-03	6.78E-05	7.89E-03	2.60E-04	1.11E-03	4.69E-05	9.52E-03	4.25E-04
	1975	4.84E-03	2.70E-04	1.27E-03	1.10E-04	7.95E-03	4.43E-04	1.15E-03	3.14E-05	9.44E-03	2.04E-04
	1950	4.66E-03	2.23E-04	1.28E-03	8.60E-05	7.77E-03	4.95E-04	1.11E-03	5.05E-05	9.52E-03	4.65E-04
	1925	3.19E-03	1.26E-04	8.46E-04	6.66E-05	5.38E-03	3.09E-04	7.16E-04	3.41E-05	6.56E-03	1.73E-04
END4 (47.767, -129.431)	2150	5.54E-03	2.86E-04	1.52E-03	5.20E-05	8.85E-03	2.57E-04	1.38E-03	6.34E-05	1.11E-02	4.40E-04
	2125	5.00E-03	2.69E-04	1.36E-03	8.74E-05	8.30E-03	4.23E-04	1.23E-03	6.75E-05	9.96E-03	2.74E-04
	2100	5.60E-03	5.81E-04	1.46E-03	4.03E-05	8.83E-03	4.50E-04	1.31E-03	6.01E-05	1.06E-02	5.39E-04
	2075	6.27E-03	4.69E-04	1.43E-03	1.03E-04	8.46E-03	6.72E-04	1.28E-03	7.99E-05	1.02E-02	4.87E-04
	2000	5.28E-03	1.55E-04	1.32E-03	9.04E-05	8.19E-03	4.84E-04	1.20E-03	6.92E-05	9.99E-03	2.07E-04
	1975	5.24E-03	1.41E-04	1.36E-03	9.33E-05	8.02E-03	3.03E-04	1.22E-03	6.43E-05	9.84E-03	3.78E-04
	1950	4.95E-03	2.12E-04	1.56E-03	1.18E-04	7.55E-03	3.43E-04	1.36E-03	5.60E-05	9.43E-03	3.09E-04
	1925	3.20E-03	1.26E-04	8.52E-04	4.04E-05	5.23E-03	2.85E-04	7.64E-04	2.68E-05	6.35E-03	3.75E-04
END5 (47.645, -129.605)	2200	5.25E-03	3.96E-04	1.43E-03	1.18E-04	8.16E-03	2.19E-04	1.28E-03	2.03E-05	1.02E-02	4.15E-04
	2150	5.10E-03	2.47E-04	1.31E-03	5.31E-05	8.06E-03	2.94E-04	1.22E-03	8.15E-05	9.87E-03	5.38E-04
	2100	4.91E-03	2.53E-04	1.42E-03	1.06E-04	8.19E-03	3.86E-04	1.27E-03	3.92E-05	1.01E-02	5.20E-04
	2075	4.73E-03	1.97E-04	1.42E-03	8.09E-05	7.55E-03	3.29E-04	1.23E-03	5.42E-05	9.44E-03	4.33E-04
	2025	4.64E-03	4.36E-04	1.17E-03	2.15E-05	7.50E-03	1.66E-04	1.18E-03	4.16E-05	9.06E-03	3.67E-04
	2000	4.75E-03	2.41E-04	1.19E-03	1.06E-04	7.68E-03	2.73E-04	1.18E-03	5.97E-05	9.36E-03	3.63E-04
	1975	4.92E-03	2.16E-04	1.29E-03	1.01E-04	8.20E-03	2.72E-04	1.22E-03	5.97E-05	9.77E-03	4.79E-04
	1950	4.82E-03	3.76E-04	1.30E-03	7.48E-05	7.73E-03	2.56E-04	1.16E-03	5.66E-05	9.19E-03	3.02E-04
	1925	4.86E-03	2.22E-04	1.35E-03	3.67E-05	7.96E-03	3.01E-04	1.21E-03	6.72E-05	9.39E-03	4.59E-04

Station	Depth	dHo	error	dEr	error	dTm	error	dYb	error	dLu	error
	m	nM	nM	nM	nM	nM	nM	nM	nM	nM	nM
END1 (47.957, -129.094)	2140	1.21E-03	5.06E-05	4.45E-03	3.77E-04	5.59E-04	3.33E-05	4.15E-03	2.10E-04	6.33E-04	4.76E-05
	2125	2.73E-03	1.06E-04	9.83E-03	1.90E-04	1.48E-03	6.28E-05	1.07E-02	5.02E-04	1.83E-03	8.59E-05
	2100	1.91E-03	4.78E-05	6.93E-03	3.30E-04	1.01E-03	3.14E-05	7.65E-03	4.87E-04	1.28E-03	7.30E-05
	2075	1.16E-03	6.48E-05	4.28E-03	1.90E-04	5.42E-04	2.54E-05	4.54E-03	3.18E-04	7.15E-04	1.20E-05
	2050	1.81E-03	1.06E-04	6.67E-03	3.23E-04	9.29E-04	6.05E-05	7.43E-03	2.78E-04	1.26E-03	3.79E-05
	2025	8.01E-04	4.79E-05	3.08E-03	1.25E-04	3.59E-04	1.31E-05	2.93E-03	1.92E-04	4.29E-04	2.78E-05
	2000	1.87E-03	5.98E-05	6.95E-03	2.48E-04	9.65E-04	4.27E-05	7.63E-03	1.93E-04	1.30E-03	4.18E-05
	1975	1.76E-03	5.13E-05	6.53E-03	2.71E-04	9.47E-04	4.46E-05	7.38E-03	3.26E-04	1.23E-03	6.40E-05
	1950	1.68E-03	8.14E-05	6.53E-03	3.96E-04	9.34E-04	3.90E-05	7.06E-03	3.58E-04	1.24E-03	4.59E-05
	1925	1.76E-03	7.51E-05	6.53E-03	1.31E-04	9.59E-04	3.89E-05	7.36E-03	3.52E-04	1.24E-03	4.07E-05
	1900	1.75E-03	9.17E-05	6.50E-03	2.81E-04	9.25E-04	2.88E-05	7.48E-03	2.95E-04	1.23E-03	6.14E-05
END2 (47.920, -129.144)	2200	1.87E-03	8.20E-05	6.78E-03	4.24E-04	9.76E-04	4.35E-05	7.61E-03	5.12E-04	1.29E-03	9.59E-05
	2150	1.83E-03	6.41E-05	6.81E-03	1.84E-04	9.75E-04	4.96E-05	7.26E-03	4.03E-04	1.27E-03	5.38E-05
	2125	1.88E-03	9.18E-05	7.12E-03	3.20E-04	1.02E-03	5.58E-05	7.75E-03	3.75E-04	1.32E-03	4.34E-05
	2100	1.95E-03	1.31E-04	7.07E-03	3.97E-04	9.93E-04	6.75E-05	7.79E-03	2.95E-04	1.31E-03	8.83E-05
	2075	1.92E-03	5.33E-05	7.08E-03	3.35E-04	9.71E-04	2.19E-05	7.66E-03	4.37E-04	1.30E-03	4.73E-05
	2050	1.87E-03	1.26E-04	6.99E-03	4.60E-04	1.02E-03	5.38E-05	7.81E-03	2.15E-04	1.32E-03	4.42E-05
	2025	1.88E-03	6.44E-05	7.00E-03	1.57E-04	9.51E-04	3.15E-05	7.59E-03	3.42E-04	1.31E-03	6.74E-05
	2000	1.93E-03	8.75E-05	7.05E-03	5.78E-04	1.03E-03	6.62E-05	7.71E-03	2.73E-04	1.27E-03	4.12E-05
	1975	1.83E-03	5.91E-05	6.82E-03	2.43E-04	9.61E-04	5.95E-05	7.50E-03	5.64E-04	1.31E-03	7.40E-05
	1950	1.78E-03	1.21E-04	6.56E-03	4.28E-04	9.66E-04	4.91E-05	7.38E-03	2.98E-04	1.24E-03	7.38E-05
	1925	2.68E-03	1.30E-04	9.70E-03	2.57E-04	1.45E-03	7.60E-05	1.08E-02	4.52E-04	1.84E-03	8.31E-05
END3 (47.871, -129.241)	2200	5.91E-04	2.57E-05	2.22E-03	1.25E-04	2.24E-04	2.62E-05	1.50E-03	9.12E-05	1.50E-04	1.68E-05
	2150	2.58E-03	7.69E-05	9.24E-03	5.94E-04	1.33E-03	7.20E-05	1.02E-02	2.34E-04	1.75E-03	1.45E-04
	2125	2.63E-03	7.69E-05	9.47E-03	3.31E-04	1.39E-03	3.30E-05	9.83E-03	3.33E-04	1.63E-03	2.75E-05
	2100	2.63E-03	1.16E-04	9.32E-03	3.83E-04	1.39E-03	1.01E-04	1.01E-02	4.01E-04	1.72E-03	7.25E-05
	2075	2.55E-03	6.21E-05	9.39E-03	3.55E-04	1.40E-03	5.53E-05	1.03E-02	2.72E-04	1.78E-03	8.58E-05

	2025	2.61E-03	1.48E-04	9.34E-03	5.82E-04	1.36E-03	7.28E-05	1.03E-02	6.39E-04	1.79E-03	6.89E-05
	2025	2.42E-03	8.62E-05	9.12E-03	3.35E-04	1.30E-03	3.74E-05	9.73E-03	4.26E-04	1.66E-03	5.40E-05
	2000	2.55E-03	5.65E-05	9.65E-03	3.87E-04	1.35E-03	4.65E-05	1.03E-02	5.68E-04	1.75E-03	6.37E-05
	1975	2.49E-03	9.56E-05	9.17E-03	3.11E-04	1.33E-03	4.49E-05	1.02E-02	3.48E-04	1.75E-03	4.78E-05
	1950	2.50E-03	6.07E-05	9.05E-03	4.81E-04	1.32E-03	5.78E-05	1.02E-02	2.30E-04	1.74E-03	2.91E-05
	1925	1.72E-03	3.93E-05	6.36E-03	4.57E-04	8.95E-04	2.08E-05	7.15E-03	3.61E-04	1.17E-03	5.08E-05
END4 (47.767, -129.431)	2150	3.15E-03	1.27E-04	1.08E-02	4.87E-04	1.69E-03	6.34E-05	1.16E-02	5.34E-04	2.06E-03	1.20E-04
	2125	2.86E-03	5.86E-05	9.79E-03	4.08E-04	1.43E-03	3.31E-05	1.01E-02	2.93E-04	1.79E-03	9.76E-05
	2100	2.91E-03	7.99E-05	1.03E-02	4.62E-04	1.53E-03	9.42E-05	1.06E-02	2.32E-04	1.92E-03	3.20E-05
	2075	2.88E-03	9.51E-05	1.00E-02	4.51E-04	1.47E-03	5.31E-05	1.05E-02	4.42E-04	1.87E-03	1.18E-04
	2000	2.83E-03	1.01E-04	9.56E-03	3.57E-04	1.44E-03	7.07E-05	1.02E-02	5.87E-04	1.80E-03	7.91E-05
	1975	2.78E-03	1.43E-04	9.50E-03	6.75E-04	1.47E-03	4.16E-05	9.97E-03	3.58E-04	1.76E-03	6.20E-05
	1950	2.69E-03	9.88E-05	9.05E-03	3.23E-04	1.49E-03	9.96E-05	9.69E-03	4.04E-04	1.84E-03	5.81E-05
	1925	1.79E-03	9.54E-05	6.22E-03	2.79E-04	9.39E-04	2.75E-05	6.69E-03	1.33E-04	1.14E-03	6.48E-05
END5 (47.645, -129.605)	2200	2.78E-03	6.59E-05	9.78E-03	3.68E-04	1.43E-03	5.61E-05	1.01E-02	4.21E-04	1.78E-03	8.64E-05
	2150	2.73E-03	8.48E-05	9.38E-03	4.68E-04	1.43E-03	7.42E-05	1.00E-02	2.53E-04	1.72E-03	4.56E-05
	2100	2.91E-03	1.89E-04	9.94E-03	3.35E-04	1.49E-03	1.17E-04	1.05E-02	6.89E-04	1.85E-03	2.23E-05
	2075	2.68E-03	8.69E-05	9.04E-03	3.33E-04	1.38E-03	4.96E-05	9.91E-03	6.28E-04	1.69E-03	8.18E-05
	2025	2.64E-03	9.42E-05	8.85E-03	4.13E-04	1.38E-03	5.32E-05	9.54E-03	2.51E-04	1.70E-03	5.48E-05
	2000	2.63E-03	4.97E-05	8.78E-03	3.63E-04	1.37E-03	3.87E-05	9.68E-03	5.56E-04	1.71E-03	9.94E-05
	1975	2.80E-03	9.83E-05	9.52E-03	2.62E-04	1.49E-03	9.09E-05	1.02E-02	2.32E-04	1.86E-03	6.46E-05
	1950	2.69E-03	1.03E-04	9.28E-03	3.53E-04	1.39E-03	4.50E-05	9.68E-03	3.81E-04	1.75E-03	4.24E-05
	1925	2.71E-03	1.38E-04	9.36E-03	3.43E-04	1.42E-03	5.81E-05	1.00E-02	3.63E-04	1.77E-03	7.82E-05

Appendix B. Data tables of total dissolved transition and REE.

Table B1. Total dissolved (>0.02 μm) transition metal concentrations.

Station	Depth	dMn	error	dFe	error	dCo	error	dCu	error
	m	nM	nM	nM	nM	nM	nM	nM	nM
END1 (47.957, -129.094)	2140	0.777	0.010	1.305	0.019	0.066	0.001	1.900	0.035
	2125	39.269	0.592	48.212	1.019	0.019	0.000	4.217	0.034
	2100	44.856	0.588	52.497	1.396	0.018	0.000	4.444	0.028
	2075	16.763	0.258	21.260	0.474	0.041	0.001	2.643	0.010
	2050	74.661	1.166	95.311	1.455	0.027	0.001	5.359	0.045
	2025	1.003	0.013	2.425	0.036	0.078	0.001	1.802	0.030
	2000	113.466	1.524	132.007	1.569	0.029	0.001	6.071	0.060
	1975	135.217	1.882	179.023	2.696	0.032	0.001	6.917	0.041
	1950	128.416	2.053	179.514	1.382	0.039	0.001	7.054	0.054
	1925	118.763	1.573	171.182	4.437	0.037	0.001	6.762	0.039
	1900	66.072	0.672	97.399	2.133	0.029	0.001	6.018	0.065
END2 (47.920, -129.144)	2200	11.730	0.380	13.246	0.374	0.007	0.000	2.525	0.029
	2150	12.810	0.612	13.245	0.396	0.007	0.000	2.461	0.016
	2125	11.486	0.336	12.658	0.465	0.007	0.000	2.457	0.017
	2100	11.837	0.421	14.397	0.837	0.033	0.001	2.514	0.032
	2075	14.576	0.269	13.436	0.338	0.007	0.000	2.448	0.013
	2050	10.066	0.280	10.405	0.212	0.007	0.000	2.413	0.022
	2025	5.261	0.059	8.022	0.101	0.005	0.000	2.276	0.018
	2000	5.515	0.071	8.744	0.193	0.009	0.000	2.343	0.032
	1975	3.532	0.034	7.128	0.083	0.024	0.001	2.556	0.017
	1950	3.501	0.042	6.981	0.079	0.009	0.000	2.271	0.022
	1925	5.910	0.046	11.041	0.292	0.009	0.000	2.258	0.031
	2200	2.643	0.032	1.640	0.021	0.038	0.001	1.156	0.018

END3 (47.871, -129.241)	2150	7.661	0.092	7.658	0.070	0.017	0.000	2.610	0.013
	2125	7.272	0.071	8.214	0.078	0.018	0.001	3.049	0.043
	2100	6.761	0.085	6.581	0.053	0.018	0.000	2.221	0.019
	2075	5.676	0.072	5.055	0.068	0.014	0.000	2.331	0.022
	2050	21.668	0.263	26.159	0.678	0.019	0.000	3.952	0.036
	2025	29.116	0.502	34.883	1.146	0.020	0.000	3.885	0.023
	2000	13.047	0.226	18.394	0.630	0.019	0.000	3.562	0.030
	1975	6.103	0.079	12.411	0.235	0.018	0.001	3.366	0.055
	1950	3.396	0.048	8.851	0.099	0.020	0.001	3.310	0.029
	1925	3.137	0.046	8.054	0.101	0.017	0.000	3.145	0.038
END4 (47.767, -129.431)	2150	5.575	0.045	6.270	0.019	0.017	0.000	2.632	0.040
	2125	4.998	0.061	5.883	0.063	0.015	0.000	2.451	0.020
	2100	4.489	0.054	9.800	0.124	0.018	0.000	3.273	0.042
	2075	4.355	0.070	8.836	0.150	0.018	0.001	3.331	0.025
	2000	13.264	0.645	11.819	0.433	0.022	0.000	2.346	0.016
	1975	11.215	0.285	14.404	0.425	0.018	0.001	2.574	0.021
	1950	6.264	0.050	8.175	0.099	0.018	0.001	1.894	0.018
	1925	2.415	0.025	0.562	0.004	0.018	0.000	2.115	0.027
END5 (47.645, -129.605)	2200	3.502	0.045	3.402	0.045	0.015	0.000	2.009	0.020
	2150	3.451	0.046	4.535	0.052	0.011	0.000	2.153	0.022
	2100	3.267	0.043	5.118	0.074	0.014	0.001	2.233	0.026
	2075	2.918	0.039	4.632	0.052	0.014	0.000	2.321	0.009
	2025	2.796	0.043	5.544	0.067	0.015	0.001	2.413	0.027
	2000	2.727	0.077	4.220	0.114	0.015	0.000	1.928	0.036
	1975	2.584	0.017	5.364	0.062	0.016	0.000	2.269	0.028
	1950	2.167	0.030	3.577	0.050	0.015	0.000	2.087	0.028
	1925	1.980	0.030	3.945	0.051	0.016	0.000	1.717	0.015

Station	Depth m	dZn nM	error nM	dCd nM	error nM	dPb nM	error nM	dNi nM	error nM
END1 (47.957, -129.094)	2140	5.491	0.068	0.921	0.018	0.059	0.001	10.406	0.124
	2125	16.082	0.073	1.077	0.016	0.039	0.001	10.214	0.097
	2100	17.115	0.143	1.048	0.003	0.039	0.001	10.364	0.073
	2075	8.682	0.070	0.801	0.013	0.037	0.001	8.458	0.132
	2050	27.012	0.272	1.126	0.015	0.067	0.001	10.419	0.037
	2025	6.783	0.079	0.921	0.020	0.058	0.001	10.488	0.134
	2000	23.895	0.073	1.080	0.008	0.076	0.001	10.414	0.091
	1975	26.841	0.207	1.076	0.011	0.119	0.002	11.116	0.054
	1950	27.828	0.163	1.080	0.012	0.084	0.001	10.555	0.105
	1925	24.987	0.195	1.100	0.011	0.080	0.001	11.048	0.141
	1900	20.361	0.184	1.095	0.010	0.051	0.001	10.571	2.560
END2 (47.920, -129.144)	2200	8.705	0.038	0.724	0.008	0.013	0.000	10.642	0.212
	2150	8.607	0.074	0.709	0.009	0.017	0.000	7.741	0.088
	2125	9.536	0.087	0.716	0.011	0.015	0.000	10.753	0.137
	2100	12.600	0.118	0.719	0.010	0.017	0.000	7.661	0.074
	2075	9.256	0.088	0.704	0.009	0.021	0.000	10.983	0.136
	2050	8.416	0.084	0.710	0.017	0.018	0.000	10.865	0.148
	2025	7.758	0.118	0.720	0.015	0.007	0.000	10.686	0.127
	2000	8.561	0.082	0.735	0.011	0.037	0.001	7.700	0.098
	1975	9.667	0.088	0.741	0.004	0.010	0.000	10.887	0.155
	1950	8.122	0.083	0.763	0.015	0.009	0.000	7.579	0.152
	1925	9.868	0.158	0.720	0.012	0.017	0.000	10.888	0.159
END3 (47.871, -129.241)	2200	1.740	0.018	0.034	0.001	0.014	0.000	10.796	0.107
	2150	20.393	0.113	1.002	0.009	0.013	0.000	11.286	0.146
	2125	11.696	0.170	1.006	0.014	0.011	0.000	10.442	0.060
	2100	11.433	0.079	1.035	0.013	0.012	0.000	10.865	0.137

	2075	11.626	0.150	0.980	0.010	0.009	0.000	10.867	0.118
	2050	14.162	0.170	1.072	0.009	0.026	0.000	11.083	0.098
	2025	14.593	0.128	1.001	0.011	0.032	0.000	11.332	0.158
	2000	12.625	0.088	1.027	0.018	0.075	0.001	10.816	0.134
	1975	12.417	0.199	0.995	0.007	0.017	0.000	7.365	0.124
	1950	12.603	0.078	1.091	0.012	0.015	0.000	11.208	0.108
	1925	13.721	0.146	1.011	0.008	0.015	0.000	7.754	0.096
END4 (47.767, -129.431)	2150	11.763	0.158	0.959	0.017	0.014	0.000	7.668	0.101
	2125	10.886	0.088	0.977	0.015	0.009	0.000	7.483	0.043
	2100	12.743	0.160	1.037	0.014	0.010	0.000	10.642	0.161
	2075	12.171	0.100	1.078	0.013	0.013	0.000	7.693	0.083
	2000	11.349	0.065	1.061	0.023	0.103	0.003	7.849	0.144
	1975	13.277	0.127	1.004	0.020	0.021	0.000	7.567	0.116
	1950	9.664	0.109	1.012	0.016	0.018	0.000	10.924	0.139
	1925	15.324	0.174	0.993	0.016	0.017	0.000	10.732	0.153
END5 (47.645, -129.605)	2200	10.205	0.094	1.077	0.011	0.013	0.000	11.152	0.092
	2150	12.282	0.133	0.976	0.011	0.021	0.000	10.289	0.123
	2100	12.347	0.107	1.028	0.015	0.011	0.000	10.613	0.085
	2075	18.814	0.170	0.979	0.009	0.026	0.000	11.152	0.144
	2025	11.306	0.102	0.985	0.008	0.009	0.000	11.147	0.145
	2000	10.942	0.160	0.944	0.026	0.128	0.003	11.086	0.173
	1975	11.924	0.120	0.969	0.009	0.024	0.000	11.344	0.155
	1950	11.064	0.126	0.968	0.011	0.022	0.000	10.512	0.078
	1925	11.940	0.079	0.963	0.007	0.016	0.001	11.221	0.086

Table B2. Total dissolved (>0.02 μm) REE concentrations.

Station	Depth	tY	error	tLa	error	tCe	error	tNd	error
	m	nM	nM	nM	nM	nM	nM	nM	nM
END1 (47.957, -129.094)	2140	2.86E-01	8.81E-03	5.25E-02	1.57E-03	2.47E-03	6.08E-05	3.10E-02	1.31E-03
	2125	2.83E-01	6.81E-03	4.82E-02	1.94E-03	2.42E-03	1.56E-04	2.82E-02	1.56E-03
	2100	2.82E-01	1.14E-02	4.86E-02	1.67E-03	2.42E-03	2.09E-04	2.73E-02	1.31E-03
	2075	1.85E-01	6.45E-03	3.13E-02	9.32E-04	4.55E-03	2.56E-04	1.84E-02	4.43E-04
	2050	2.75E-01	1.19E-02	4.67E-02	1.78E-03	2.35E-03	1.09E-04	2.70E-02	1.19E-03
	2025	2.79E-01	9.90E-03	4.62E-02	1.75E-03	2.61E-03	1.03E-04	2.65E-02	1.52E-03
	2000	2.74E-01	1.08E-02	4.62E-02	1.43E-03	2.50E-03	1.06E-04	2.62E-02	1.13E-03
	1975	2.80E-01	1.13E-02	4.81E-02	2.20E-03	3.22E-03	2.42E-04	2.83E-02	1.66E-03
	1950	2.81E-01	8.98E-03	4.63E-02	1.05E-03	2.86E-03	1.54E-04	2.66E-02	7.61E-04
	1925	2.78E-01	8.80E-03	4.86E-02	1.29E-03	3.28E-03	9.95E-05	2.88E-02	7.73E-04
	1900	2.91E-01	5.05E-01	4.96E-02	3.17E-02	2.49E-03	2.09E-03	2.84E-02	2.65E-02
END2 (47.920, -129.144)	2200	2.85E-01	1.19E-02	4.95E-02	1.13E-03	3.20E-03	3.13E-04	2.98E-02	1.36E-03
	2150	1.64E-01	4.88E-03	2.62E-02	8.47E-04	1.02E-03	5.94E-05	1.12E-02	7.01E-04
	2125	2.85E-01	8.26E-03	5.10E-02	1.16E-03	3.08E-03	8.69E-05	3.04E-02	9.79E-04
	2100	1.92E-01	7.29E-03	3.33E-02	1.72E-03	3.10E-03	2.03E-04	2.01E-02	6.11E-04
	2075	2.79E-01	7.85E-03	4.72E-02	1.44E-03	2.90E-03	1.68E-04	2.75E-02	1.55E-03
	2050	2.84E-01	1.23E-02	4.70E-02	2.35E-03	2.91E-03	2.19E-04	2.66E-02	1.44E-03
	2025	2.81E-01	1.10E-02	4.62E-02	1.38E-03	2.97E-03	1.22E-04	2.64E-02	8.19E-04
	2000	1.89E-01	7.01E-03	3.31E-02	1.36E-03	2.10E-03	9.46E-05	1.99E-02	6.24E-04
	1975	3.03E-01	1.24E-02	5.02E-02	1.66E-03	3.00E-03	1.52E-04	2.92E-02	1.64E-03
	1950	1.85E-01	6.90E-03	3.27E-02	8.42E-04	2.29E-03	1.13E-04	1.96E-02	9.79E-04
	1925	2.93E-01	1.27E-02	4.84E-02	1.80E-03	3.06E-03	1.22E-04	2.82E-02	1.49E-03
	2200	2.99E-01	6.94E-03	4.90E-02	1.71E-03	2.77E-03	8.03E-05	2.86E-02	9.55E-04
	2150	3.02E-01	9.51E-03	5.03E-02	1.84E-03	3.12E-03	1.65E-04	2.93E-02	1.67E-03

END3 (47.871, -129.241)	2125	2.94E-01	9.61E-03	4.83E-02	1.31E-03	3.21E-03	1.36E-04	2.87E-02	7.93E-04
	2100	2.92E-01	7.73E-03	4.94E-02	1.56E-03	3.26E-03	9.12E-05	2.87E-02	6.85E-04
	2075	2.94E-01	9.79E-03	4.81E-02	1.33E-03	3.51E-03	1.68E-04	2.81E-02	5.33E-04
	2050	2.95E-01	1.02E-02	4.88E-02	1.34E-03	3.65E-03	1.04E-04	2.90E-02	8.67E-04
	2025	2.96E-01	7.89E-03	5.14E-02	1.43E-03	4.29E-03	1.22E-04	3.04E-02	8.63E-04
	2000	2.94E-01	8.89E-03	4.87E-02	1.03E-03	3.33E-03	4.83E-05	2.85E-02	8.08E-04
	1975	1.87E-01	7.50E-03	3.29E-02	1.24E-03	2.09E-03	8.48E-05	1.98E-02	6.52E-04
	1950	2.96E-01	1.06E-02	5.01E-02	1.90E-03	3.97E-03	8.94E-05	2.97E-02	1.53E-03
	1925	1.92E-01	5.82E-03	3.34E-02	1.17E-03	3.97E-03	1.23E-04	2.04E-02	8.05E-04
END4 (47.767, -129.431)	2150	1.87E-01	7.77E-03	3.25E-02	1.90E-03	2.02E-03	1.40E-04	2.00E-02	1.46E-03
	2125	1.86E-01	7.36E-03	3.24E-02	9.65E-04	1.90E-03	5.43E-05	1.93E-02	5.82E-04
	2100	2.24E-01	1.30E-02	3.78E-02	2.41E-03	2.11E-03	8.74E-05	2.05E-02	1.14E-03
	2075	1.87E-01	5.38E-03	3.33E-02	8.72E-04	2.22E-03	1.31E-04	2.00E-02	3.32E-04
	2000	1.91E-01	7.08E-03	3.33E-02	1.29E-03	2.44E-03	1.22E-04	1.95E-02	1.10E-03
	1975	1.85E-01	6.51E-03	3.19E-02	7.73E-04	2.04E-03	6.48E-05	1.88E-02	5.13E-04
	1950	2.81E-01	9.31E-03	4.71E-02	1.53E-03	2.90E-03	1.28E-04	2.70E-02	1.33E-03
	1925	2.82E-01	1.15E-02	4.65E-02	1.90E-03	3.02E-03	1.52E-04	2.64E-02	1.32E-03
END5 (47.645, -129.605)	2200	2.79E-01	6.97E-03	4.80E-02	1.16E-03	2.89E-03	1.68E-04	2.87E-02	7.56E-04
	2150	2.83E-01	7.04E-03	4.84E-02	1.50E-03	2.42E-03	8.39E-05	2.78E-02	1.29E-03
	2100	2.81E-01	8.32E-03	4.87E-02	1.61E-03	2.35E-03	6.99E-05	2.82E-02	1.02E-03
	2075	2.77E-01	1.12E-02	4.74E-02	1.84E-03	3.43E-03	2.18E-04	2.89E-02	9.55E-04
	2025	2.78E-01	1.39E-02	4.82E-02	2.31E-03	3.17E-03	1.72E-04	2.84E-02	1.64E-03
	2000	2.82E-01	1.24E-02	4.81E-02	1.96E-03	3.26E-03	1.32E-04	2.81E-02	9.38E-04
	1975	2.85E-01	9.78E-03	4.88E-02	1.62E-03	3.42E-03	1.69E-04	2.92E-02	9.37E-04
	1950	2.78E-01	1.06E-02	4.61E-02	1.56E-03	2.83E-03	8.63E-05	2.64E-02	1.19E-03
	1925	2.80E-01	8.81E-03	4.79E-02	1.57E-03	3.22E-03	1.23E-04	2.84E-02	8.67E-04

Station	Depth	tSm	error	tEu	error	tGd	error	tTb	error	tDy	error
	m	nM	nM	nM	nM	nM	nM	nM	nM	nM	nM
END1 (47.957, -129.094)	2140	5.59E-03	3.78E-04	1.65E-03	1.20E-04	9.07E-03	6.55E-04	1.38E-03	6.00E-05	1.14E-02	6.35E-04
	2125	5.33E-03	2.03E-05	1.33E-03	5.75E-05	7.78E-03	3.85E-04	1.23E-03	4.53E-05	9.92E-03	4.12E-04
	2100	4.90E-03	2.20E-04	1.39E-03	8.21E-05	8.14E-03	3.73E-04	1.20E-03	6.87E-05	9.68E-03	5.24E-04
	2075	3.26E-03	1.70E-04	8.74E-04	7.38E-05	5.19E-03	2.77E-04	7.24E-04	4.54E-05	6.39E-03	1.71E-04
	2050	4.86E-03	3.32E-04	1.27E-03	7.11E-05	7.75E-03	2.43E-04	1.18E-03	7.29E-05	9.42E-03	4.24E-04
	2025	4.92E-03	3.37E-04	1.28E-03	1.51E-04	7.91E-03	6.16E-04	1.20E-03	1.19E-05	9.66E-03	3.73E-04
	2000	4.74E-03	3.26E-04	1.30E-03	1.09E-04	7.59E-03	4.17E-04	1.21E-03	6.77E-05	9.29E-03	3.04E-04
	1975	5.21E-03	1.72E-04	1.45E-03	1.38E-04	8.30E-03	6.48E-04	1.24E-03	6.56E-05	1.04E-02	5.81E-04
	1950	4.95E-03	2.88E-04	1.28E-03	9.67E-05	7.76E-03	3.19E-04	1.21E-03	6.20E-05	9.40E-03	4.69E-04
	1925	5.35E-03	4.66E-04	1.57E-03	9.03E-05	8.50E-03	4.46E-04	1.20E-03	2.67E-05	1.04E-02	6.79E-04
	1900	5.09E-03	4.70E-03	1.34E-03	5.29E-04	8.26E-03	2.49E-03	1.26E-03	NA	9.99E-03	NA
END2 (47.920, -129.144)	2200	5.31E-03	3.48E-04	1.44E-03	1.14E-04	8.57E-03	4.96E-04	1.30E-03	8.13E-05	1.06E-02	6.62E-04
	2150	1.75E-03	1.44E-04	4.22E-04	2.38E-05	3.16E-03	2.21E-04	4.50E-04	3.79E-05	4.53E-03	2.37E-04
	2125	5.49E-03	2.76E-04	1.53E-03	5.43E-05	9.08E-03	4.67E-04	1.41E-03	7.19E-05	1.10E-02	2.61E-04
	2100	3.79E-03	1.40E-04	1.02E-03	6.35E-05	5.92E-03	1.65E-04	8.54E-04	4.67E-05	7.27E-03	1.94E-04
	2075	4.87E-03	3.32E-04	1.37E-03	1.14E-04	7.82E-03	3.39E-04	1.24E-03	7.95E-05	9.89E-03	4.44E-04
	2050	4.61E-03	2.96E-04	1.35E-03	1.06E-04	7.94E-03	3.91E-04	1.18E-03	6.95E-05	9.40E-03	5.57E-04
	2025	4.81E-03	2.84E-04	1.26E-03	1.42E-04	7.69E-03	6.61E-04	1.18E-03	9.18E-05	9.03E-03	4.65E-04
	2000	3.56E-03	1.30E-04	9.58E-04	1.09E-04	5.91E-03	2.90E-04	8.09E-04	4.52E-05	7.05E-03	3.90E-04
	1975	5.44E-03	4.12E-04	1.51E-03	1.37E-04	8.16E-03	2.35E-04	1.29E-03	6.34E-05	1.02E-02	3.57E-04
	1950	3.73E-03	6.90E-05	9.86E-04	7.52E-05	5.80E-03	3.60E-04	8.49E-04	2.08E-05	7.24E-03	3.10E-04
	1925	5.40E-03	3.90E-04	1.35E-03	7.02E-05	8.13E-03	4.26E-04	1.23E-03	7.30E-05	9.83E-03	4.24E-04
END3 (47.871, -129.241)	2200	5.39E-03	3.54E-04	1.44E-03	5.29E-05	8.14E-03	2.30E-04	1.30E-03	1.02E-04	1.01E-02	2.54E-04
	2150	5.34E-03	2.54E-04	1.46E-03	9.96E-05	8.82E-03	6.24E-04	1.31E-03	9.09E-05	1.07E-02	5.18E-04
	2125	5.18E-03	4.67E-04	1.44E-03	8.69E-05	8.05E-03	3.19E-04	1.27E-03	4.41E-05	9.87E-03	6.55E-04
	2100	5.39E-03	2.29E-04	1.41E-03	1.30E-04	8.38E-03	1.31E-04	1.29E-03	9.42E-05	1.01E-02	2.21E-04

	2075	5.23E-03	1.70E-04	1.41E-03	8.99E-05	8.15E-03	4.19E-04	1.22E-03	4.45E-05	9.77E-03	5.50E-04
	2050	5.36E-03	3.38E-04	1.38E-03	1.09E-04	8.38E-03	4.41E-04	1.28E-03	5.16E-05	1.03E-02	4.00E-04
	2025	5.82E-03	1.95E-04	1.58E-03	3.52E-05	9.12E-03	4.47E-04	1.44E-03	7.44E-05	1.11E-02	3.73E-04
	2000	5.44E-03	2.63E-04	1.41E-03	6.95E-05	8.32E-03	3.03E-04	1.30E-03	4.85E-05	1.01E-02	3.17E-04
	1975	3.48E-03	1.87E-04	9.49E-04	6.51E-05	5.65E-03	3.15E-04	8.37E-04	3.66E-05	7.10E-03	2.39E-04
	1950	5.59E-03	3.32E-04	1.48E-03	7.53E-05	8.75E-03	4.26E-04	1.36E-03	6.60E-05	1.07E-02	4.63E-04
	1925	3.96E-03	4.10E-04	1.05E-03	6.86E-05	6.00E-03	3.16E-04	8.81E-04	5.55E-05	7.37E-03	3.64E-04
END4 (47.767, -129.431)	2150	3.57E-03	2.43E-04	9.36E-04	2.86E-05	5.92E-03	4.42E-04	8.46E-04	8.46E-05	6.93E-03	2.60E-04
	2125	3.41E-03	1.58E-04	9.26E-04	2.68E-05	5.79E-03	2.92E-04	8.30E-04	4.14E-05	6.87E-03	3.09E-04
	2100	3.53E-03	3.64E-04	9.30E-04	6.14E-05	5.86E-03	3.51E-04	8.77E-04	8.03E-05	7.56E-03	4.62E-04
	2075	3.61E-03	1.97E-04	9.98E-04	6.76E-05	5.84E-03	1.39E-04	8.22E-04	3.00E-05	6.99E-03	2.69E-04
	2000	3.36E-03	1.23E-04	9.69E-04	5.87E-05	5.94E-03	2.44E-04	8.34E-04	3.77E-05	7.07E-03	2.41E-04
	1975	3.58E-03	2.06E-04	9.22E-04	3.67E-05	5.54E-03	2.99E-04	7.61E-04	3.33E-05	6.92E-03	2.27E-04
	1950	4.74E-03	4.11E-04	1.36E-03	3.72E-05	7.88E-03	3.27E-04	1.21E-03	7.69E-05	9.64E-03	3.89E-04
	1925	4.84E-03	3.38E-04	1.27E-03	1.62E-04	7.63E-03	4.61E-04	1.17E-03	8.37E-05	9.17E-03	4.95E-04
END5 (47.645, -129.605)	2200	5.58E-03	8.45E-05	1.49E-03	5.06E-05	8.52E-03	3.26E-04	1.25E-03	3.76E-05	1.02E-02	2.93E-04
	2150	5.12E-03	2.39E-04	1.36E-03	1.07E-04	7.96E-03	5.97E-04	1.22E-03	1.14E-05	9.80E-03	1.82E-04
	2100	5.07E-03	1.99E-04	1.42E-03	9.71E-05	8.26E-03	3.11E-04	1.24E-03	7.33E-05	1.00E-02	3.42E-04
	2075	5.36E-03	2.85E-04	1.56E-03	8.15E-05	8.52E-03	3.02E-04	1.24E-03	5.40E-05	1.03E-02	4.35E-04
	2025	5.28E-03	3.58E-04	1.45E-03	1.33E-04	8.21E-03	1.94E-04	1.22E-03	8.83E-05	1.04E-02	4.93E-04
	2000	5.13E-03	2.39E-04	1.45E-03	9.36E-05	8.38E-03	4.84E-04	1.26E-03	4.40E-05	1.04E-02	2.93E-04
	1975	5.35E-03	2.37E-04	1.53E-03	5.48E-05	8.55E-03	3.75E-04	1.20E-03	8.05E-05	1.06E-02	3.99E-04
	1950	4.82E-03	1.88E-04	1.27E-03	1.05E-04	7.73E-03	3.80E-04	1.18E-03	5.06E-05	9.29E-03	4.82E-04
	1925	5.18E-03	2.23E-04	1.38E-03	5.82E-05	8.41E-03	4.37E-04	1.20E-03	5.18E-05	1.01E-02	5.27E-04

Station	Depth	tHo	error	tEr	error	tTm	error	tYb	error	tLu	error
	m	nM	nM	nM	nM	nM	nM	nM	nM	nM	nM
END1 (47.957, -129.094)	2140	3.16E-03	1.80E-04	1.08E-02	5.27E-04	1.65E-03	6.63E-05	1.15E-02	7.66E-04	2.02E-03	1.95E-04
	2125	2.76E-03	1.38E-04	9.45E-03	3.87E-04	1.47E-03	1.02E-04	1.03E-02	4.16E-04	1.78E-03	8.06E-05
	2100	2.74E-03	1.18E-04	9.43E-03	7.78E-04	1.43E-03	6.67E-05	1.01E-02	3.43E-04	1.79E-03	5.00E-05
	2075	1.64E-03	7.73E-05	5.89E-03	3.62E-04	7.63E-04	4.48E-05	6.05E-03	2.21E-04	9.98E-04	1.34E-05
	2050	2.61E-03	1.67E-04	8.96E-03	3.89E-04	1.44E-03	4.87E-05	9.84E-03	3.43E-04	1.70E-03	6.64E-05
	2025	2.68E-03	7.49E-05	9.16E-03	6.27E-04	1.40E-03	8.03E-05	9.83E-03	5.03E-04	1.73E-03	1.28E-04
	2000	2.59E-03	8.72E-05	8.94E-03	3.76E-04	1.39E-03	8.32E-05	9.55E-03	2.72E-04	1.69E-03	9.33E-05
	1975	2.74E-03	1.67E-04	9.83E-03	6.28E-04	1.44E-03	8.01E-05	1.08E-02	5.11E-04	1.83E-03	8.69E-05
	1950	2.66E-03	2.12E-04	8.96E-03	4.22E-04	1.37E-03	8.62E-05	9.63E-03	5.49E-04	1.72E-03	8.04E-05
	1925	2.71E-03	1.50E-04	9.89E-03	7.35E-04	1.43E-03	4.82E-05	1.08E-02	4.32E-04	1.87E-03	8.45E-05
	1900	2.78E-03	6.23E-03	9.71E-03	2.17E-02	1.46E-03	#VALUE!	1.05E-02	1.43E-02	1.76E-03	1.84E-03
END2 (47.920, -129.144)	2200	2.95E-03	1.59E-04	1.03E-02	4.33E-04	1.53E-03	9.42E-05	1.09E-02	7.28E-04	1.90E-03	1.19E-04
	2150	1.46E-03	4.33E-05	5.34E-03	1.83E-04	8.01E-04	4.10E-05	6.04E-03	7.93E-05	1.07E-03	7.35E-05
	2125	3.06E-03	9.65E-05	1.07E-02	6.59E-04	1.63E-03	6.50E-05	1.16E-02	4.30E-04	2.00E-03	1.24E-04
	2100	1.89E-03	9.18E-05	6.82E-03	4.24E-04	9.88E-04	7.45E-05	7.45E-03	2.45E-04	1.30E-03	2.27E-05
	2075	2.68E-03	7.62E-05	9.31E-03	3.48E-04	1.42E-03	7.03E-05	1.00E-02	2.50E-04	1.76E-03	9.14E-05
	2050	2.65E-03	1.12E-04	9.24E-03	7.94E-04	1.39E-03	1.13E-04	9.62E-03	1.77E-04	1.69E-03	1.37E-04
	2025	2.58E-03	9.45E-05	8.80E-03	2.97E-04	1.33E-03	6.62E-05	9.56E-03	2.95E-04	1.65E-03	8.18E-05
	2000	1.87E-03	7.23E-05	6.81E-03	4.62E-04	9.84E-04	3.00E-05	7.55E-03	3.78E-04	1.29E-03	5.23E-05
	1975	2.80E-03	8.01E-05	9.68E-03	4.76E-04	1.46E-03	4.63E-05	1.05E-02	4.00E-04	1.83E-03	9.70E-05
	1950	1.96E-03	8.68E-05	7.07E-03	2.74E-04	1.01E-03	3.20E-05	7.77E-03	3.60E-04	1.32E-03	4.69E-05
	1925	2.72E-03	1.29E-04	9.52E-03	4.22E-04	1.41E-03	1.10E-04	9.99E-03	4.04E-04	1.75E-03	9.64E-05
END3 (47.871, -129.241)	2200	2.83E-03	2.43E-04	9.39E-03	9.48E-04	1.42E-03	7.77E-05	1.02E-02	7.90E-04	1.80E-03	1.12E-04
	2150	2.97E-03	8.49E-05	1.03E-02	5.36E-04	1.54E-03	7.25E-05	1.11E-02	4.29E-04	1.95E-03	3.09E-05
	2125	2.83E-03	1.17E-04	9.56E-03	7.32E-04	1.44E-03	5.94E-05	1.04E-02	5.02E-04	1.84E-03	9.68E-05
	2100	2.81E-03	1.71E-04	9.77E-03	5.31E-04	1.47E-03	4.95E-05	1.04E-02	4.45E-04	1.82E-03	3.93E-05

	2075	2.79E-03	1.35E-04	9.48E-03	2.55E-04	1.44E-03	9.50E-05	1.04E-02	1.88E-04	1.76E-03	6.85E-05
	2050	2.89E-03	8.28E-05	9.62E-03	3.08E-04	1.50E-03	5.60E-05	1.08E-02	3.53E-04	1.88E-03	5.76E-05
	2025	3.12E-03	8.42E-05	1.07E-02	3.81E-04	1.65E-03	4.23E-05	1.17E-02	5.24E-04	2.05E-03	9.22E-05
	2000	2.83E-03	8.20E-05	9.67E-03	2.14E-04	1.49E-03	6.36E-05	1.04E-02	2.91E-04	1.87E-03	7.32E-05
	1975	1.85E-03	7.15E-05	6.70E-03	2.16E-04	9.85E-04	2.22E-05	7.40E-03	1.98E-04	1.27E-03	4.93E-05
	1950	3.01E-03	1.18E-04	1.02E-02	6.50E-04	1.57E-03	9.69E-05	1.13E-02	4.14E-04	1.96E-03	5.08E-05
	1925	1.87E-03	7.75E-05	6.73E-03	4.52E-04	1.00E-03	3.80E-05	7.53E-03	5.23E-04	1.28E-03	3.67E-05
END4 (47.767, -129.431)	2150	1.83E-03	7.41E-05	6.61E-03	3.08E-04	9.45E-04	5.59E-05	7.46E-03	2.51E-04	1.21E-03	7.97E-05
	2125	1.79E-03	8.88E-05	6.56E-03	2.18E-04	9.44E-04	5.00E-05	7.39E-03	3.68E-04	1.27E-03	4.35E-05
	2100	2.20E-03	1.10E-04	7.82E-03	2.10E-04	1.17E-03	7.88E-05	8.47E-03	3.03E-04	1.49E-03	7.78E-05
	2075	1.86E-03	5.32E-05	6.73E-03	2.88E-04	1.01E-03	2.35E-05	7.60E-03	2.44E-04	1.29E-03	4.79E-05
	2000	1.87E-03	1.06E-04	6.84E-03	3.51E-04	9.70E-04	5.11E-05	7.51E-03	3.98E-04	1.27E-03	8.28E-05
	1975	1.84E-03	5.43E-05	6.67E-03	4.47E-04	9.43E-04	5.20E-05	7.18E-03	3.00E-04	1.24E-03	5.80E-05
	1950	2.67E-03	1.15E-04	9.28E-03	5.59E-04	1.41E-03	2.66E-05	9.82E-03	5.00E-04	1.73E-03	6.93E-05
	1925	2.60E-03	1.09E-04	8.87E-03	3.71E-04	1.35E-03	1.07E-04	9.59E-03	5.57E-04	1.66E-03	1.57E-04
END5 (47.645, -129.605)	2200	2.83E-03	3.72E-05	9.82E-03	3.14E-04	1.40E-03	5.21E-05	1.08E-02	1.12E-04	1.87E-03	4.48E-05
	2150	2.75E-03	5.61E-05	9.44E-03	3.78E-04	1.45E-03	7.84E-05	1.02E-02	2.31E-04	1.79E-03	6.35E-05
	2100	2.83E-03	1.11E-04	9.56E-03	5.37E-04	1.48E-03	7.17E-05	1.03E-02	5.15E-04	1.80E-03	6.91E-05
	2075	2.71E-03	1.83E-04	9.66E-03	5.39E-04	1.42E-03	5.65E-05	1.09E-02	5.26E-04	1.83E-03	9.84E-05
	2025	2.71E-03	1.30E-04	9.66E-03	5.54E-04	1.44E-03	8.96E-05	1.08E-02	3.70E-04	1.83E-03	1.22E-04
	2000	2.78E-03	7.68E-05	1.00E-02	4.89E-04	1.45E-03	1.19E-04	1.09E-02	4.31E-04	1.84E-03	9.17E-05
	1975	2.77E-03	9.32E-05	1.00E-02	3.66E-04	1.44E-03	8.33E-05	1.09E-02	3.14E-04	1.84E-03	1.04E-04
	1950	2.59E-03	1.30E-04	8.86E-03	2.87E-04	1.36E-03	8.60E-05	9.60E-03	4.81E-04	1.71E-03	1.17E-04
	1925	2.74E-03	6.58E-05	9.80E-03	4.60E-04	1.44E-03	7.75E-05	1.08E-02	3.45E-04	1.85E-03	1.06E-04

Appendix C. Vertical profiles of dissolved REE.

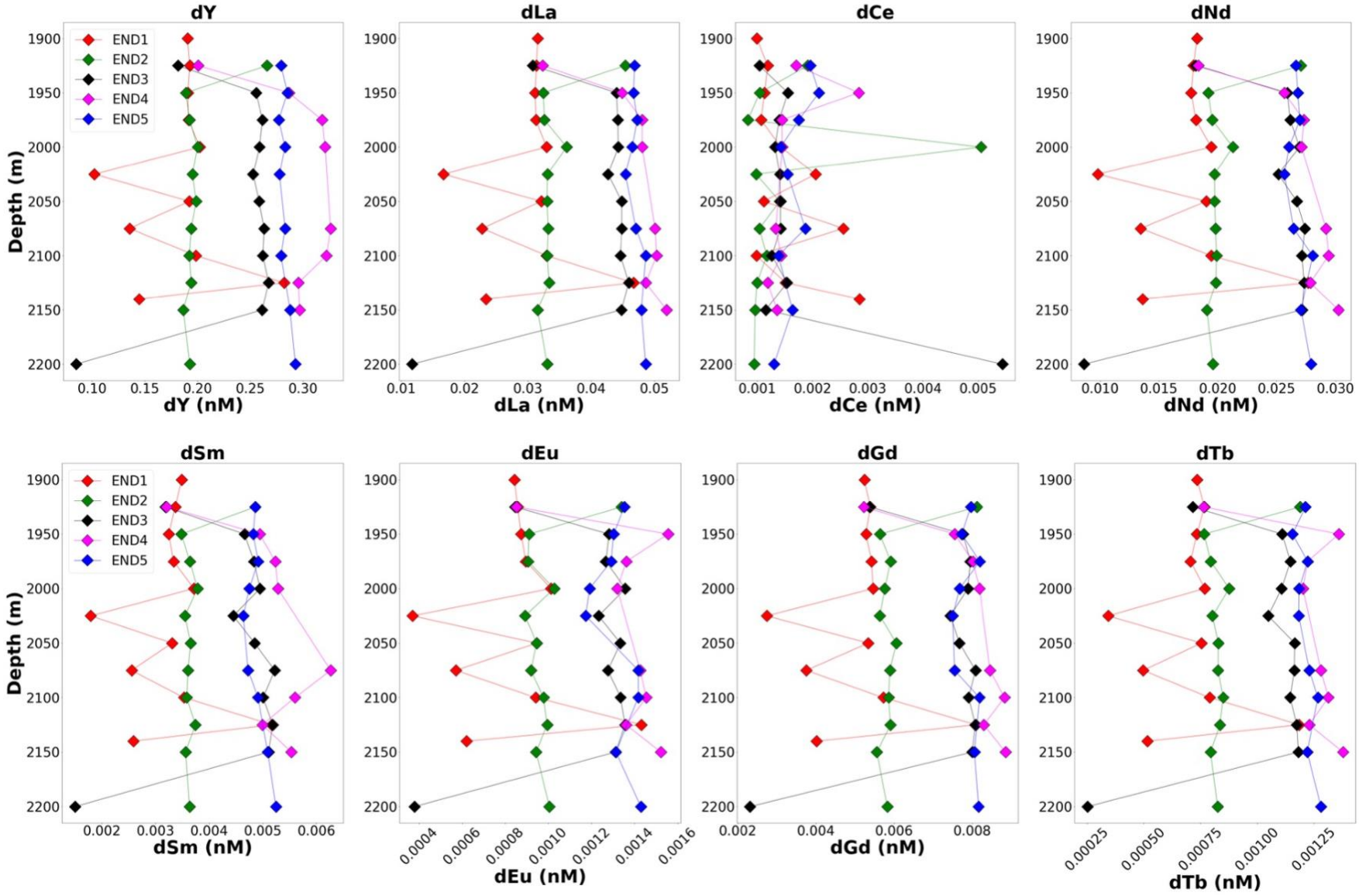

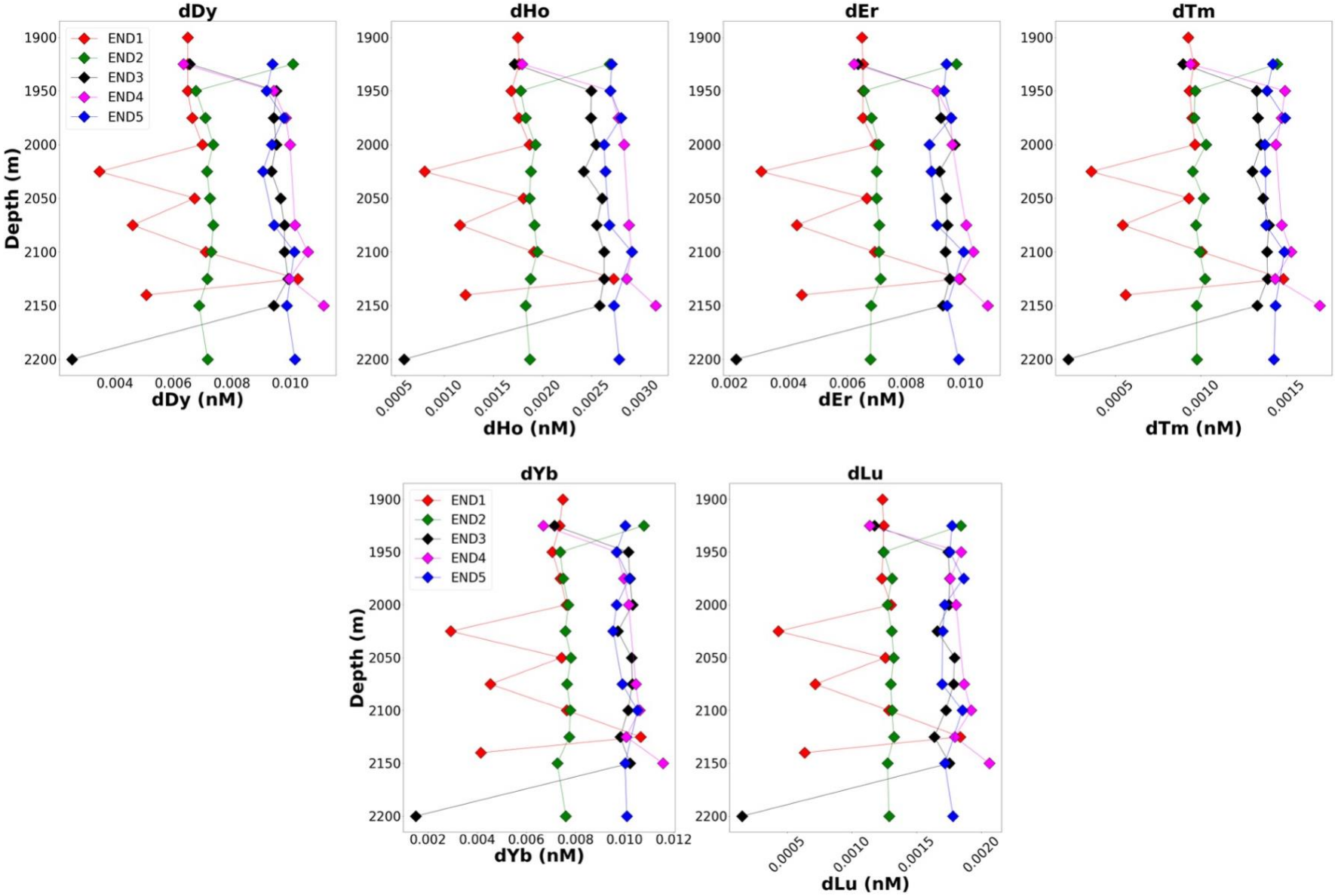
dDy
dHo
dEr
dTm
dYb
dLu
END1
END2
END3
END4
END5
Depth (m)
dDy (nM)
dHo (nM)
dEr (nM)
dTm (nM)
dYb (nM)
dLu (nM)

Appendix D. Data table of parameters used in Fe oxidation calculations.

Table D1. Parameters used to calculate Fe half-life and oxidation rate.

Station	Temp (ºC)	O_2 (umol kg^{-1})	Salinity	pH	Pressure (dbar)	ALK	DIC	log k	k1 (min^{-1})	Half-life (hour)
END1	2.03	51.20	34.57	7.72	1875.00	2412.00	2356.56	14.25	1.32E-03	8.75
	2.01	55.60	34.58	7.73	1924.70	2414.53	2352.80	14.25	1.56E-03	7.39
	2.01	56.90	34.58	7.74	1949.50	2414.53	2351.50	14.25	1.63E-03	7.08
	2.01	62.20	34.60	7.76	1974.90	2417.80	2346.40	14.25	2.01E-03	5.75
	2.00	61.80	34.60	7.76	1999.50	2417.63	2347.02	14.25	1.97E-03	5.87
	2.00	61.80	34.60	7.76	2024.80	2417.65	2347.06	14.25	1.96E-03	5.88
	1.97	62.60	34.60	7.76	2049.90	2417.93	2346.78	14.25	1.99E-03	5.79
	1.96	62.30	34.60	7.76	2074.20	2417.80	2347.20	14.25	1.96E-03	5.88
	1.96	62.50	34.60	7.76	2099.90	2417.93	2347.01	14.25	1.98E-03	5.84
	2.00	62.90	34.60	7.76	2124.90	2418.02	2346.08	14.25	2.03E-03	5.68
	2.02	63.50	34.60	7.76	2149.90	2418.10	2345.06	14.25	2.09E-03	5.52
	1.96	63.90	34.60	7.76	2174.10	2418.36	2345.80	14.25	2.07E-03	5.59
END2	2.09	47.40	34.56	7.70	1849.70	2410.13	2359.17	14.25	1.16E-03	9.98
	2.05	50.20	34.57	7.71	1900.10	2411.54	2357.18	14.25	1.28E-03	9.04
	2.03	51.20	34.57	7.71	1924.80	2412.02	2356.51	14.25	1.32E-03	8.74
	1.99	54.20	34.58	7.72	1949.90	2413.21	2354.35	14.25	1.46E-03	7.94
	1.98	55.00	34.58	7.73	1975.00	2413.68	2353.80	14.25	1.49E-03	7.73
	1.97	56.30	34.58	7.73	1999.40	2414.06	2352.75	14.25	1.56E-03	7.41
	1.97	56.90	34.58	7.73	2024.80	2414.49	2352.28	14.25	1.59E-03	7.25
	1.96	58.00	34.59	7.74	2049.80	2415.00	2351.38	14.25	1.65E-03	6.98
	1.95	58.70	34.59	7.74	2074.00	2415.38	2350.86	14.25	1.69E-03	6.83
	1.94	60.50	34.59	7.74	2099.00	2416.19	2349.31	14.25	1.80E-03	6.42
	1.94	63.00	34.60	7.76	2124.20	2417.82	2347.00	14.25	1.98E-03	5.83
	1.92	65.40	34.60	7.76	2148.90	2418.21	2345.06	14.25	2.11E-03	5.46
	1.87	67.90	34.61	7.77	2198.70	2419.31	2343.57	14.25	2.25E-03	5.13

END3	2.08	47.50	34.56	7.70	1849.70	2410.26	2359.12	14.25	1.16E-03	9.94
	2.03	51.20	34.57	7.72	1899.90	2411.83	2356.50	14.25	1.32E-03	8.76
	2.01	52.50	34.57	7.72	1925.00	2412.36	2355.63	14.25	1.37E-03	8.41
	1.99	54.30	34.58	7.72	1949.20	2413.15	2354.31	14.25	1.46E-03	7.93
	1.97	56.60	34.58	7.73	1974.10	2413.85	2352.46	14.25	1.57E-03	7.36
	1.95	57.40	34.58	7.74	1999.30	2414.59	2352.04	14.25	1.61E-03	7.17
	1.94	59.10	34.59	7.74	2023.90	2415.59	2350.59	14.25	1.71E-03	6.74
	1.93	60.30	34.59	7.75	2048.90	2416.12	2349.61	14.25	1.78E-03	6.48
	1.94	61.40	34.60	7.75	2074.80	2416.93	2348.50	14.25	1.87E-03	6.18
	1.92	62.90	34.60	7.75	2099.40	2417.29	2347.43	14.25	1.94E-03	5.94
	1.88	65.00	34.60	7.76	2124.60	2417.87	2346.16	14.25	2.05E-03	5.65
	1.87	66.50	34.60	7.76	2148.70	2418.53	2344.93	14.25	2.14E-03	5.39
	1.84	68.80	34.61	7.77	2198.90	2419.71	2343.14	14.25	2.30E-03	5.02
END4	2.07	49.20	34.57	7.71	1849.20	2410.69	2357.77	14.25	1.23E-03	9.38
	2.03	52.10	34.57	7.72	1900.00	2412.19	2355.76	14.25	1.36E-03	8.49
	2.01	53.40	34.58	7.72	1925.00	2412.83	2354.88	14.25	1.42E-03	8.14
	1.99	54.50	34.58	7.73	1948.90	2413.49	2354.14	14.25	1.47E-03	7.84
	1.97	56.10	34.58	7.73	1975.50	2414.32	2352.97	14.25	1.55E-03	7.43
	1.96	57.40	34.59	7.74	1998.90	2414.91	2351.98	14.25	1.62E-03	7.12
	1.94	59.00	34.59	7.74	2024.80	2415.59	2350.69	14.25	1.71E-03	6.76
	1.93	60.50	34.59	7.75	2050.80	2416.25	2349.49	14.25	1.80E-03	6.43
	1.91	62.70	34.60	7.75	2075.80	2416.97	2347.69	14.25	1.92E-03	6.01
	1.89	64.20	34.60	7.76	2099.30	2417.80	2346.74	14.25	2.01E-03	5.76
	1.87	66.10	34.60	7.76	2123.70	2418.33	2345.29	14.25	2.12E-03	5.46
	1.86	67.00	34.60	7.77	2148.80	2418.74	2344.53	14.25	2.18E-03	5.31
	1.84	68.60	34.61	7.77	2199.80	2419.80	2343.33	14.25	2.29E-03	5.05
END5	2.07	47.90	34.57	7.70	1848.90	2410.47	2358.91	14.25	1.18E-03	9.82
	2.04	51.10	34.57	7.71	1900.60	2411.81	2356.51	14.25	1.32E-03	8.78
	2.01	53.80	34.58	7.72	1925.10	2412.87	2354.49	14.25	1.44E-03	8.03
	1.98	55.10	34.58	7.73	1949.60	2413.75	2353.68	14.25	1.50E-03	7.69
	1.97	56.30	34.58	7.73	1973.80	2414.40	2352.85	14.25	1.56E-03	7.39

	1.94	58.40	34.59	7.74	2000.40	2415.21	2351.23	14.25	1.67E-03	6.91
	1.93	59.00	34.59	7.74	2025.10	2415.68	2350.84	14.25	1.71E-03	6.77
	1.92	60.40	34.59	7.75	2049.80	2416.08	2349.68	14.25	1.78E-03	6.48
	1.91	61.90	34.60	7.75	2074.40	2416.78	2348.56	14.25	1.87E-03	6.19
	1.89	63.60	34.60	7.76	2099.70	2417.57	2347.28	14.25	1.97E-03	5.88
	1.87	64.90	34.60	7.76	2124.20	2418.14	2346.29	14.25	2.04E-03	5.65
	1.87	65.60	34.60	7.76	2148.90	2418.42	2345.71	14.25	2.09E-03	5.53
	1.84	68.60	34.61	7.77	2199.40	2419.71	2343.38	14.25	2.28E-03	5.06

Appendix E. Results of ANOVA test assessing the significance of changes in the proportions of dissolved and particulate Fe and Mn.

Table E1. ANOVA test comparing concentrations of dMn between stations. Results suggest differences in dMn concentrations between END1 and END5 and END3 and END5 are statistically significant with p-values of 0.002 and 0.047 respectively.

Group 1	Group 2	p-value	F-statistic
END1	END3	0.182	1.96
END1	END4	0.054	4.69
END1	END5	0.002	13.9
END3	END4	0.339	0.982
END3	END5	0.047	4.60
END4	END5	0.497	0.496

Table E2. ANOVA test comparing concentrations of dFe between stations. Results suggest differences in dFe concentrations between END1 and END5 and END3 and END5 are statistically significant with p-values of 0.023 and 0.012 respectively.

Group 1	Group 2	p-value	F-statistic
END1	END3	0.398	0.749
END1	END4	0.268	1.33
END1	END5	0.023	6.39
END3	END4	0.141	2.46
END3	END5	0.012	8.20
END4	END5	0.348	0.967